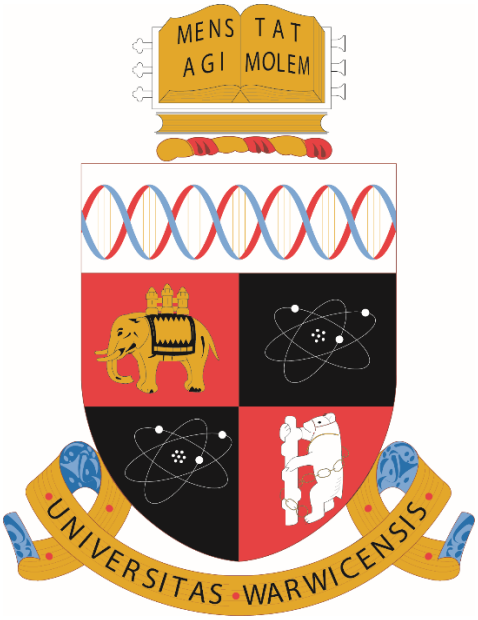

Characterisation of Encapsulation Grown Nanowires

by

Samuel Robert Marks

Thesis

Submitted to the University of Warwick

for the degree of

Doctor of Philosophy

Department of Physics

October 2017

Contents

List of Figures

List of Tables

Abbreviations

[EMIM][BF_4]	1-ehtyl-3-methylimidazolium tetrafluoroborate
[N^nBu_4]	Tetrabutylammonium
3H	3-atom Helix
AAO	Anodic Aluminium Oxide
ADF	Annular Dark-field
AIRSS	*Ab Initio* Random Structure Searching
BF	Bright Field
BSE	Backscattered Electron
CNT	Carbon Nanotube
CTF	Contrast Transfer Function
CVD	Chemical Vapor Deposition
DF	Dark Field
DOS	Density of States
EDX	Energy-dispersive X-ray Spectroscopy
EELS	Electron Energy Loss Spectroscopy
FCC	Face centred Cubic
FEG	Field Emission Gun
FET	Field Effect Transistor
FIB	Focussed Ion Beam
HAADF	High-angle Annular Dark-field
HDR-ED	High Dynamic Range Electron Diffraction
HRTEM	High-resolution Transmission Electron Microscopy
HRSTEM	High-resolution Scanning Transmission Electron Microscopy

IPA	Isopropyl alcohol
JFET	Junction Field Effect Transistor
MOSFET	Metal Oxide Semiconductor Field Effect Transistor
MWNT	Multi Walled Nanotube
RDF	Radial Distribution Function
SADP	Selected Area Electron Diffraction Pattern
SCF	Supercritical Fluid
SCFED	Supercritical Fluid Electrodeposition
scR32	Supercritical Difluoromethane
SE	Secondary Electron
SEM	Scanning Electron Microscope (Microscopy)
STEM	Scanning Transmission Electron Microscope (Microscopy)
SWNT	Single-walled Nanotube
TEM	Transmission Electron Microscope (Microscopy)
VLS	Vapor-Liquid-Solid
XRD	X-ray Diffraction

Acknowledgements

I would like to thank some brilliant people who, without their help this thesis and my PhD would not have come to fruition.

Many thanks to Jeremy Sloan for his encouragement and dedication. I fondly remember our trip to Moscow and countless conversations about Macbeth and Blackadder.

Secondly Dr Richard Beanland for the hours given to me and his insight and tuition in all areas of electron microscopy, sublimation and gas flow. Also, Dr David Smith for his daily skype conversations; Dr Ana Sanchez for her guidance and Dr Neil Wilson for the generally off topic conversations.

Within the group, the imparted wisdom about life, PhDs and postdocs from Dr Alex Marsden has been indispensable. I would like to especially mention Dr Jon Peters who has supported me throughout this process, always available for a cup of tea and a chat, he is a great friend and has helped me immensely. I hope my pointless waffle hasn't driven him too insane.

Thanks to the microscopy technicians, Steve York and Steve Hindmarsh. They are a lifeline within the group and appear to have an unlimited supply of patience. I would like to thank Steve Hindmarsh especially for the hours spent in the FIB room to sample prep and rightmove.

Cheers to all my family for their unlimited encouragement. My mum's constant belief and unwavering support is inspirational and a day doesn't pass that I don't think of my dad and how proud he would be. Matt and Tim, thanks for trying to be interested and asking how it was going!

Finally, I would like to thank my girlfriend Martina. Meeting her at the start of this process, she has been by my side every step of the way making the whole journey unforgettable. The level of patience and understanding she has shown me is truly selfless and I wouldn’t be here without her. I look forward to our future adventures together.

Declarations

I declare that this thesis contains an account of my research work carried out at the Department of Physics, University of Warwick, between October 2013 and Sep 2017 under the supervision of Dr J. Sloan. The research reported here has not been previously submitted, wholly or in part, at this or any other academic institution for admission to a higher degree.

Parts of this thesis have been published by the author between October 2013 and Sep 2017:

- The experimental data in Section 3.2.1 on Ge thin films has been published as:

  Cummings, C.Y., Bartlett, P.N., Pugh, D., Reid, G., Levason, W., Hasan, M.M., Hector, A.L., Spencer, J., Smith, D.C., Marks, S. and Beanland, R., 2016. Electrodeposition of Protocrystalline Germanium from Supercritical Difluoromethane. ChemElectroChem, 3(5), pp.726-733.

- The Te nanowires in Section 4.2 have been published as:

  Bartlett, P.N., Cook, D.A., Hasan, M.M., Hector, A.L., Marks, S., Naik, J., Reid, G., Sloan, J., Smith, D.C., Spencer, J. and Webber, Z., 2017. Supercritical fluid electrodeposition, structural and electrical characterisation of tellurium nanowires. RSC Advances, 7(65), pp.40720-40726.

- The data and findings in Chapter 5 on both SbTe and Te encapsulation have been published as:

  Marks, S.R., Morawiec, K., Dluzewski, P., Kret, S. and Sloan, J., 2017. In Situ Electron Beam Amorphisation of Sb2Te3 within Single-walled Carbon Nanotubes. Acta Physica Polonica A, 131(5), pp.1324-1327.

  Medeiros, P.V., Marks, S., Wynn, J.M., Vasylenko, A., Ramasse, Q.M., Quigley, D., Sloan, J. and Morris, A.J., 2017. Single-Atom Scale Structural Selectivity in Te Nanowires Encapsulated inside Ultra-Narrow, Single-Walled Carbon Nanotubes. ACS nano.

  All the work presented here was completed by myself, except for the following:

- SCFED samples analysed in Chapters 3 and 4 were created by D. Cook or C. Cummings.

- The XRD data in Figure 3.2 was acquired by A. Hector.
- The Raman spectras in Figure 3.3 were acquired by J. Spencer.
- STEM images and EELS data shown in figures 5.6 and 5.9 were acquired by Q. Ramasse, SuperSTEM.
- The AIRSS simulations for Te, including formation energy plots and DOS calculations in figure 5.7 were performed by P. Mendeiros and A. Morris.
- The AIRSS simulations for SNTe, including convex hull diagram and formation energy vs SWNT diameter plot were calculated by A. Vasylenko.

Abstract

The push to decrease the size of electronic components has been pioneered over the last decade. This has led to electrodeposition being a primary nanoscale fabrication method. However, this technique is beginning to reach its physical limits with respect to the size of media that can be deposited. Therefore, alternative methods of sub 10 nm fabrication are being investigated. This thesis aims to explore: supercritical fluid electrodeposition as an encapsulated nanowire fabrication method, the phase transitions involved when heating said nanowires in situ and the encapsulation of materials within carbon nanotubes to form truly one-dimensional nanowires. All of this is undertaken using electron microscopy as the primary analysis technique.

First, the supercritical fluid electrodeposition process is investigated as a nanowire fabrication technique. Initially, Ge planar films are deposited and shown to form electron beam sensitive crystallites embedded within an amorphous Ge matrix. This is expanded upon, with the deposition of Ge into 13 nm anodic alumina pores, also resulting in the formation of amorphous Ge nanowires. More advanced systems are explored, with crystalline CuTe nanowires forming in the P4/nmm space group. Further to this, the CuTeS system, the first supercritical fluid electrodeposited tertiary system, is proved to form in the Cu_6Te_3S structure. Sn is deposited into hierarchical alumina in attempts to decrease the encapsulated media size. This shows the ability for sub 10 nm nanowire formation from supercritical fluid electrodeposition.

Next, the effects of in situ heating for both Te and Bi nanowires are presented. Here the Te system underwent a sublimation phase transition. The experimental rate of sublimation is imperfect and generates an evaporation coefficient of 2×10^{-3} as a multiplying factor. The effects of elemental contamination manifests in two forms during sublimation. The first as unmoving large masses that slow the rate of sublimation. The second, as a small atomic percentage that flows along the nanowire, at the sublimation front, before condensing in the end of the nanowire. Sublimation is not the only observed phase transition with Bi proven to melt in situ becoming an encapsulated liquid. Selected area diffraction, with radial distribution analysis, results in the first liquid Bi radial peak measured at 3.47 Å. This is akin to bulk neutron diffraction and XRD measurements, however, this is believed to be the first nanoscale measurement. Examination of the suspected pressure drop arising from the remnant alumina proves that the alumina coatings are non-continuous, as no experimental pressure drop is observed.

Finally, the encapsulation of materials within carbon nanotubes is presented. It is demonstrated that the melt filling, from Ge and SbTe, will form crystalline bulk-like nanowires during encapsulation. The effects of electron beam interaction are visible, with energetic encapsulated crystallites. A study of the encapsulated SbTe indicates that for an 80kV electron beam, the threshold for amorphisation, due to electron beam heating, lies between a beam energy of 0.8 and 1.5 pA cm^{-2}. Striving for higher filling percentages the sublimation filling technique is examined. For the case of Te, both a bulk-like helix and one-dimensional chain structure is observed across a range of nanowire diameters. Additionally, SnTe is formed generating a one-dimensional chain, for low dimension carbon nanotubes, and a zigzag structure within higher diameters. The chemical composition of both systems is examined using EELS. This proves the Te and zigzag SnTe chemical compositions, but suggests that the SnTe one-dimensional chain is SnI. In order to characterise the crystal structures ab initio random structure searches are performed for the first time. These result in a new level of structural understanding arising from this first order simulation process.

Introduction

1.1 Introduction

The previous 150 years has seen technological advancement in all areas at an unprecedented scale. A key area that has undergone major technical advancement is electronics, especially regarding the power, size and cost of components. In 1965 Gordon Moore quantified the growth within the semiconductor industry. Now referred to as Moore's Law he observed and predicted that the number of components on an integrated circuit board, initially 2500, was doubling every year and would continue to do so for another 10 years.[1-2] This prediction has had a profound effect on the semiconductor industry, with many people claiming that it has been the driving force in reducing the size of components leading to integrated circuit boards with over 1 billion components on them.[3]

This push to reduce the size of components has led to major improvements within modern lithography techniques with the successful production of sub 14 nm transistors.[4] It is believed, however, that modern lithography is reaching its resolution limit and over the next decade will fail to maintain Moore's law.[5] Because of this there has been a push towards alternative fabrication techniques, devices and materials. Key examples of this are bottom-up growth, 2D heterostructures and graphene.[6-8]

A key component in the transition to nanometre based materials and structures is visualisation. Due to the demanding size restriction emplaced on modern materials it is no longer possible to image them using conventional optical microscopy. Instead they must be visualised using electron microscopy, predominantly using scanning electron microscopy (SEM), transmission electron microscopy (TEM) and scanning transmission electron microscopy (STEM).

This thesis examines a range of nanomaterials, especially nanowires, investigated and imaged using electron microscopy. Specifically, it explores the results of both a new nanowire formation technique, supercritical fluid electrodeposition, and the encapsulation of nanowires within carbon nanotubes. A key theme throughout is *in situ* experimentation, be that through heating or electron beam irradiation.

1.2 Background

1.2.1 Nanowires

Nanowires are structures with a diameter in the nm scale with an extremely high ratio of length to width. The basic formation mechanism for nanowires is predominantly bottom-up growth, examples of which include vapor-liquid-solid (VLS) growth and electrodeposition into porous templates.[9-10] Advantages of bottom up growth are the degrees of control on key parameters, including size, chemical composition, doping, morphology and structure, detailed below. These parameters are what define the physical properties of the nanowires and therefore the properties and functions of the resulting devices.

There are several different nanowire formation techniques with VLS being a well-established method stemming from chemical vapour deposition. Here, nanowires are formed at the interface between a substrate and liquid catalyst when the liquid catalyst becomes supersaturated. An example of this is the growth of Si nanowires in which a liquid Au droplet reacts with gaseous Si to form liquid AuSi, upon Si supersaturation the Si precipitates beneath the droplet forming a Si nanowire.[11] The physical properties of the nanowires, like diameter and nanowire composition, are dependent on the catalyst. The catalyst material is often a metal, examples of such include Cu, Au and Mn.[12-14] Heterogeneous nanowires are easily formed using this technique by switching the gases to form both core/shell and axial heterogeneous nanowires.[15-16]

An alternative technique for bottom-up nanowire generation is through electrodeposition into mesoporous templates.[17] A conducting surface is deposited onto one side of a nanowire template consisting of a self-organised hexagonal array, predominantly SiO and anodic alumina oxide (AAO).[18-19] This is then submerged in a liquid solvent which reacts with the conducting surface when charge is passed through it filling the pores with the deposition material.[20] A variation of this technique was used to produce the majority of the samples examined within this thesis and is described in greater detail in Section 1.2.2.

There are three categories of nanowire, as described in Table 1.1: homogeneous, axial heterostructures and radial heterostructures.[21-23] They may be single-crystal, polycrystalline or amorphous with an elemental composition ranging from a single element to ternary systems and more.[24-26] Homogeneous nanowires have a single continuous composition throughout the nanowire. In comparison axial heterostructures have a fluctuating elemental composition altered along the growth axis of the nanowire.[27] One way of achieving this, using VLS, is by modifying the flow of reactants to grow a different material, which may be repeated multiple times to achieve a stacking structure. Radial heterogeneous nanowires are defined by their core/shell structures with an internal homogeneous nanowire coated with at least one material.[28] Again, for VLS, the shell is formed by changing the deposition conditions to favour deposition onto the nanowire surface instead of at the catalyst particle.

An important ability required during nanowire fabrication, especially in the interest of applications, is the ability to dope the nanowires. Doping is the act of intentionally introducing impurities into the nanowire to alter its electrical properties.[29] Group IV elements on the periodic table have four electrons in their outer electron shell and are semiconductors. Materials whose electrical resistivity falls between conducting and insulating, making their electrical properties very susceptible to impurities. There are two types of doping: n-type and p-type, described below.

Homogeneous	Axial Heterogeneous	Radial Heterogeneous
Definition • Single continuous elemental composition. 	Definition • Contains at least one axial junction upon which the composition changes. 	Definition • Homogenous core nanowire with at least one material shell. 
Examples: Si, GaAs, InGaAs	Examples: InAs/GaAs, Au/ZnO	Examples: ZnO/ZnMgO, GaAs/AlGaAs

Table 1.1: Visual examples of the homogeneous, axial heterogeneous and radial heterogeneous nanowire structures grown using the VLS method including example structures.

The first type of doping is N-type semiconductors, named from the majority of negative current carriers which are electrons. The substitution of a group IV element, like Ge, with that of a group V element, like As, within a crystal lattice occurs comfortably with the As generating the same four covalent bonds as the Ge whilst including a fifth, effectively spare, electron. This electron is very loosely bound as it is not covalently bonded with the Ge and is shielded from the nucleus, leaving it with a binding energy of ≈ 0.01 eV. Therefore, looking at the band picture, the electron sits 0.01 eV away from the conduction band, known as the donor level, and with kT equal to ≈ 0.025 eV at room temperature electrons can easily transition into the conduction band and the material becomes conducting.[30] Examples of such are shown in Figure 1.1 a and b.

A similar effect arises from substitution with a group III element instead of a group V element, the only difference being the material having three available electrons instead of five. Using the example of Ga substitution within Ge, it attempts to make the four covalent bonds but with only three outer electrons. It then borrows an electron from a neighbouring Ge, fulfilling the need for four covalent bonds and generating a hole. Analogous to the n-

type system, the stolen electron generates an acceptor level with an energy ≈ 0.01 eV above the valence band. This is known as a p-type semiconductor, as the dominant current carrier system is now holes, which are positively charged, Figure 1.1 c and d.

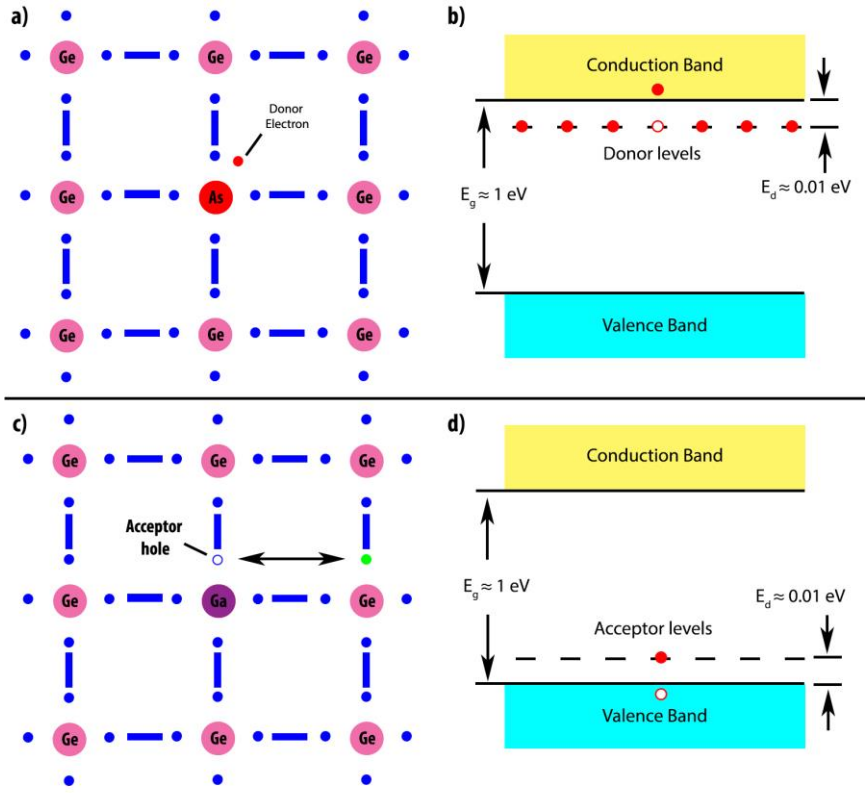

Figure 1.1 a) A n-type As impurity within a bulk Ge lattice, providing a donor electron to the system. b) The associated energy band diagram, n-type, where an electron has been excited from the donor level c) A p-type Ga impurity within a bulk Ge lattice, as Ga has only three electrons an electron has been stolen from an adjacent Ge leaving an acceptor hole. d) The associated energy band diagram for a p-type semiconductor where an electron has been accepted in the acceptor level forming a hole in the valence band.

The applications of nanowires are still being realised, however, as previously stated, there has been significant progress regarding semiconducting nanowires. For certain materials the mechanical properties of small diameter nanowires have been proven to be greater than their bulk counterparts. An example of such is ZnO, a semiconductor with a direct wide band gap of 3.37 eV. It has been shown by Wen, that the tensile strength of ZnO nanowires increases for smaller diameters, exhibiting values of up to 40 times that of the bulk material.[31]

One direct application of semiconducting nanowires are nanowire field effect transistors (FETs). A FET is a transistor that uses an electric field to control the electrical behaviour of the device. This device has been recreated on the nanoscale through the application of n-type and p-type doped semiconductor nanowires with the device consisting of a source, drain and gate. They can be generalised into two categories: junction FETs (JFETs) and metal oxide semiconductor FET (MOSFET).[32-33]

Within a JFET the drain and source will be comprised of one material, p- or n- type, and the gate the other, Figure 1.2 a. Therefore, the main current flow throughout the device is either electrons through the n-type semiconductor or holes through the p-type. As a voltage is applied between the gate and source, the associated pn junction becomes reverse-biased and begins to limit the current flow from drain to source. By increasing the gate source voltage the current through the device can be blocked as the depletion region of the pn junction increases eventually, occupying the width of the device.

A MOSFET is similar to a JFET with the source and drain being one type, typically n, the substrate connecting the two regions being the other type and a metal oxide linking all three and attaching to the gate, Figure 1.2 b. A MOSFET can operate in two different modes: depletion and enhancement. Depletion is as described for the JFET, with no voltage applied to the gate, maximum current is achieved between the drain and source. As voltage increases on the gate it increases the depletion region reducing and eventually blocking the drain to source current. Enhancement has the opposite effect, with no voltage applied to the gate the current cannot flow between the drain and source. This makes the conductance of the device voltage dependent, therefore a greater gate voltage leading to higher currents.

The manipulation of a nanowire into such a device as a MOSFET is achieved through the utilisation of axial and radial heterojunctions, allowing for the combination of n- and p-layer materials.[34-35] The main challenges currently faced, with respect to device generation,

are increasing the range of materials available for deposition, increasing the uniformity of nanowire growth/coverage and decreasing the diameter of the nanowires.

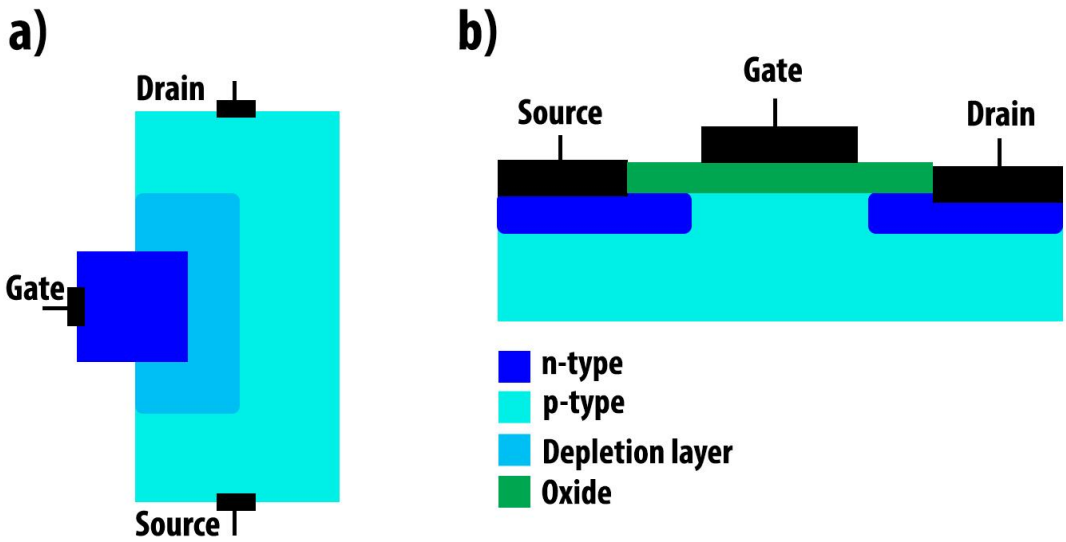

Figure 1.2 a) N-type JFET, electric current flows from the source to the drain and is restricted by a reverse bias applied to the gate generating a depletion zone within the n-type material. b) N-type MOSFET, a setup very similar to the JFET with current flowing from source to drain and a depletion zone controlled by the reverse gate voltage.

1.2.2 Electrodeposition from a Supercritical Fluid

Electrodeposition is defined as a process in which positively charged ions are deposited onto the surface of a negatively charged electrode due to the passage of electrical current.[36] For this process to occur there must be a medium for the current to flow through, this is predominantly an aqueous solution.[37] The solution must be conductive and is prepared so that it contains the ionic species of the deposition material, usually a salt. An example deposition of the salt solution of $CuSO_4$ is shown in Figure 1.3, in which the negatively charged cathode attracts the positive ions, in this case Cu^{2+}.[38] Once the Cu^{2+} ions make contact with the electrode, they undergo ion reduction through electron gains forming solid Cu on the electrode.

Nanowires can be formed through electrodeposition by confining the deposition medium within an insulating template structure. The most common template is anodized

aluminium, with deposition reported as early as 1975 by Kawai but becoming popular in the early 90s from the deposition of Fe by AlMawlawi.[39-41] Anodizing is a widely used industrial process developed to increase corrosion resistance in alloys.[42] The anodized aluminium layer is formed by passing a direct current through the aluminium whilst using a range of acids as the electrolytic solution.[43] The electrochemical reaction releases oxygen at the anode in the aluminium forming an insulating aluminium oxide (alumina) surface.[44] The oxide forms in a self-organising, honeycomb structure generating a high density array of uniform and parallel nanopores.[45] The pore diameter is controlled by the choice of electrolyte and cell potential, an example being pore diameters of 60, 95, and 450 nm obtained in sulphuric, oxalic, and phosphoric acid solutions under voltages of 25, 40, and 160 V, respectively.[46]

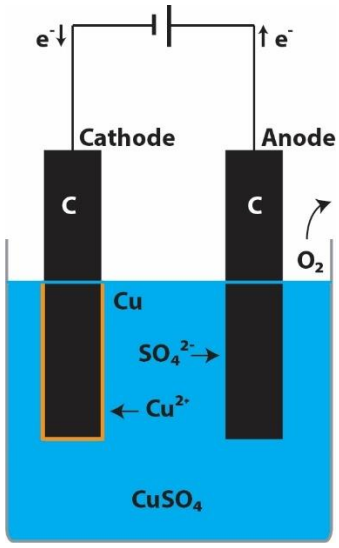

Figure 1.3: Aqueous electrodeposition of Cu from a $CuSO_4$ salt solution onto a C electrode.

Anodic alumina is an ideal deposition template as no electrochemistry occurs at its surface as it is an insulator. An electrode is sputtered onto one side of the alumina, creating an electric contact within the template. The template is submerged into the electrodeposition medium with the electrode insulated from the electrodeposition medium apart from inside the pores. The resulting electrochemistry generates bottom-up nanowires originating within the nanopore at the interface between the electrodeposition medium and the electrode,

illustrated in figure 1.4.[47] This has been utilised to form arrays of singular, binary and ternary composition nanowires with diameters ranging from greater than 100 to 9 nm.[48-52] Standard aqueous electrodeposition from a water based medium is limited by the boiling point of water and its narrow potential window. A aqueous electrodeposition into nanopores, with diameters < 10 nm, is limited by the surface tension of the liquid, which prevents the liquid from penetrating into the pore and contacting the electrode.[53]

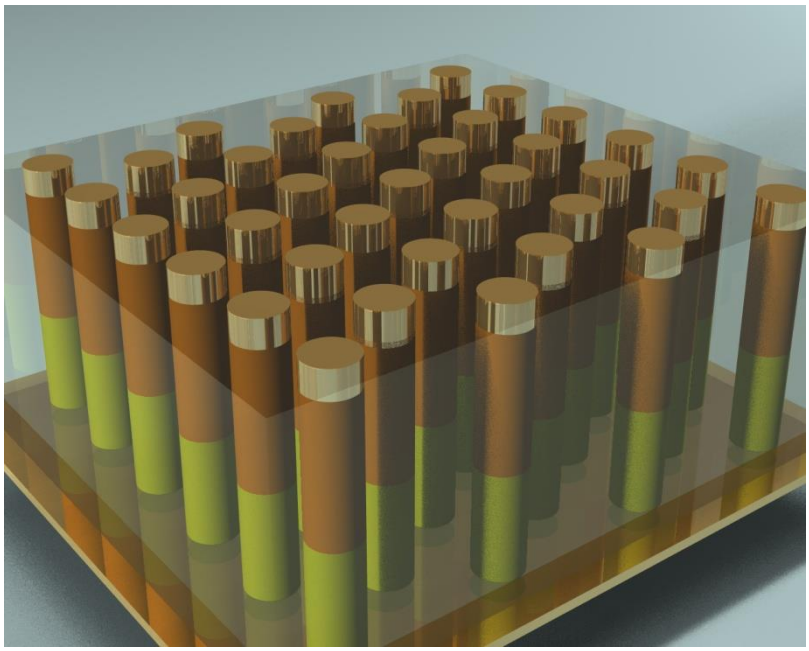

Figure 1.4: Illustration of a high-density nanowire array formed through electrodeposition into a porous anodic alumina template. The nanowires are formed in a bottom-up process originating at the gold contact within the pores.

A supercritical fluid (SCF) can be used as an alternative electrodeposition medium to overcome the limitations faced by standard aqueous deposition. A SCF is a phase of matter at a temperature and pressure above its critical point. This region is located between the gas and liquid phase interface, figure 1.5, in which the phase loses distinction between being a gas or a liquid embodying properties of both phases, explored in table 1.2.

The degree of which phase the SCF is more akin to depends on the pressure and temperature, this ability makes a SCF a “tuneable” solvent. As it is no longer a liquid, a SCF

has no surface tension and high rates of mass transport whilst maintaining a large density, this allows for penetration into < 10 nm nanopores and electrodeposition to occur. This is known as supercritical fluid electrodeposition (SCFED).[54]

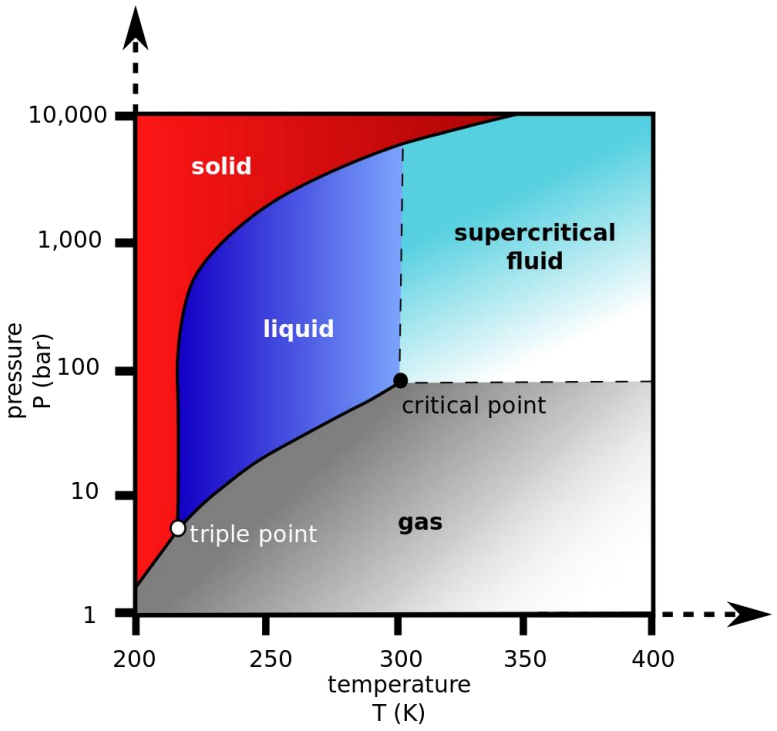

Figure 1.5: Phase diagram for carbon dioxide highlighting the phase separations dependent on temperature and pressure.

	Density (kg/m^3)	**Viscosity (cP)**	**Diffusivity (cm^2s^{-1})**
Gases	1 – 100	0.01 – 0.05	$10 – 10^3$
Supercritical Fluids	100 – 1000	0.05 – 0.1	1 – 10
Liquids	1000	0.5 – 1.0	10^{-5}

Table 1.2: Example of the value range of different properties for a SCF with relation to gases and liquids.

The SCF used for electrodeposition contains a background electrolyte combined with the deposition solvent and a supercritical base. SCFED is undertaken using supercritical difluoromethane (CH_2F_2, also known referred to as scR32), however the low dielectric constant and conductivity of the fluid hinder the deposition process.[55] To compensate for

this, a background electrolyte is used, as they have been found to increase the conductivity of the solution, an example of such is 1-ethyl-3-methylimidazolium tetrafluoroborate.[56] The target deposition material is then combined with the background electrolyte before the solution is dissolved into the SCF.

Due to the increased pressure and temperature required to sustain a SCF, all electrodeposition must be undertaken within a cell, similar to the bath used for aqueous deposition.[57] The cells need to be durable and able to withstand high pressures whilst incorporating the electrical throughputs and connectors that make SCFED possible.

1.2.3 Melting and Sublimation

Modern phase transitions are categorised into two broad groupings defined by Ehrenfest as First-order and Second-order phase transitions.[58] Second-order phase transitions are known as continuous phase transitions as they are characterised as providing a continuous change in entropy.[59] An example of such is the phase transition from a paramagnet to a ferromagnet, this occurs above the Curie Temperature where the ordered spin aligned electrons in the ferromagnetic domains become randomly aligned creating the phase transition to paramagnetic.[60]

First-order phase transitions are described as involving latent heat in which a system either absorbs or releases a fixed amount of energy per volume.[61] During a phase transition, whilst heat is added to or removed from a system, the temperature of the system will remain constant. An example of such is shown in Figure 1.6 highlighting the temperature of water as it is heated over time. Periods of constant temperature are observed where heat flows into the system but the temperature does not increase, this is due to the heat being used to perform the phase transition and not to increase the temperature of the system.

The Gibbs free energy is defined as the maximum reversible work that may be performed by a system at a constant temperature and pressure.[62] The plateaus observed in

Figure 1.6 are the defining feature of a first-order phase transition as the first derivative of the Gibbs free energy, G, is discontinuous across the phase boundary. The function, *G*, is defined as

$$G = U - TS + PV \qquad (1\text{-}1)$$

Where *U* is the internal energy, *TS* the temperature multiplied by the entropy and *PV*, the pressure multiplied by the volume. *G* incorporates the internal energy of the system and the natural tend of a material towards disorder, so *G* is not purely trying to obtain its minimum energy state.

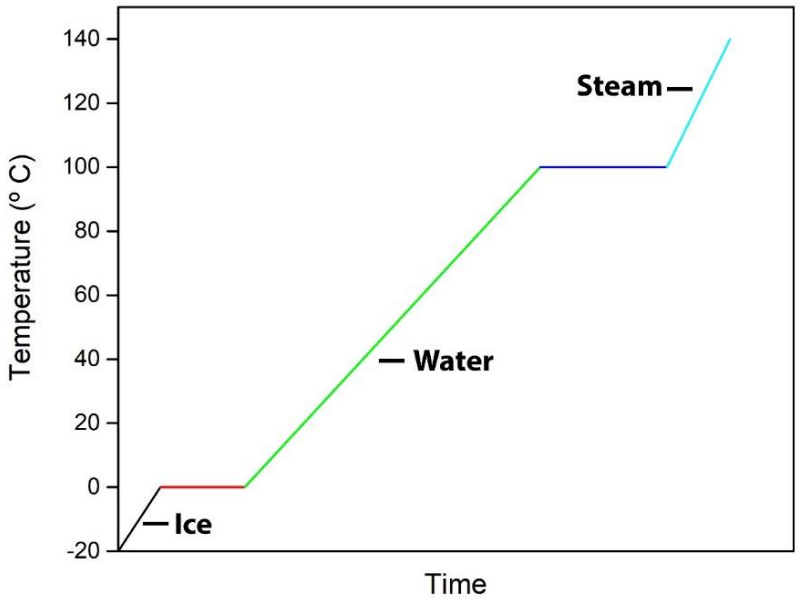

Figure 1.6: Graphical representation of the temperature of water under constant heat as a function of time. Temperature plateaus are observed at phase changes where the heat energy is used to phase change the material instead of increasing its temperature.

For a small change in *G*

$$dG = dU + PdV + TdP - TdS - SdT \qquad (1\text{-}2)$$

The first law of thermodynamics states that $dU = dQ + dW$. The definition of entropy states that $dQ = TdS$ and the negative work done in expanding by dV is represented by $dW = -PdV$.

The substitution of *dU* into equation 1-2 simplifies the change in Gibbs free energy

$$dG = VdP - SdT \qquad (1\text{-}3)$$

Assuming that the phase transition is being undertaken under a constant pressure then the gradient of the Gibbs energy with respect to temperature at a constant pressure is the negative of the entropy *S*, equation 1-4.[63]

$$\left.\frac{dG}{dT}\right|_P = -S \qquad (1\text{-}4)$$

This is as expected from a phase change where a system, for example, goes from a condensed solid phase into a dispersed liquid phase. The molecular disorder is much greater within the liquid phase and therefore requires a substantial entropy change.

The direct phase transition from solid to gas with no intermediary liquid phase is known as sublimation. This phase transition, whilst uncommon under standard atmospheric pressures, becomes more potent in high vacuum conditions due to the vapor pressure of a material becoming unstable. Vapor pressure is a measure of the pressure exerted by a materials vapor over its liquid or solid state at equilibrium for a given temperature in a closed system. Due to the energy distribution of particles within a material following a Maxwell-Boltzmann distribution, some particles will have sufficient energy to escape the surface of the material. For a closed container as the quantity of vapor increases so does the quantity of particles colliding with the surface of the material and returning to the bulk. This will continue until the rate of particles escaping the surface equals the rate of particles returning. At this point the vapor is said to be saturated. As the temperature of a material increases, so does the kinetic energy of its particles. This allows more particles to transition into the vapor increasing the vapor pressure.

Solids are normally in a state of equilibrium, as the rate of vapor condensation is equal to the rate of vaporisation. However, under high vacuum as the temperature of a system

increases, so does the kinetic energy of the particles, this increases the quantity of surface vapor and consequently the vapor pressure can become greater than the local pressure. At this point vapor particles will be removed to the vacuum and, with no external pressure, the bulk substance will transition from solid to gas.

The vapor pressure, P_v, of a material can be calculated from the Antoine equation where

$$log_{10}(P_v) = A - B/(C + T) \qquad (1\text{-}5)$$

A, *B* and *C* are material dependent constants and T is the temperature. This semi-empirical relationship is derived from experimental observations and originally presented by Antoine in 1888.[64] The Antoine equation is a modification of the Clausius-Clapeyron equation which characterises the gradient of the vapor pressure curve at a phase transition.[65] Again this relationship examines the thermodynamics at the phase transition where

$$\frac{dP}{dT} = \frac{\Delta s}{\Delta v} \qquad (1\text{-}6)$$

$\frac{dP}{dT}$ is the gradient of the vapor pressure curve, Δs the entropy change specific to the phase change and Δv the volume change specific to the phase transition. The Antoine equation is derived from equation 1-6 by substituting $\Delta s = \frac{\Delta H}{T}$, assuming ideal phase behaviour and substituting $v = \frac{RT}{P}$ (equation 1-7) and integrating (equation 1-8)

$$\frac{dP/P}{dT/T^2} = \frac{\Delta H}{R} \qquad (1\text{-}7)$$

$$lnP = A - \frac{\Delta H}{RT} = A - \frac{B}{T} \qquad (1\text{-}8)$$

A is a constant of integration and $B = \frac{\Delta H}{R}$ where ΔH is the latent heat and R the universal gas constant. Equation 1-8 is modified with the constant C, equation 1-5, as this proves more accurate at higher temperatures.

The rate of sublimation was first described in two separate publications by Hertz and Knudsen in the early 1900s.[66-67] Their combined equation, though derived for condensation, represents the number of gas molecules passing through a unit area per second with a Maxwell-Boltzmann distribution. Described below as equation 1-9, $\frac{dN}{dT}$ is the flux of molecules

$$\frac{dN}{dT} = \frac{(P_v - P)A}{\sqrt{2\pi nkT}} \qquad (1\text{-}9)$$

P_v and P, the vapor pressure and system pressure, A the surface area of the sublimation front, m, the mass, k, Boltzmann's constant and T the system temperature. The assumption that the distribution is Maxwellian is well established as the gas particles are expected to move freely, undergoing very few collisions with each other, with the particles main interactions being with the container walls.[68]

The experimental rate of sublimation is often observed to be imperfect with the theoretically rate of sublimation not equalling the experimental rate.[69] Langmuir suggests that this is due to impingement of the sublimed molecules back onto the sublimation front.[70] This is accounted for by the incorporation of α, a correction/accommodation coefficient.[71] The correction coefficients found, though empirical, have shown a high degree of accuracy.[72-74] Drawbacks from this calculation are the assumptions of a high degree of accuracy for both the temperature and pressure at the sublimation interface. Therefore, it is expected that this value may fluctuate as a function of the accuracy of these variables.

1.2.4 Filled Carbon Nanotubes

Discovered in the early 90s by Sumio Iijima and quickly hailed as a "wonder material", carbon nanotubes (CNTs) are formed from a sheet of rolled graphene, often with a diameter less than 10 nm.[75] If the CNT consists of one independent CNT constructed from a single graphene sheet then this is classified as a single-walled nanotube (SWNT). CNTs can form from multiple rolled layers of graphene, these are classified as multi-walled nanotubes (MWNT). The theoretical properties of SWNTs were quickly established, indicating, among other things, high electrical conductivity, tensile strength and thermal conductivity.[76-79] Over the next decade these properties were verified experimentally, examples of such are an average Young's modulus of 1.8 TPa in < 10 nm SWNTs and conductivity/resistance measurements indicating that a nanowire's diameter or geometry generates either metallic or non-metallic behaviour.[80-81]

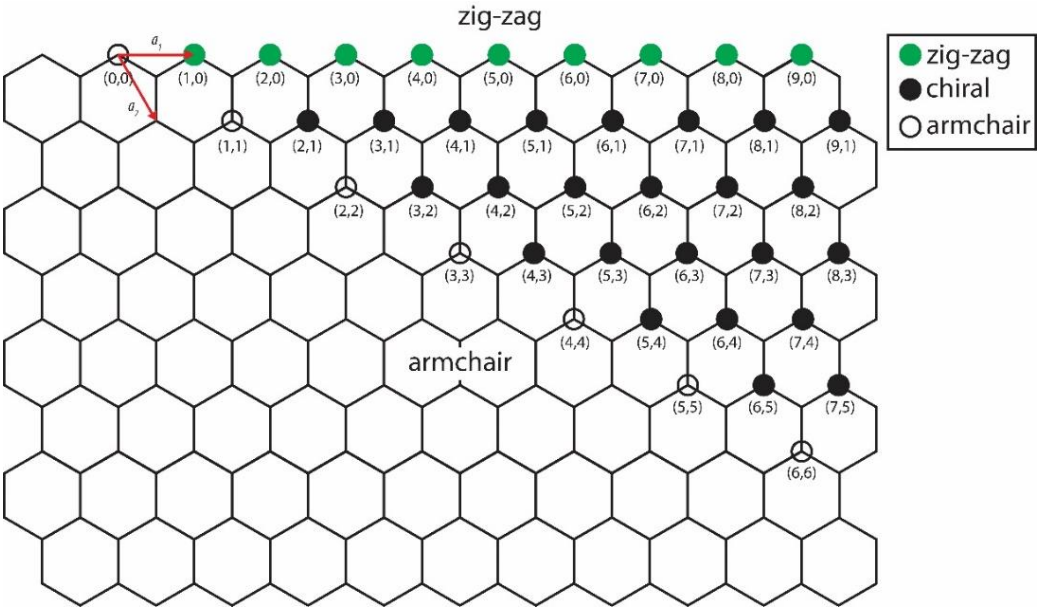

Figure 1.7: Illustration of the carbon-carbon coordinate system leading to the SWNT geometry identification. The unit vectors a_1 and a_2, used to define the wrapping vector of the SWNT, are highlighted on the C origin atom.

A SWNT consists of a graphene sheet of sp^2 bonded carbon rolled into a cylinder. The graphene sheet itself is formed from a repeating hexagonal C lattice, with the C atoms

covalently bonded.[82] To differentiate SWNTs they are categorised with respect to their wrapping vector. The wrapping vector is expressed as (m,n), this is in relation to the unit cell, *v*, of the SWNT where m and n are integers relating to the unit vectors a_1 and a_2 where

$$v = na_1 + ma_2 \qquad (1\text{-}10)$$

The wrapping vector is important as it defines the metallic or semiconducting properties of the SWNTs.[83] There are three unique geometries of carbon nanotube: zig-zag (n,0), armchair (n=m) and chiral (n,m). The vector coordinate system is illustrated in Figure 1.7 in which the wrapping is described by superimposing the origin C atom (0,0) onto the desired SWNT configuration coordinate.[84]

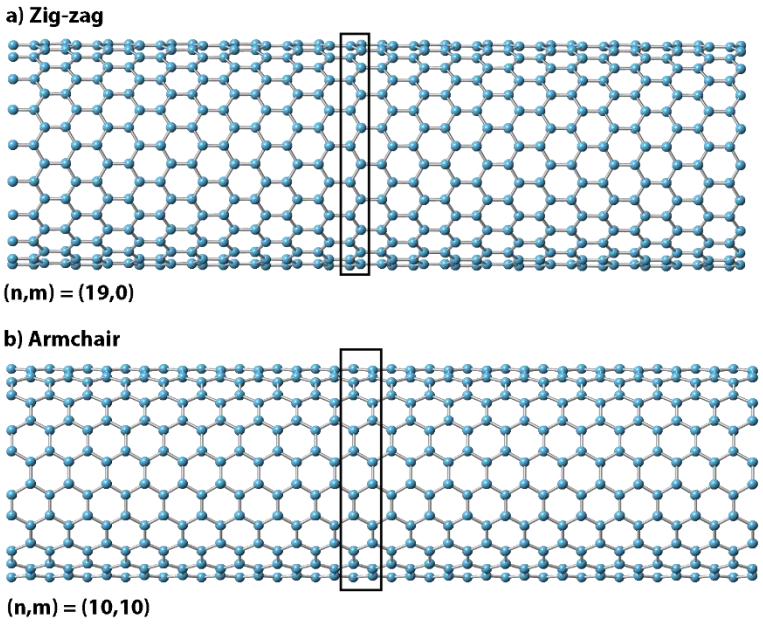

Figure 1.8: Visualisation of an individual zig-zag (a) and armchair (b) SWNT. The wrapping vector for each SWNT is included with the circumference motif of which the classification name originates from is highlighted.

The armchair and zig-zag configurations are both observed in Figure 1.7, they follow the two lines of symmetry with the zig-zag running parallel from the origin and at the armchair at 60º. The names are derived from the arrangements of hexagons around the circumference of the SWNT, with the zig-zag C atoms following a 1x1 zig-zag motif (Figure

1.8 a) and the armchair c atoms following a 2 up 2 down motif (Figure 1.8 b). Any configuration that falls between zig-zag and armchair is classified as chiral.

SWNTs were traditionally formed using arc-discharge evaporation in which a current was applied across two carbon-based electrodes in an inert gas atmosphere.[85] As the graphitic rods erode a by-product is single and multi-walled CNTs. Using this method with a cobalt catalyst can result in mostly defect free CNTs, with a diameter range of 1 – 20 nm and average lengths of a few microns.[86] Alternatively chemical vapor deposition (CVD) is used as a bulk long length CNT production method. Here the flow of a carbon-containing gas over catalyst nanoparticles stimulate CNT formation at high temperatures. The CNT diameter distribution from CVD is typically 10 – 100 nm, yet extremely long lengths of ≈ 60 μm have been consistently reported and bulk formation is much easier.[87]

The encapsulation of a material within a carbon nanotube was predicted by Pederson in 1992 and experimentally reported by Ajayan in 1993 with the capillary melt filling of lead into MWNTs.[88-89] He experimented with opening the CNTs by heating to allow entry for the filling material. From this he discovered that the CNTs must be heated in air to remove the carbon caps from the CNTs opening them up for filling. The Pb filling percentage was reported as quite low and the resulting encapsulated material is believed to have oxidised as the structure could not be identified.[90]

After the discovery of filling a range of systems have been examined using TEM, examples of such being palladium and nickel, however structural determination is often ignored due to TEM limitations.[91-92] This was overcome through advancements in electron microscopes and the introduction of aberration correction in the early 2000s. In 2000, Meyer reported the first case of atomically resolved high-resolution TEM, acquiring images of encapsulated potassium iodine within CNTs.[93]

For encapsulation within large nanowires, typically greater than 5 nm, the reported crystal structure when identified is predominantly equal to the bulk lattice structure.[94-95] This is not always the case when encapsulation occurs within small CNTs. If a CNTs diameter is less than 2 nm, the van der Waals surface of the CNT can create an internal confining volume that is too restricted for the bulk crystal structure to form.[96-97] When this is the case, then identification of the crystal structure becomes complex and novel crystal identification practices are required.

The standard protocol for encapsulated crystal identification is visual comparisons to the bulk structure. However, as this is a semi-empirical relationship, it can easily generate bias. A potential alternative to this is *Ab Initio* Random Structure Searching (AIRSS), a first principles structural search procedure that can predict, for a range of boundary conditions, the most stable crystallographic configuration from their associated potential energies.[98] The first reported case of this method was undertaken by Pickard in 2006.[99] The guiding principle behind the random structure search is that nothing is known about the structure and therefore some random structures should be generated and then relaxed to cover the widest range of potential energy surfaces.

1.3 Thesis Outline

In this thesis, electron microscopy has been used as the primary characterisation technique to aid in the structural and elemental characterisation of a range of nanowires and materials. A full spectrum of machines and techniques were used to analyse the nanowire properties, as described in Chapter 2. Key experimental results are verified through comparisons with alternative experiments, theoretical analysis and simulations.

Firstly, in Chapter 3, the ability to deposit materials using SCFED is examined starting at the micron scale, with a Ge film, through to ≈ 6 nm Sn nanowires. The need for electron microscopy as a characterisation technique is proven with respect to analysing the

crystallinity, elemental composition and diameters of the deposited films and nanowires. Included in this section is what is thought to be the first atomically resolved images of a Cu_6Te_3S nanowire.

Moving on from broad characterisation, Chapter 4 focuses on the effects of heating nanowires in situ. Here Bi and Te are heated to observe the solid to liquid phase transition. When heated under vacuum, Te is reported to not melt, with the system undergoing sublimation. The in situ sublimation process is recorded so that comparisons can be drawn between the experimental and theoretical rate of sublimation. The expected phase transition from solid to liquid is observed for the Bi system. As the liquid Bi remains encapsulated within alumina, radial distribution function (RDF) analysis was implemented to probe the average atomic spacing of the liquid Bi. The RDF results prove that this form of analysis provides results on par with XRD and neutron scattering.

Chapter 5 highlights attempts to make one-dimensional crystals through the encapsulation of materials inside CNTs. Continuing with the systems explored in other chapters, the effect of encapsulation on crystal structure is focussed upon. Initially systems are examined with HRTEM and STEM and compared to their bulk structures. AIRSS is successfully used for the first time to generate the encapsulated structures from first principles and lowest energy analysis.

Experimental Methods

2.1 SCFED Based Sample Preparation

All SCFED samples were created in Southampton, using the process outlined in Chapter 1.2.2. and the relevant solvent concentrations documented in each relevant results section. The background electrolytes used to increase the conductivity of the solution are either 1-ehtyl-3-methylimidazolium tetrafluoroborate ([EMIM][BF_4]) or tetrabutylammonium ([N^nBu_4]). The nanowires must be released from their templates to allow for imaging in the TEMs. This is predominantly undertaken by dissolving the template in a strong base. First they are immersed in 4 M NaOH for 1-3 minutes, whilst still attached the residual gold or platinum contact. The nanowires are then washed with deionised water and isopropyl alcohol (IPA). The wires are suspended in IPA by sonication and drop cast onto a 3.05 mm copper or nickel grid with a lacy carbon support film (Agar Scientific). Alternatively, samples may be prepared via the Focussed Ion Beam, as described in Chapter 2.3.2.

2.2 Filled Carbon Nanotubes

2.2.1 Nanotube Preparation

Two sources of SWNTs have been used as they provide a slight variation in diameter range. NanoIntegris NI96 with a diameter range of 1.2 - 1.6 nm and Sigma-Aldrich SWeNT nanotubes with a diameter range of 0.7 – 1.1 nm. The NI96 SWNTs arrive in an aggregated bucky paper state and must be redispersed for filling experiments. This is achieved by placing the bucky paper in chloroform and sonicating at 20 % power, with 2 second bursts, for 30 minutes of active sonication. After this the mixture is then filtered using a porous film and vacuum flask to draw all the chlorine out of the system and then dried in a vacuum flask. This process may be repeated if the nanowires are not dispersed enough after filtration.

The SWNTs are then placed on a ceramic boat and baked under air at 480 °C for 45 minutes. This opens and thins the nanotubes through oxidation, destroying carbon caps on the nanotubes and opening then for filling.[100-101] A mass loss of ≈ 20 % is expected under these conditions. Literature would suggest a longer baking time, however, baking at > 700 °C for approximately 1 hour results in a mass loss of ≈ 80 %. This is due to the commercially produced SWNT having already undertaken an initial purification, therefore this reduced method is a measure to remove any impurities that have built up since then.

2.2.2 Capillary Melt Filling

The capillary melt technique is well established as a way of filling carbon nanotubes.[90, 102] A weighed out mass of SWNT is ground together with the desired filling material by pestle and mortar under an inert argon atmosphere in a glovebox. After 30 minutes of grinding, the combined sample is inserted into a silica quartz ampoule and sealed under vacuum. The combined sample is then heated in a tube furnace using a thermal cycling procedure. Following the initial ramp to the filling temperature, this protocol involves thermally cycling the sample above and below the melting temperature before the final cooling segment. An example heating procedure is shown in Figure 2.1 with Table 2.1 highlighting the quantities used and ramping procedure. The ramping procedure allows the liquid filling material to penetrate the SWNTs and recrystallize within it. The samples were judged to be "ready" via visual inspection, looking for proof of solid to liquid transitions from mass dispersion. The dispersal method to prepare samples to be imaged is discussed in Section 2.2.4.

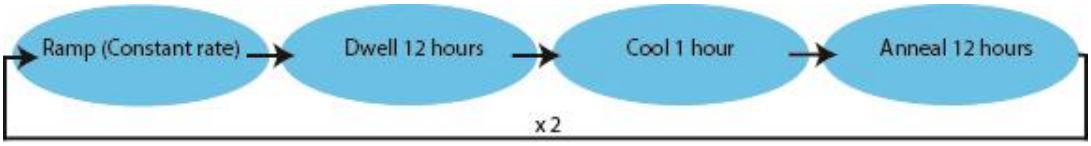

Figure 2.1: Example of a ramp heating procedure. Repetition of the heating cycle is enforced to ensure a high filling rate.

Material	Filling mass (mg)	SWNTs mass (mg)	Dwell temperature (°C)	Heating protocol	Repeat
Ge	60	34	980	Ramp (6hrs) - dwell (6hrs) – cool (1hr) – anneal (5 hrs, 900°C)	2
Sb_2Te_3	30	9	620	Ramp (4hrs) – dwell (6hrs) – cool (1hr) – anneal (4 hrs, 560°C)	3

Table 2.1: Examples of experimental conditions for melt filling experiments for Ge and SbTe. The mass of filling material and SWNTs is measured prior to grinding. The furnace heating protocol is provided with duration and temperature.

2.2.3 Sublimation Filling

An extension of the capillary method involves sublimation with mass transport along temperature gradients. Filling material is placed in one end of a double chamber sublimation ampoule with SWNTs placed in the other, a neck between the two chambers prevents mixing. The ampoule is sealed under vacuum and kept horizontal at all times before being placed into a tube furnace. Tube furnaces have a temperature gradient; the centre of the tube is the constant temperature zone, with the temperature decreasing towards each end of the tube. A multi-zone tube furnace can be used to impose a greater degree of control over the temperature gradient. With the filling material in the hot zone, when heated above its melting temperature under vacuum, it will sublime and transport down the sublimation ampoule and recrystallizing within the SWNTs. Proof of recrystallization is observed in the cooler end of the ampoule by the observation of microcrystallites around the SWNTs, an example of such is shown in Figure 2.2.

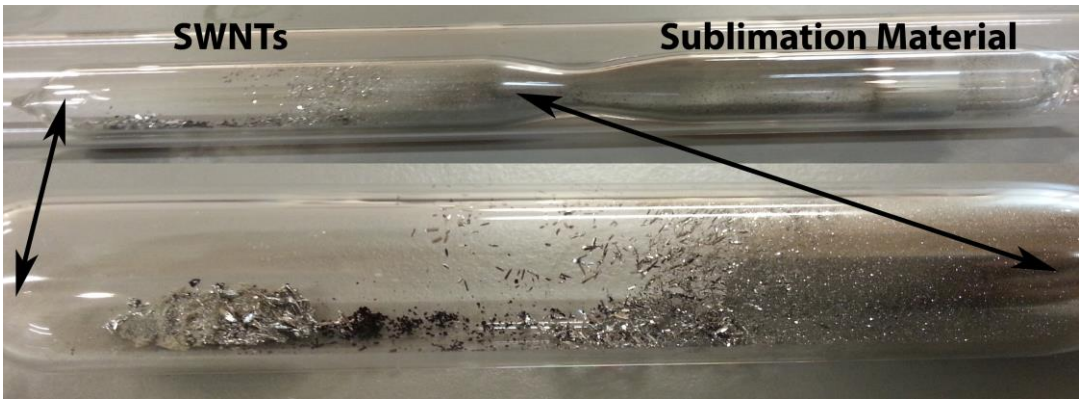

Figure 2.2: Sublimation ampoule post sublimation. The SWNTs are placed in the left section of the ampoule and separated by a neck from the sublimation material. Proof of sublimation and mass transport is proved by visible microcrystals in the SWNT region after heating.

2.2.4 Specimen Preparation for Microscopy

After the different heating procedures for the sublimation and melt filling samples, they are both prepared for imaging with the same procedure. The ampoule is opened by scratching a fault into the quartz with a file and snapping the ampoule along the fault. Once opened, a small quantity of sample, ≈ 1-2mg, is dispersed in 10ml of ethanol or chloroform and sonicated for 20 minutes. Dispersion is confirmed visually by the dispersion liquid becoming cloudy and the breaking of SWNT bundles. Once dispersed a single drop is pipetted onto a lacey carbon grid and dried under a heat lamp.

2.3 Microscopy

2.3.1 Scanning Electron Microscopy

Optical microscopy cannot be used to image samples as its lateral resolution is limited by the Rayleigh Criterion[103]. This defines the resolution of an optical microscope as the minimum distance, *r*, between two points, at which both points can be distinguished individually.

$$r \approx \frac{0.61\lambda}{n_a} \qquad (0\text{-}1)$$

Where λ is the wavelength of light and n_a is the numerical aperture used. This limits the lateral resolution of an optical microscope to ≈ 250 nm, therefore, this technique cannot be utilised for systems with dimensions smaller than this.

Electrons can be used as an electromagnetic radiation source instead of light.[104] Formulated by de Broglie, the nonrelativistic wavelength of electrons, λ (Å), is determined by the voltage, E (eV), it is accelerated by where

$$\lambda = \frac{2\pi\hbar c}{pc} \approx \sqrt{\frac{150}{E}} \qquad (0\text{-}2)$$

This principle is the basis behind SEM, Figure 2.3. Electrons are emitted from an electron source, typically a tungsten filament or field emission gun (FEG), with a voltage between 1-20 keV. The beam is condensed to a spot of 0.5 – 5 nm by lenses in the gun column and rastered across the sample. Using the electron source instead of light, the resolution within the SEM ≈ 1 nm - small enough to image nanowires but not enough for atomically resolved imaging.

The incident electron beam interacts with the sample via the interaction volume, producing secondary electrons, backscattered electrons and electromagnetic radiation. The interaction volume is the region from which signals can be detected from and is illustrated in Figure 2.4.[105] Secondary electrons (SE) are the primary source for imaging, they are produced when the electron beam interacts with the sample causing ionization of loosely bound electrons. SE are extremely surface sensitive with a small penetration depth, typically <100nm, dependent on the accelerating voltage and sample. The SE image has high spatial resolution, as due to this small sample volume, little noise from non-surface electrons reach the detector.

Backscattered electrons (BSE) are the result of elastic collisions between the incoming electron beam and the sample atom. This generates atomic number related contrast, as more electrons are scattered from bigger, heavier nuclei creating brighter contrast in the

images. The lateral resolution of BSE images is ≈1µm due to the high energy elastic collisions causing an interaction depth of approximately 1µm. Electromagnetic radiation is also released in the form of X-rays and once detected allows for elemental analysis by Energy-dispersive X-ray Spectroscopy (EDX). The interaction volume for X-rays is the greatest as they are not easily absorbed, this generates a penetration depth of up to 10 µm. This technique is described in more detail in Section 2.4.1.

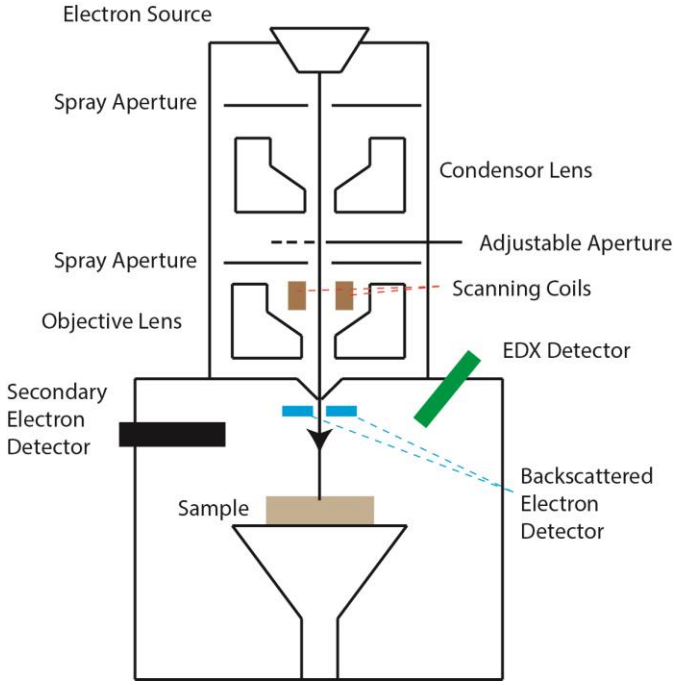

Figure 2.3: Schematic diagram of a standard scanning electron microscope. Spray apertures are installed to reduce electron beam spread from propagating through the microscope. The rastering of the beam is controlled by the scan coils.

The SEM used is a Zeiss Supra 55VP SEM, with an accelerating voltage between 1 – 20 kV. It is fitted with a FEG source and an EDAX Genesis analysis system. If a material is non-conducting, it will suffer heavily from charging effects. The build-up and uncontrolled discharge of electrons from the sample leading to image distortion. This is countered by carbon coating and applying silver dag to the edge of the sample.

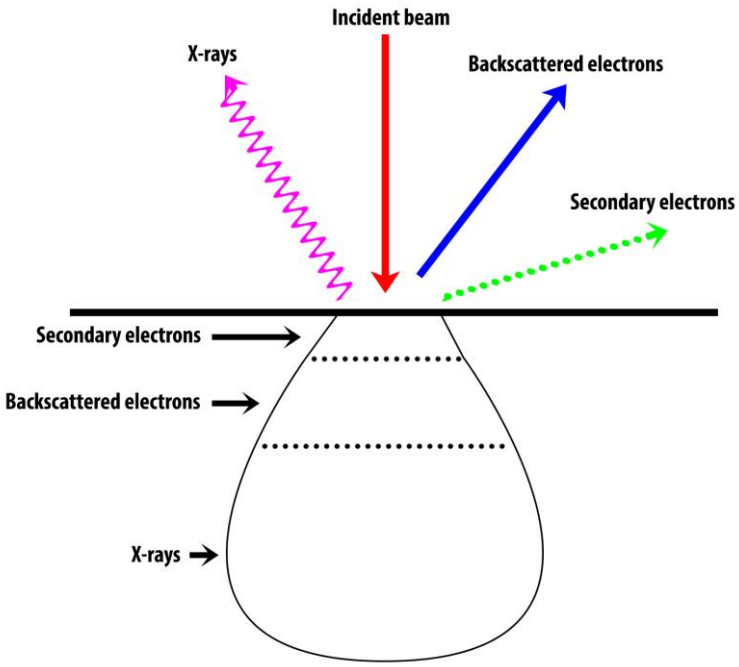

Figure 2.4: Example of the signals produced inside the SEM with the interaction volume.

2.3.2 Focused Ion Beam

Certain samples cannot be released from the alumina, an example of such being investigations on the interface between the nanowire and the gold contact. When traditional cross-section or planview samples are required, mechanical polishing is extremely challenging due to the small dimensions of the samples, typically 2 mm by 1 mm with a depth of 50 μm. To combat this samples are prepared using a Focused Ion Beam (FIB) milling technique.

A dual-beam FIB combines an SEM with an ion source, mounted at 52° with respect to each other, that allows for nanoscale milling and deposition.[106] The ions are generated from a liquid metal ion source. In which, Ga is placed in contact with a tungsten needle, wetting the Ga and allowing it to flow to the tip of the needle. There, it is ionised by an electric field and accelerated towards the sample. The Ga^+ interacts with the sample in a similar way to the SEM, producing secondary electrons and secondary ions.

The three principle operations of the FIB are: imaging, milling and deposition. When operated at a low beam energy, the imaging system is identical to a SEM, with the image made up of secondary electrons produced via an interaction with the Ga^+. At higher energies, the Ga^+ will interact with the surface atoms and sputter them, ejecting them from the sample via a momentum transfer and producing a milling effect. By rastering the beam across a designated region, this effect can be controlled and manipulated to actively mill a sample, and for our purposes thin it down to <50nm and electron transparency. Deposition occurs when a gas precursor is adsorbed onto the surface of the sample. It then reacts with the Ga^+, dissociating the molecule, leaving a deposited desired material, whilst the volatile excess is lost to the vacuum.[107]

The standard sample preparation method is the "lift-out" technique, a combination of different modes of operation, which with the aid of a micromanipulator probe allowing for a cross section sample to be prepared.[108] For this a JEOL 4500 dual-beam FIB/SEM with a 30 kV LaB_6 SEM electron source, 30 kV Ga^+ ion source and a phenanthrene ($C_{14}H_{10}$) precursor was used.

2.3.3 Transmission Electron Microscopy

With a resolution of ≈ 1 nm, SEM and FIB are limited with respect to detailed, high-resolution, high-magnification imaging. For this Transmission Electron Microscopy (TEM) is required. TEM is a technique similar to SEM in terms of the electron source and optics system. Differences arise from the image formation within a TEM. Here, image formation derives from electrons that are transmitted through the sample in a parallel beam, instead of detecting secondary electrons from a probe source. Another key difference is the much higher accelerating voltages of 80KeV and 200KeV.

The TEM column can be separated into two systems: the illumination system, consisting of the electron source, condenser lenses, upper objective lens and specimen; and

the imaging system, including the specimen, objective lens, objective aperture, selective area aperture, intermediate lens, projector lens and screen. The illumination system establishes how the beam will interact with the specimen, for TEM operation an approximately parallel beam is required (Figure 2.5a), whilst for STEM a focussed beam, known as a probe, is required (Figure 2.5b).

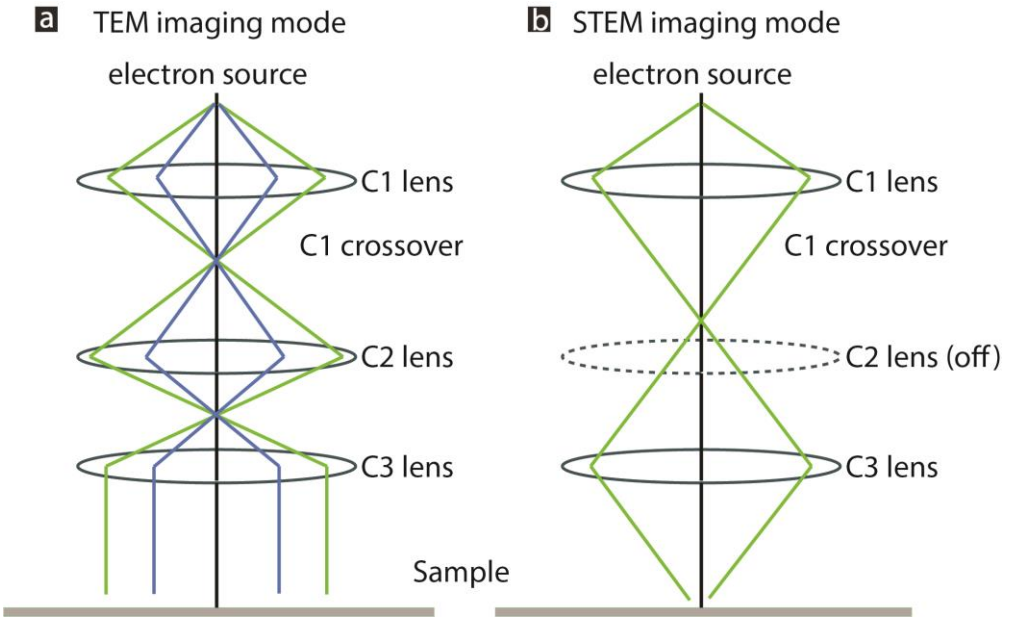

Figure 2.5: The main TEM illumination techniques a) Schematic overview of the parallel beam conditions used for TEM imaging. b) Schematic overview of the convergence beam/probe conditions used for STEM imaging.

The imaging system operates in predominantly two ways manipulating the parallel beam, exiting the sample to form either an image of the sample or a diffraction pattern as shown in Figure 2.6 a and b respectively. An image is formed when the electron beam is dispersed by the objective lens. This produces a diffraction pattern in the back-focal plane, which is recombined at the projector lens to create an image and broadcast onto the screen.

A diffraction pattern is the application of wave-particle duality and highly sensitive to the periodic crystal structure of a sample. This is imaged by changing the objective lens strength to form the image in the back focal plane, producing a diffraction pattern at the screen. When a diffraction pattern is viewed, it projects a central high intensity spot,

containing the direct electron beam, and scattered spots reflecting the crystallinity of the sample, Figure 2.6b. A standard TEM image is formed by isolating the central spot with an objective aperture, this forms what is known as a bright-field image and can be viewed in image mode, ray diagram Figure 2.6a. A dark-field image is formed in a similar way except that a scattered spot will be isolated with the objective aperture, highlighted by Figure 2.6c.

Bright-Field images form a bright background where the beam has been uninterrupted and will be darker where the beam has been scattered by materials. Dark-field images are formed from the isolation of diffraction spots arising from crystalline regions. This inverts the contrast so regions of vacuum and no signal will now be dark. The main application of this is the ability to image specific crystalline regions through the isolation of crystallographic reflections.

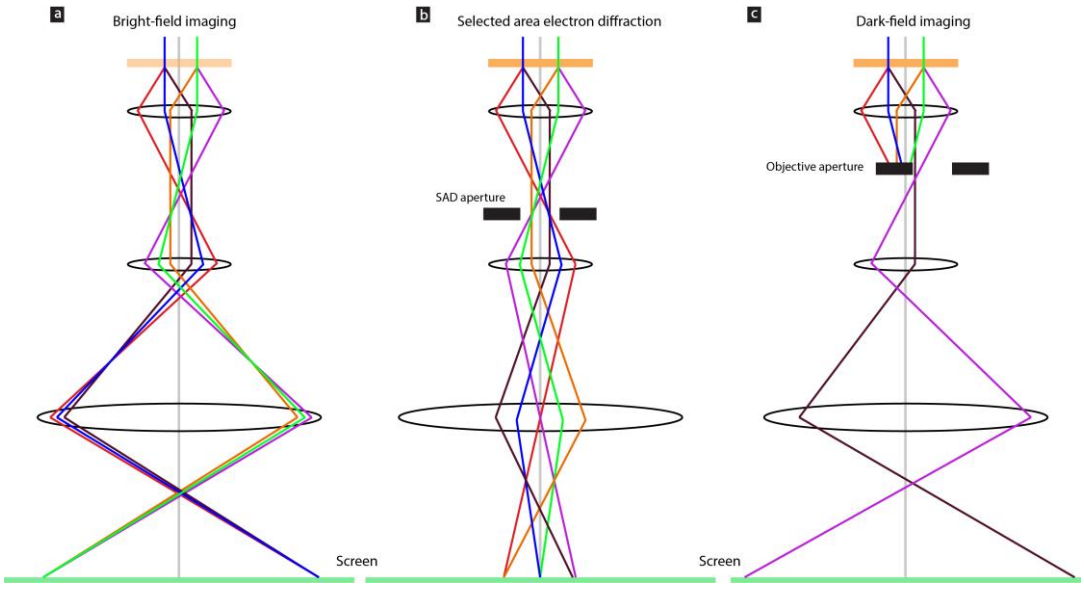

Figure 2.6: Ray diagrams highlighting the three basic modes of TEM operation: a) Bright-field imaging b) Selected area electron diffraction and c) Dark-field imaging.

Contrast in images arise from the interaction of the beam with the sample. This interaction can be separated into amplitude contrast and phase contrast. Amplitude contrast is the contrast arising from variations in mass and thickness. This form of contrast is Z number sensitive, with heavier or thicker elements scattering more electrons. Therefore, in a

BF image, thicker/heavier regions will present a darker contrast than lighter/thinner regions. This is a strong source of contrast within TEM images however it is non-quantitative.

Phase contrast arises from the effect of the atomic structure on the electron plane wave. As an incident electron wave ($\psi_{in}(r)$) passes through a sample it undergoes a phase dependent on the object function $\phi(r)$. This is known as the weak phase object approximation as the specimen only alters the phase of the electron wave.[109] As $\phi(r)$ is proportional to the projected electrostatic crystal potential $V_t(r)$, the exit-plane wave ψ_{ep} can be represented as

$$\psi_{ep}(r) = 1 - i\phi(r) = 1 - \frac{i\pi}{\lambda U} V_t(r) \qquad (2.3)$$

where λ is the relativistic wavelength of the electron, U the acceleration voltage, V_t the projected electrostatic potential of the crystal.

The wave function at the image plane $\psi(r)$ is the inverse Fourier transform $\mathcal{F}^{-1}$ of the wave function multiplied a complex transform function $t(q)$. The Fourier transform relates the back focal plane to the image plane whilst $t(q)$ accounts for the characteristic errors of the objective lens. When multiplied in Fourier space this becomes a convolution, Ⓧ, in real space

$$\psi(r) = \mathcal{F}^{-1}\left[\psi_{ep}(q)t(q)\right] = \psi_{ep}(r) \circledast t(r) \qquad (2.4)$$

The transfer function of the objective lens directly transfers information from the exit-plane into the image plane, playing a crucial role in image formation. The contrast transfer function (CTF) is described by $t_L(q)$ and dependent on the aberration function $\chi(q)$, as described below

$$t_L(q) = exp\left[-\frac{2\pi i}{\lambda}\chi(q)\right] \qquad (2.5)$$

$$\chi(q) = \frac{1}{2}\theta^2 C_1 + \frac{1}{4}\theta^4 C_3 \qquad (2.6)$$

Where in a conventional TEM the aberrations are determined by defocus C_1 and the spherical aberration of the objective lens C_3. When the introduced aberrations are combined with the Rayleigh criterion the limiting factor of the resolution within the TEM becomes the spherical aberration C_3 with

$$r_{min} = 0.91(C_3\lambda^3)^{1/4} \qquad (2.7)$$

Therefore, to realise the full potential of the TEM correctors have been developed to counteract aberrations and push for sub 1Å resolution.

2.3.4 Aberration-Correction

The problem of lens aberrations were described by Scherzer in 1936, who theorized that aberrations cannot be corrected for rotationally symmetric systems.[110] To fix this the rotational symmetry must be broken through the application of quadrupoles, hexapoles and octupoles, however this wasn't realised until the late 90s.[111] Combinations of these electrostatic lenses can be used to apply a negative spherical aberration to the natural positive spherical aberration, which negate each other summing to zero spherical aberration.

Once spherical aberration is corrected, previously ignored aberrations now become more dominant within the aberration function leading to an expansion of equation 2.6 to

$$\chi(q) = \Re\{A_0\overline{w} + \frac{1}{2}C_1 w\overline{w} + \frac{1}{2}A_1\overline{w}^2 + B_1 w^2\overline{w} + \frac{1}{3}A_2\overline{w}^3 + \frac{1}{4}C_3(w\overline{w})^2 + S_3 w^3\overline{w} + \frac{1}{4}A_3\overline{w}^4\} \qquad (2.8)$$

The expanded CTF now includes aberrations up to the third order but can be continued up to the seventh order. Equation 2.8 has been converted to complex notation in which $w = \theta + i\theta$ and $\overline{w} = \theta - i\theta$, the expansion now includes the defocus C_1, spherical aberration C_3, $A_{1,2,3}$ the 2,3 and 4-fold astigmatism, B_2 the 2-fold coma and S_3 the 3rd order star aberration. The CTF is expanded to the third order, as that is the degree of correction acquired using the

CEOS Corrector and the Zemlin-tableau method.[112-113] Aberrations are identified by tilting the beam off its optical axis and measuring the change in diffractogram, derived from a fast Fourier transform of an amorphous region, they can then be corrected for via the software.

In Warwick, two TEMS were used, firstly a JEOL ARM 200F operating at 80 and 200 kV with a Schottky emitter. TEM and STEM analysis was undertaken, with probe and image CEOS correction and TEM data was recorded on an unshuttered Gatan Orius SC1000 CCD camera. Secondly a JEOL 2100 operating at 200 kV with a LaB_6 emitter with data recorded on an unshuttered Gatan Orius SC600 Camera.

2.3.5 Scanning Transmission Electron Microscopy

Scanning Transmission Electron Microscopy (STEM) in principle is the rastering of a focussed electron beam across a sample and the examination of the transmitted signal.[114] This is achieved through the manipulation of scan coils, which allow the probe to remain parallel to the optical axis as it is rastered. Again bright-field (BF) and-dark field (DF) signals can be collected. The BF signal is acquired by placing a BF detector directly below the sample to intercept direct-beam electrons, the BF detector typically has a collection angle of $\beta \approx 30$ mrad, Figure 2.7. The DF signal is generated from scattered electrons, this signal is collected using an annular dark-field (ADF) detector, surrounding the BF detector collecting scattered electrons at high angles, typically 30 - 200 mrad. An extension of the ADF detector is the high-angle annular dark-field (HAADF) detector, which detects high-angle scattered electrons predominantly scattered by the nuclei of the sample, typically 120 - 450mrads. At these angles the primary source of scattering is Rutherford scattering which creates an intensity that is Z^2 dependent.[115]

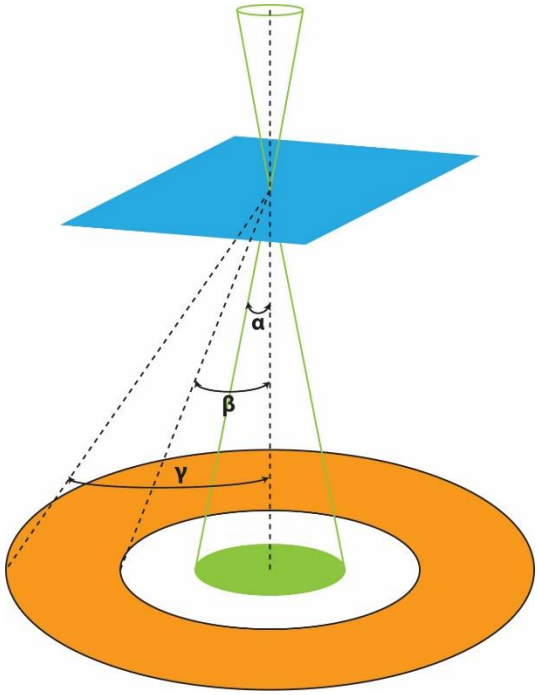

Figure 2.7: Example of the STEM beam interacting with a sample and scattering into the detectors. The collection angle of the BF detector (green region), α, ≈ 30 mrad, the DF detector (white region), β, = 30 – 200 mrad and the HAADF detector (orange region), γ, = 120 450 mrad.

2.4 Advanced Techniques and Characterisation

2.4.1 Energy Dispersive X-ray Spectroscopy

Interactions between the incident electron beam and the sample can lead to the emission of characteristic X-rays. These X-rays are produced when the incident electron beam inelastically interacts with the inner electron shell of the sample, ejecting electrons with and leaving an electron vacancy. This vacancy is then filled by an electron from a higher energy level, releasing a photon of energy, to drop and fill this vacancy. The X-rays can be detected and will have a characteristic energy equal to the difference in the two energy states of the higher and lower electron shells, which are characteristic of the element the X-ray was released from. An example of this process can be seen in Figure 2.8.

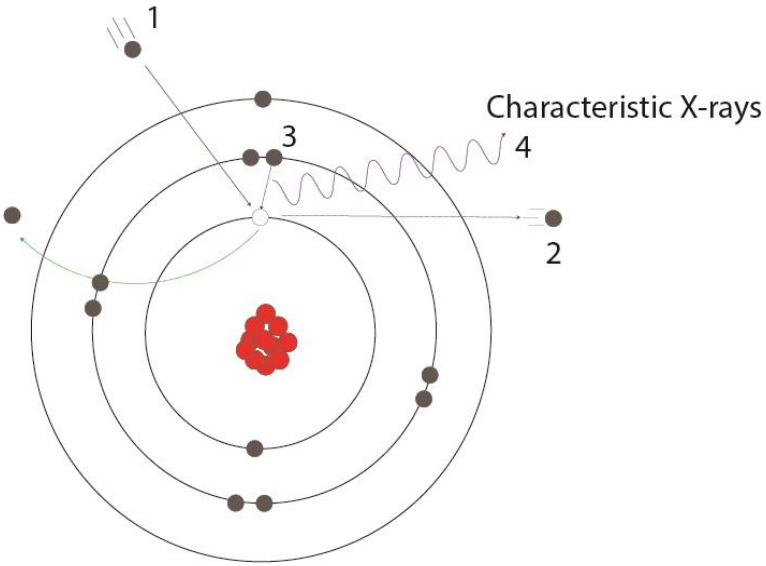

Figure 2.8: The interaction between an incident electron with the electron shell (1) ionizing the element and ejecting an electron (2). A higher energy electron drops down to fill the hole created by the lower energy electron (3), this change in energy is released in the form of a characteristic X-ray (4).

The X-rays are detected by an Energy-Dispersive Spectrometer consisting of a Si-drift detector, processing electronics and a computational analysis/output. A Si-drift detector consists of a wafer of pure n-type silicon capped with concentric rings of p-type silicon. X-ray interactions ionise the silicon, generating characteristic electrons which are detected as an electrical charge. The signal is processed and the result of collecting these characteristic X-rays over a period of time is a count vs energy spectrum, Figure 2.9. Once analysed this determines what elements are present within a sample, with the overall process known as EDX. Given greater analysis, now automated with modern software, the ratio of elements and a quantitative result of the samples composition can be obtained.

For SEM and TEM, the spectrum rendered originates from the region illuminated by the electron beam, with both systems often focusing the beam down to a spot to get an EDX spectrum from a desired region. In a SEM, the interaction volume is high, so as the electron beam penetrates into the sample it is more likely that the spectrum will be dominated by characteristic X-rays from a depth of $\approx 10\ \mu m$, therefore it is not a surface sensitive technique.

In a TEM as samples are electron transparent thickness effects become less of an issue with typical samples being ≤ 100 nm thick.

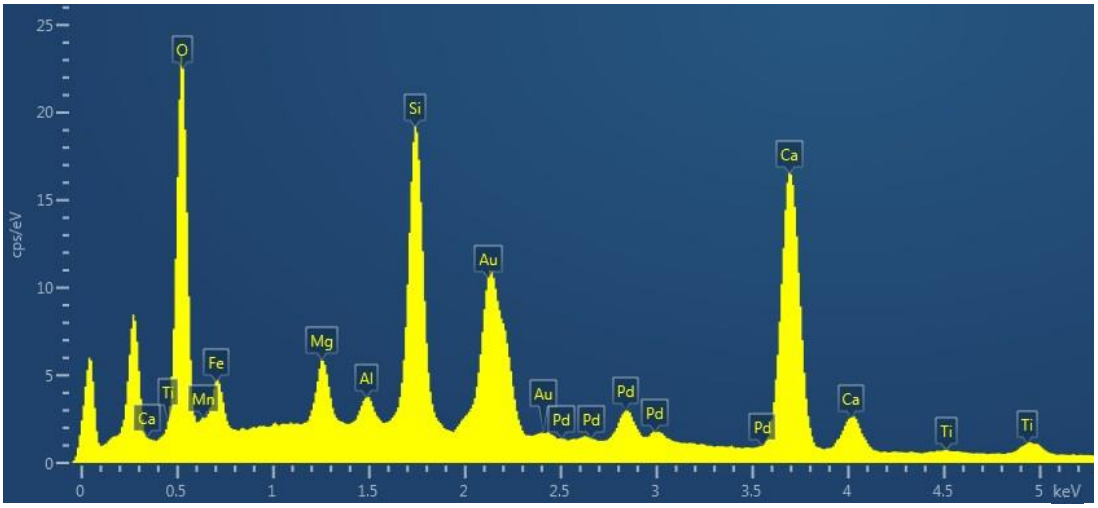

Figure 2.9: Example of a basic EDX spectrum for a complex SiO material. Ag and Pd peaks are observed from the conductive coating. A good example of signal convolution is observed at 0.5keV where Ti, O and Mn are identified within the same region.

In STEM and SEMs, as the beam is focused to a probe and rastered across the sample, an EDX spectrum can be obtained from each individual pixel during the scan. Therefore, by scanning for a prolonged period of time and summing the spectrum at each individual pixel, STEM can offer a range of different acquisitions that are not available in TEM. The three different acquisition types are point acquire, linescan and mapping. Point acquire is very similar to the standard acquisition technique seen in TEM, an initial image is captured by the EDX software and then the STEM probe is moved to designated regions of interest linking the spectrum and location with a greater degree of accuracy. For linescans, once an image is acquired by the software, the probe is scanned across a designated line collecting a spectrum at designated intervals. Mapping acquires an image and then a spectrum at every pixel within a designated 2D region. This technique is an example of spectrum imaging, in which a 3D data cube is generated with each (x,y) coordinate in an image having an associated EDX spectrum. Examples of the different STEM EDX acquisition modes are shown in Figure 2.10.

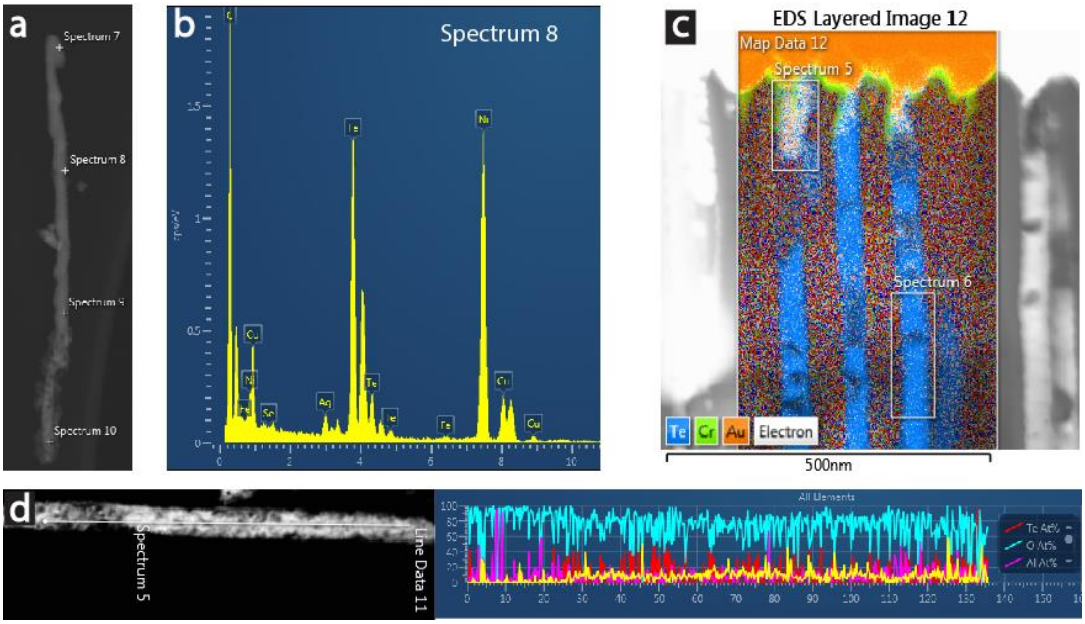

Figure 2.10: Examples of STEM EDX acquisition techniques: a) Point and acquire were individual regions are probed to generate EDX spectrums as shown in b). c) Spectral imaging of a sample where an EDX spectrum is acquired at every pixel in an image. This allows for the generation of intensity maps for individual elements which when colourised and superimposed provide a detailed image of the sample. d) EDX linescan along a TeO nanowire. Here an EDX signal is acquired for each pixel along a line, especially advantageous when looking at variations in elemental quantities across a sample.

EDX does have some disadvantages, during acquisition the orientation of the sample is extremely important to ensure that a high number of counts are acquired and that background signals are minimised. Background elements are often detected and can affect compositional analysis if not accounted for correctly. Light elements, $Z \leq 4$, cannot be detected by EDX and false elemental identification and quantification can arise due to shell energy overlap within complex samples. However, the advantages of EDX by far outweigh the disadvantages with quick acquisition times, easy analysis, a range of different acquisition types.

2.4.2 Electron Energy Loss Spectroscopy

A technique complimentary to EDX, electron energy loss spectroscopy (EELS) is the analysis of inelastically scattered electrons that have interacted with the sample ionising it through the excitation of an electron and subsequent X-ray emission. EELS is the result of a

primary interaction as the electrons analysed are the original electrons from the electron source, and not a byproduct of an interaction. Because of this primary interaction, the electrons may have lost no energy, known as “zero loss electrons”, or, being inelastically scattered, they will have very little deflection from the incident electron beam.

Detection occurs post specimen after the electron beam is rotated 90° by a magnetic prism, with inelastic electrons being deflected more than zero loss electrons, and focussed onto a CCD to be computed into a linear spectrum. The spectrum generated is counts vs energy loss (eV), it is separated into two approximate regions and has several characteristic features. Highlighted in Figure 2.11, the spectrum is split into the low-loss and high-loss regions at ≈50eV, with the low-loss region generating electronic information from the sample and the high-loss primarily elemental. This post column spectrometer is known as the Gatan imaging filter GIF. [116]

The low-loss region contains the zero-loss and plasmon peak, as the zero-loss primarily contains elastically forward scattered electrons, and electrons that have suffered small energy losses, which is the strongest feature on the spectrum. Often containing 10^6 – 10^{10} counts compared to < 100 for an elemental edge, this peak forces the spectrum into a logarithmic scale. The plasmon peak can be used to “chemically fingerprint” a sample, analysing the general shape and position of the peak, any shifts or variations are generated by different compounds of a known structure. The dielectric constant and band gap can also be interpreted from the low-loss region.[117-118]

The high-loss region consists of elemental edges, generated from inelastic scattered electrons superimposed onto a decreasing background. As previously shown in Figure 2.4, when ionisation occurs, an electron drops from an outer shell to fill the hole, the shells discussed are the K, L and M shells, each with different element dependent binding energies. The edge structures for the shells and elements can vary greatly, some produce a simple

hump in the spectrum, whilst others produce a fine structure with combinations of spikes and humps, as shown in Figure 2.11 for Te and C. Again, this can be used as another way to fingerprint an element. Like EDX, when used in combination with STEM, this technique can be used for spectrum imaging, creating an EELS spectrum at each individual pixel to produce maps, linescans or standard spectra.

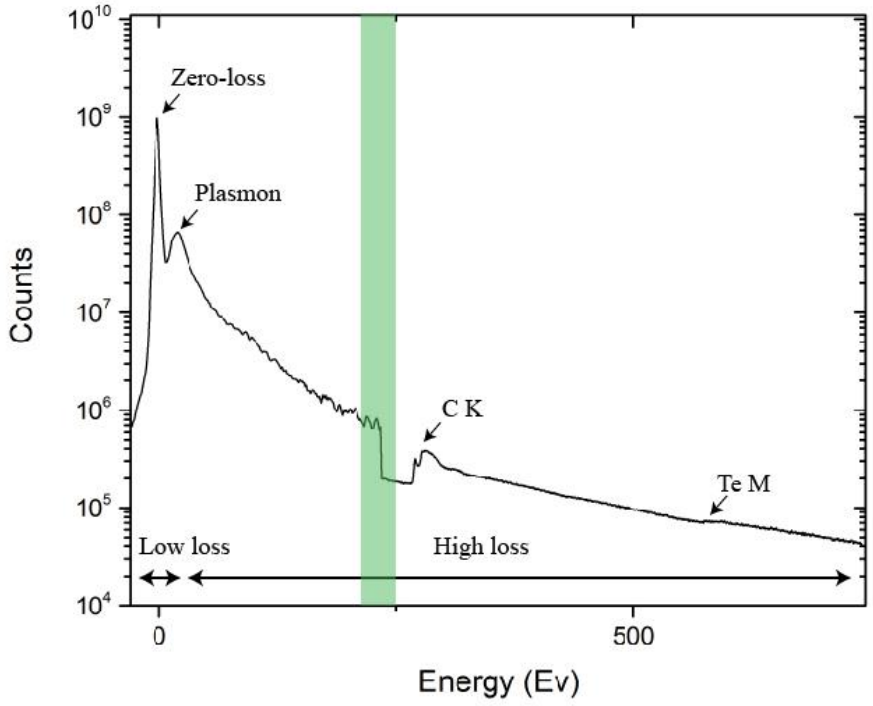

Figure 2.11: A combined EELS spectra showing the low-loss and high-loss regions. The zero-loss and plasmon peaks are observed with extremely high count rates compared to the C and Te edges. Different examples of edge structure are observed with the fine structure clearly seen for the C and only a hump generated by the Te signal. The highlighted region indicates where two spectra have been spliced together creating a change in background count levels.

2.4.3 Electron Diffraction

Electron diffraction arises from the interference pattern of the electron beam as it is scattered through the crystal lattice of the specimen. In standard TEM imaging, the diffraction pattern is generated in the back focal plane, with the TEM image in the image plane, however by adjusting the lenses the diffraction pattern can be generated in the image plane, previously

illustrated by Figure 2.6 b. As electron diffraction in generated by the scattering through a crystalline lattice it can reveal crucial crystallographic information about a sample.

An amorphous sample will produce a diffraction pattern of diffuse rings correlating to the average spacing of the atoms. Crystalline samples will form a more complex diffraction pattern due to scattering of the incident beam through a repeating crystal lattice. Bragg's law for constructive interference from a crystal lattice, described below, states that

$$n\lambda = 2dsin\theta \qquad (2.9)$$

where d is the lattice spacing of the crystal, n is an integer, λ the electron wavelength and angle of incidence θ, illustrated in Figure 2.12, that, as the incident beam is scattered, it will undergo constructive or destructive interference.[119-120]

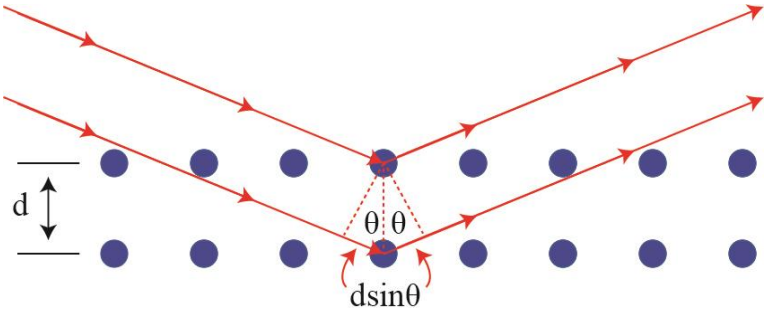

Figure 2.12: The scattering of incident electrons by a crystalline sample. The lower beam is observed to traverse an extra length of *2dsinθ*. Constructive interference occurs when the wavelength is equal to n integer multiple of the wavelength of the electron beam.

The effect of Bragg's law on the diffraction pattern, through constructive and destructive interference, is the generation of bright spots on a dark background that correlate to the crystal structure. From this, lattice parameters, crystal symmetry, crystal type, mono or polycrystallinity and growth orientation can all be determined.

2.4.4 Radial Distribution Function

Amorphous crystals and liquids lack a repeating crystal structure, but that does not mean they are completely disordered. The atoms will self-order to minimise energy, producing

repeated average spacings between atoms, this is apparent from the rings generated in the electron diffraction patterns. This ordering can be determined by analysing the radial distribution function (RDF) of the diffraction pattern. RDF describes, for a system of particles, how the density varies as a function of distance from a reference particle.[121]

In its basic form, RDF is a measure of probability, to find a particle at a distance *r*, relative to a reference particle. The formula to determine the average number of atoms in a spherical shell of thickness *dr* at a distance *r* from a reference particle is

$$\int_{shell} n_0 g(r) dr = 4\pi r^2 n_0 g(r) dr \qquad (2.10)$$

where $n_0 = N/V$ and is the average density of N atoms in a volume V, $g(r)$ is the correlation coefficient accounting for the potential energy of the system and $4\pi r^2 g(r)$ is the RDF.[122]

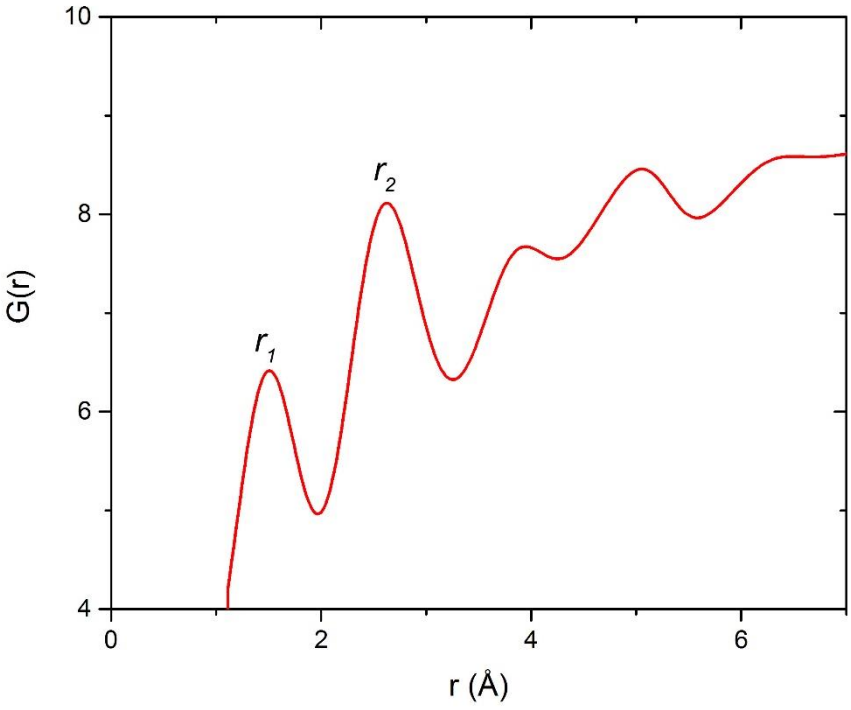

Figure 2.13: Radial distribution function from an amorphous carbon film. The first and second nearest neighbour distances are highlighted by r_1 and r_2 respectively.

An RDF generally takes the form of a histogram, Figure 2.13, with the first peak, r_1, being the nearest -neighbour distance and the second peak, r_2, the second nearest neighbour

distance. The average bond angle within the sample can be calculated from the relationship highlighted by equation 2.11

$$\frac{\alpha}{2} = sin^{-1}\left(\frac{r_2}{2r_1}\right) \qquad (2.11)$$

All RDF analysis is undertaken using D. Mitchell and T. Petersens *RDFTools* plugin.[123] Where, for an imputted diffraction pattern, the RDF is generated computationally from equation 2.10.

2.4.5 *Ab Initio* Random Structure Search

Random structures are generated by forming a "random" unit cell with three cell-vector lengths and three cell angles randomly generated from the chosen boundary conditions, typically 0.5 to 1.5 (arbitrary units) and 40 to 140 º. The "random" unit cell is then scaled to reproduce the desired volume, again this is randomly chosen as a value between 0.5 and 1.5 of the chosen volume. The atoms are randomly distributed throughout the cell before each structure is relaxed, using *ab initio* density-functional theory (DFT), into the nearest local minimum surface in their potential energy surface. The structures can then be ranked according to their formation energy per atom, to define the lowest energy and therefore most energetically stable system.

The main challenge faced when simulating encapsulated structures is the amount of computing time required per simulation. As each simulation requires a full SWNT and encapsulated nanowire, simulated structures will easily contain more than 100 atoms. This makes simulations of filled SWNTs infeasible, as the number of simulations required to account for different SWNT diameters, combined with the nanowire bond angles and distances is too great and will incur large expenses and a high amount of computing time. However, observations suggest that, with filled SWNTs, the encapsulated nanowire structure is a result of the confinement and not an interaction with the carbon nanotube, with reports

of the interior of a SWNT being more inert to atomic species.[124] Therefore, the SWNT does not need to be generated as part of the structure search, and is replaced by a confining potential as a representation of the SWNT diameter.

Simulations are undertaken using CASTEP, with the confining potential generated using a Gaussian cylinder plot.[125] The generated structures are ranked by formation energy per atom. This identifies the potentially optimum structures which are then fully simulated within SWNTs to generate accurate simulations. Here an example of the formation energy for Te encapsulated within a SWNT, E_{Form}^{Te}, is defined as

$$E_{Form}^{Te} = \frac{1}{N_{Te}}[E_T - N_C \mu_C - N_{Te} \mu_{Te}] \qquad (2.12)$$

where E_T is the total energy of the full system, N_C and N_{Te} represent the number of C atoms in the SWNT and Te atoms encapsulated within it, and μ_C and μ_{Te} are the chemical potentials associated with the C in the SWNT and an atom in bulk Te. The density of states (DOS) was calculated using the OptaDOS code, in which the spectra are generated from the eigenenergies through integration over the Brillouin zone.[126]

Characterisation of Supercritical Fluid Electrodeposited Samples

3.1 Introduction

Electrodeposition is an attractive method for nanoscale deposition for multiple reasons. It is a bottom-up technique that allows for selective filling of 3D nanostructures and nano-patterned substrates. Direct control of the driving force is provided through the applied potential, allowing for in deposition measurements of the electrical properties and direct feedback on the deposition process. However, some drawbacks of electrodeposition into porous templates arise as the pore diameters get smaller. Problems of slow mass transport rates in/out of pores and pore wetting from surface tension become significant in sub 20 nm pores.[20] The use of a supercritical fluid can overcome the problems faced by standard aqueous deposition into porous media, as described in section 1.2.2, through the application of a supercritical fluids tuneability. These include a low viscosity with fast rates of mass transport and an absence of surface tension.

Electron microscopy is a key technique required to analyse samples at the sub-micron or nanometre scale.[127] From the electrochemical point of view, the main reference of successful deposition are the cyclic voltammetry measurements. This measures the current at the deposition electrode, allowing for examination of the electrochemistry. Under certain deposition conditions a colour change may also occur in the sample. Therefore, there is often no proof that the desired reaction has taken place.

In this Chapter I will explain why electron microscopy is a key experimental technique through several examples of different systems. The electrodeposition of a planar

Ge thin film explores the use of electron microscopy to complement alternative analysis methods. This leads to the deposition of nanowires into porous media, exploring the effects of pore diameter on the Ge nanowires. The composition of two crystallographically complex binary and ternary systems is explored using XRD and electron diffraction. Finally, in an attempt to decrease nanowire diameters, a custom hierarchical template was deposited into in order to form sub 10 nm nanowires.

3.2 Germanium Deposition

The first case of electrodeposition from a supercritical fluid examines planar SCFED of Ge as a thin film onto a TiN substrate. As a case study of SCFED grown samples, planar thin film deposition is the initial step for testing the deposition of new materials. By removing the confinements of porous templates, analysis of potential deposition conditions is easily achieved. Direct comparisons between the planar films and encapsulated nanowires allow for discussion over the effects of encapsulation size.

3.2.1 Germanium Thin Films

Films of Ge were electrodeposited from $[GeI_3]^-$ onto TiN electrodes from [EMIM][BF_4]/[EMIM][GeI_3] and [N^nBu_4][BF_4]/ [N^nBu_4][GeI_3] in supercritical CH_2F_2 (deposition by Charlie Cummings at the University of Southampton). TiN was chosen as an electrode as, unlike gold, it does not form alloys with Ge.[128-129] Deposition was undertaken for 4000 s at -1.05 V versus Ag|LaF_3 in scCH_2F_2 at 19.1 MPa and 358 K from a) 16 mM [EMIM][GeI_3] with 60 mM [EMIM][BF_4] and b) 16 mm [N^nBu_4][GeI_3] with 60 mM [N^nBu_4][BF_4].

A deposition rate of 3.22 C cm^{-2} h^{-1} and 4.32 C cm^{-2} h^{-1} was calculated through integration of the current in the chronoamperograms, Figure 3.1 A, for the $[N^nBu_4]^+$ and $[EMIM]^+$ electrolytes respectively. Assuming 100% faradaic efficiency this corresponds to a plating rate of 2.27 and 3.04 µm h^{-1} which is comparable to reported deposition rates for ionic liquids at room temperature, but lower than reported for elevated temperatures.[130-131]

This may be explained by the experimental set up, in which an undivided cell is used during the electrodeposition process, therefore allowing mixing and reactions from the counter electrode and the working electrode.

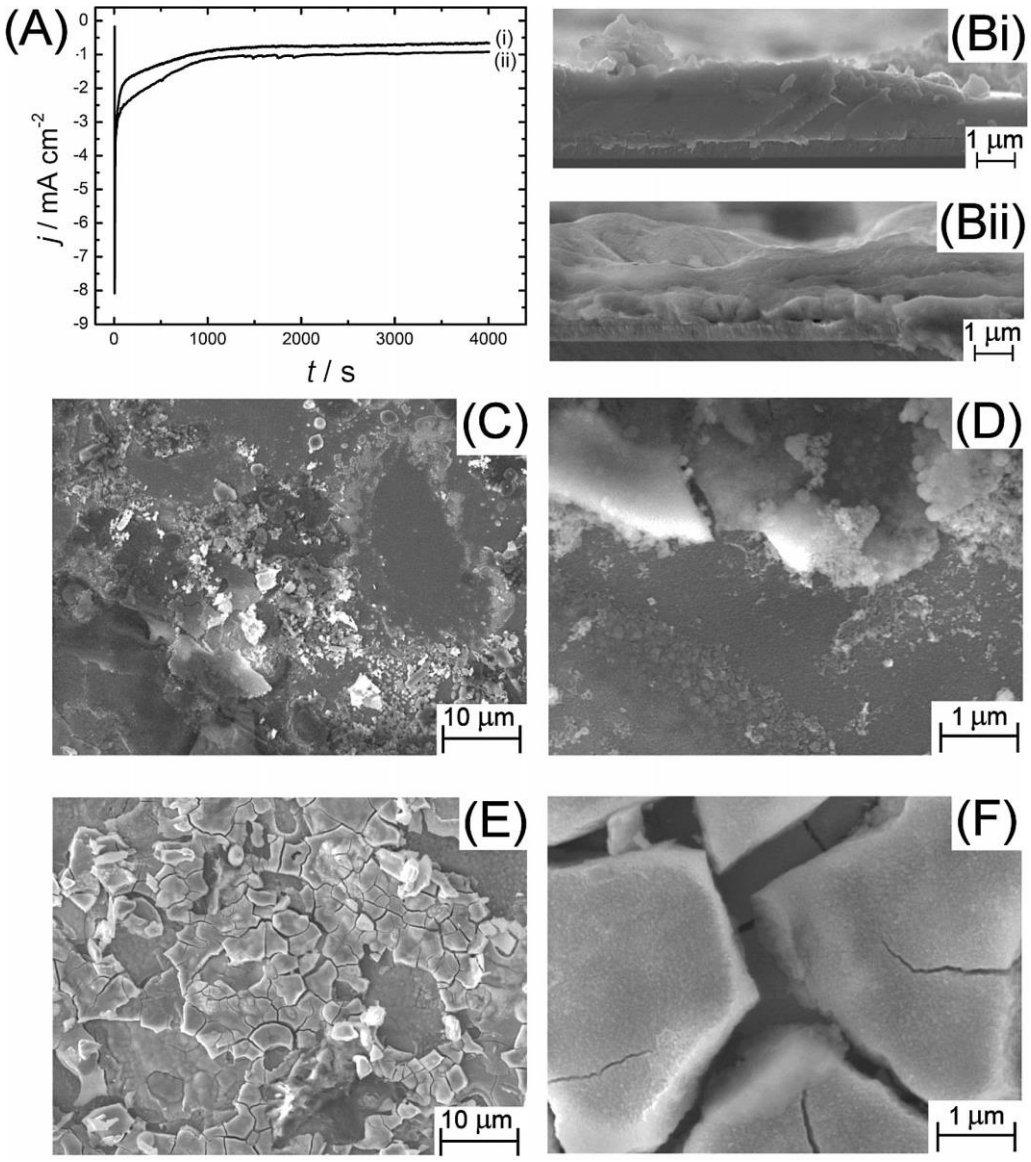

Figure 3.1: A) Chronoamperogram recorded for Ge deposition from electrolyte i) $[EMIM]^+$ and ii) $[N^nBu_4]^+$. B) SEM cross section of as-deposited Ge films from i) $[EMIM]^+$ and ii) $[N^nBu_4]^+$ systems. C) Low- and D) High – magnification SEM images of $[EMIM]^+$ system highlighting the low coverage and Ge grain size. E) Low- and F) High – magnification SEM images of $[N^nBu_4]^+$ system highlighting larger Ge grain size.

The as-deposited films were initially analysed with SEM followed by XRD and Raman then finally by TEM. Cross-sectional imaging of both samples reveals similar film

thicknesses of 1 – 2 µm for both the $[EMIM]^+$ and $[N^nBu_4]^+$ systems, Figures 3.1 B i and ii respectively. The effect of the different cations can clearly be seen when examining the surface of the films. The $[EMIM]^+$ system has considerably less coverage with regions of bare TiN visible across the sample, Figure 3.1 C and D. This may be a result of delamination during depressurisation or poor surface adhesion. The Ge that is deposited forms in grains of 0.1 – 1 µm. The $[N^nBu_4]^+$ system has considerably better coverage with much larger grains of 2 – 5 µm, Figure 3.1 E and F. Again delamination is observed but this cracking delamination is similar to that reported by Klavetter for Ge electrodeposition.[132] EDX analysis highlighted a number of impurities within the sample, including O, I and F. O is expected as Ge is known to readily oxidise in atmosphere. It is believed that the I and F arise from the depressurisation of the supercritical fluid, leaving precipitates on the electrode surface. It was found that washing the sample in dichloromethane decreased the concentration of contaminates.

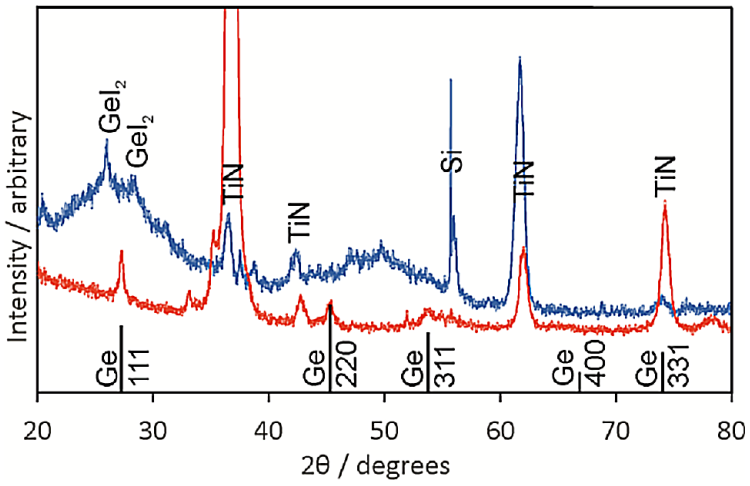

Figure 3.2: XRD for as-deposited Ge film (blue) and the same film post annealing at 700 º C under argon (red). (Acquired by A. Hector, University of Southampton)

Grazing incidence XRD of the as-deposited films in Figure 3.2 show two broad features around 27º and 50º with sharp reflection arising from the substrate and electrolyte components. The broad features may be the result of amorphous Ge attributed to the 111, 220 and 311 Ge lattice spacings. As previously stated O is present in the sample suggesting

that the crystalline peaks are being disrupted by amorphous GeO. To remove the oxide, the samples were thermally annealed under Argon at 700 º C, this resulted in crystalline Ge in close proximity to the position of the broad features, Figure 3.2.[133]

Further characterisation was undertaken using Raman spectroscopy, as it is sensitive to both amorphous and crystalline materials. The as-deposited films, Figure 3.3 A and B ii), show amorphous spectra characterised by a broad hump for both systems. The post annealed films, Figure 3.3 A and B i), show a clear peak attributed to crystalline germanium however the broadness of the peak suggests that there is still a considerable amorphous signature. We have deemed this material as protocrystalline in nature, containing quantities of both amorphous and crystalline Ge.

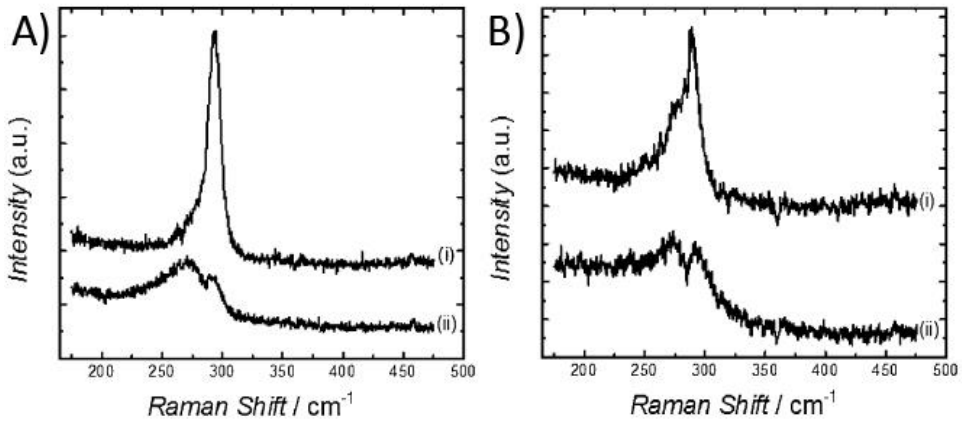

Figure 3.3: A) Raman spectrum for i) post annealing and ii) as deposited $[EMIM]^+$ system. B) Raman spectrum for i) post annealing and ii) as deposited $[N^nBu_4]^+$ system. (Acquired by J. Spencer, University of Southampton)

In further efforts to understand the nature of the protocrystalline Ge films, a sample of the post annealed $[EMIM]^+$ system was imaged inside the TEM. The sample was prepared by scraping the surface onto a lacey carbon film to create electron transparent flakes for investigation. Selected area electron diffraction of the Ge flakes highlights the protocrystallinity suggested from the XRD and Raman spectra, Figure 3.4 B. Both diffuse rings, consistent with amorphous materials, and bright spots, representing the repeating

crystalline lattice, are easily observed in the selected area electron diffraction pattern (SADP). The radial intensity distribution plot, Figure 3.4 C, conveys this diffraction result in which the broad humps arise from the amorphous material and sharp peaks from individual crystallites.

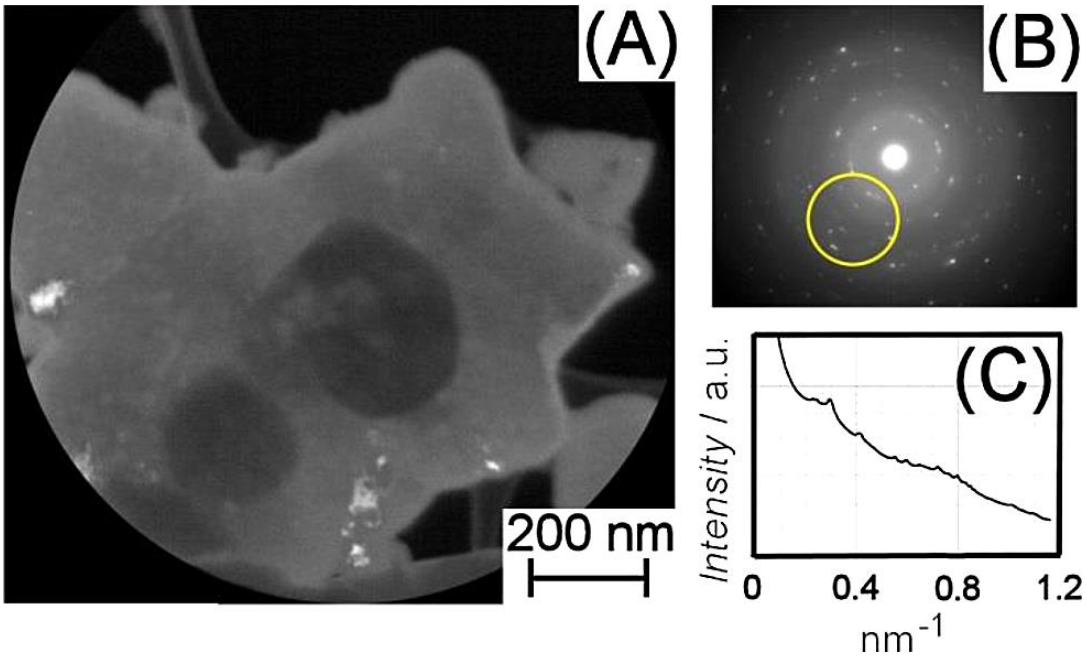

Figure 3.4: A) Dark field image of Ge flake highlighting Ge crystallites embedded within amorphous Ge. B) Selected area diffraction pattern from flake including the objective aperture used to generate the dark field image. C) Radial intensity distribution of selected area diffraction pattern indicating crystallites (sharp peaks) in an amorphous membrane (broad peaks).

Bright field images show the flakes to have uniform contrast however dark-field images, generate contrast from the diffracting crystalline Ge. The embedded crystallites have a range of diameters between 5 – 30 nm. They appear to be embedded within an amorphous Ge matrix, as shown in Figure 3.4 A. Quantification of the crystallites proved impossible due to the crystallites amorphising under the electron beam.

This is the first reported case of successful electrodeposition of Ge from a supercritical fluid, in which TEM characterisation allowed for the visualisation and confirmation of a system theorised from two different measurements. The Ge flakes were

shown to be highly beam sensitive undergoing in situ amorphisation as a result of electron beam irradiation.

3.2.2 Germanium Nanowires

More challenging depositions into both 35 and 13 nm porous alumina templates were attempted. Both systems were electrodeposited from [EMIM][BF_4]/[EMIM][GeI_3] in supercritical CH_2F_2 at 151 ºC and 450 bar with a ratio of 5 mM [EMIM][GeI_3] to 60 mM [EMIM][BF_4]. After deposition a lift-out FIB section was prepared and some of the template was etched to release the nanowires onto lacey carbon.

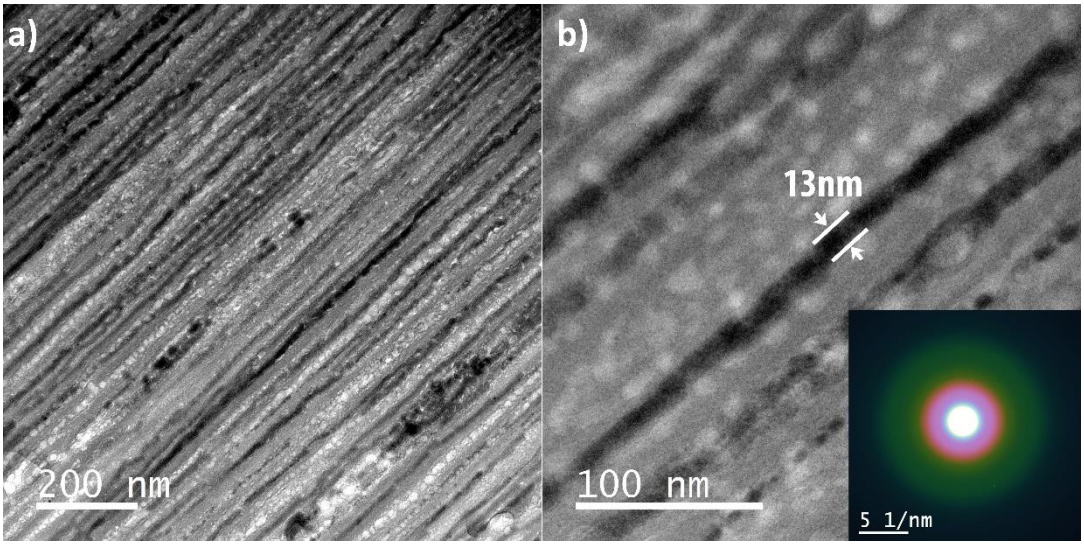

Figure 3.5: a) TEM image of a FIB prepared encapsulated Ge nanowires template indicating a high filling rate across the visible region. b) A single isolated 13 nm nanowire inset with its associated amorphous SADP.

The FIB section in Figure 3.5 shows a high amount of filled nanopores within the analysed area. HRTEM and SADP showed the nanowires to, once again, be amorphous with no evidence of crystallinity. The effect of the electron beam interacting with the sample beam can be seen in both the lower and higher magnification images as a “bubbling” effect. At higher magnifications this electron beam interaction generates crystallites within the alumina. This introduces polycrystalline diffraction spots into the amorphous SADP,

however, these crystallites are embedded within the Al and not the Ge as reported by Stratton.[134]

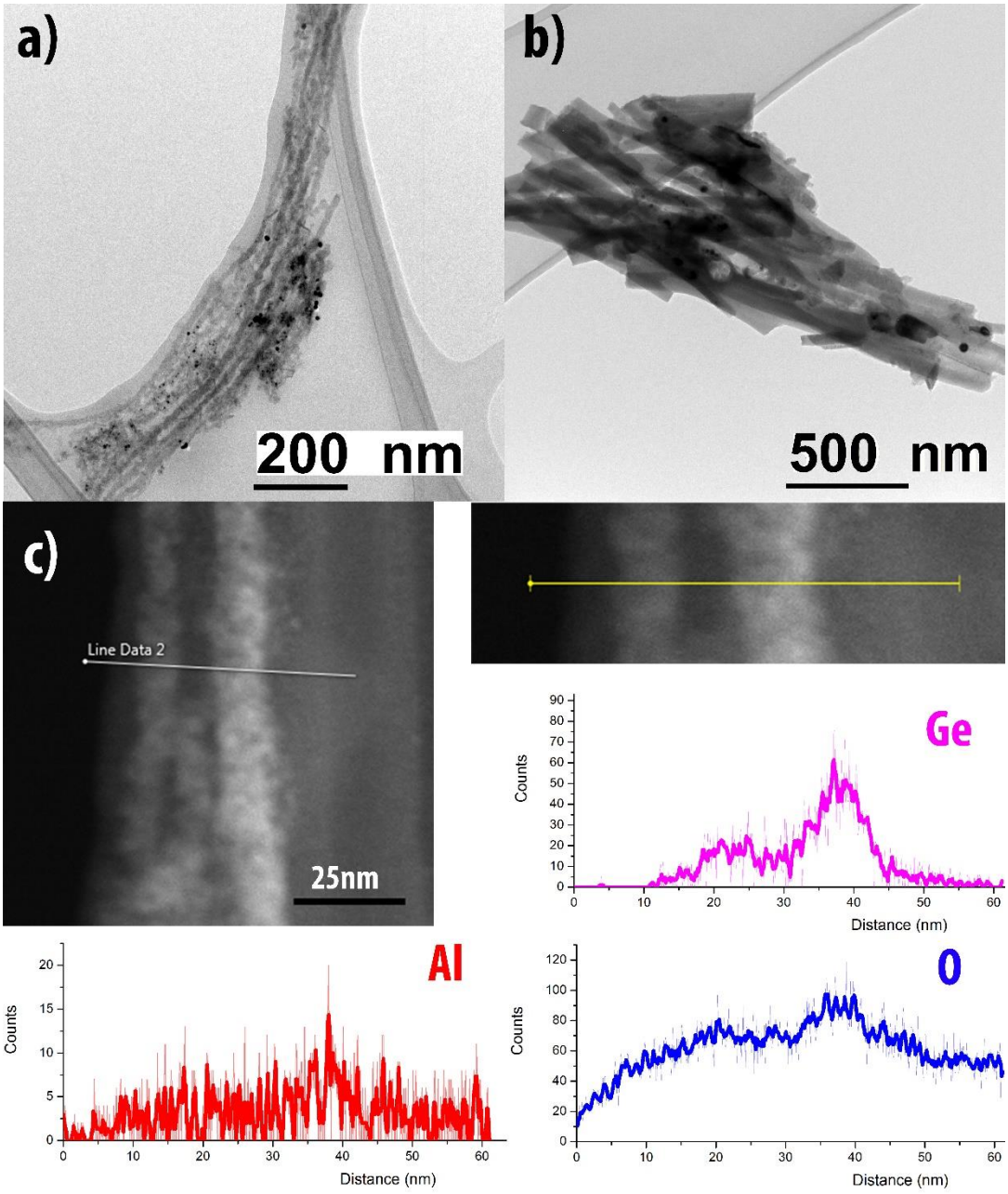

Figure 3.6: a - b) TEM images of the 35 and 13 nm released nanowires respectively, the build-up of contamination is a result of the template removal process. c) EDX linescans of the released 13 nm Ge nanowires. Smoothing (bold) has been applied to reduce the noisy data (trace). This arises from the small interaction volume available from 13 nm of sample.

Pore diameter appears to have no effect on the crystallinity of the nanowire as released nanowires from both the 35 and 13 nm diameter templates generated amorphous

nanowires. Visually, the 35 nm nanowires look more stable, as seen in Figure 3.6 a, but this is believed to be an effect of the template removal process as the nanowires from both systems are amorphous with similar elemental compositions. EDX linescans of the Ge nanowires suggest that the nanowires are not GeO. The observed O signal correlates with the Al signal, as expected for the alumina template. The percentage measurement of O is higher than expected due to the convolution of O and C energy peaks within the spectra.

Expanding on the planar deposition, this proves that Ge can be successfully electrodeposited from a supercritical fluid into a porous template. No correlation between nanowire size and crystallinity is observed, with all forms of Ge deposited being predominantly amorphous.

3.3 The Formation of Copper Telluride and Copper Tellurium Sulphide Nanowires

3.3.1 Copper Telluride

More complicated systems can also be generated using SCFED, with successful attempts at heterojunctions and binary nanowires, currently unpublished. One unique system is the Copper Telluride system and more importantly Copper Tellurium Sulphide. In this system Te nanowires were electrodeposited into 13 nm porous templates from a solution of $[N^nBu_4]_2[TeCl_6]$ in supercritical difluoromethane (scR32) at a temperature of 86 ºC and 18.1 MPa (deposition by David Cook at the University of Southampton). Notably, no Cu is in the solvent or solute as it entered the system as a by-product from the solvent dissolving a brass screw. It is assumed that, at the elevated temperature and pressure, the screw was dissolved into the solvent at an accelerated rate to create a CuTe binary solute of unknown composition prior to the electrodeposition process.

Imaging of the nanowires by SEM after template etching, Figure 3.7, showed a high filling rate with nanowire lengths between 20 and 30 µm. EDX of the nanowires shows a

strong Cu signal as well as the dominant Te signal with a small signal from remnants of the alumina template. There is no apparent remnant Zn signal from the screw (which would appear at 8.6 and 1.0 keV), Figure 3.7 b. This reinforces the hypothesis that a solute is created prior to electrodeposition. The phase of copper telluride can be challenging to identify due to its range of different compositions both stoichiometric (CuTe, $CuTe_2$, Cu_3Te_4, Cu_7Te_5) and non-stoichiometric i.e. Weissite ($Cu_{2-x}Te$).[135-138]

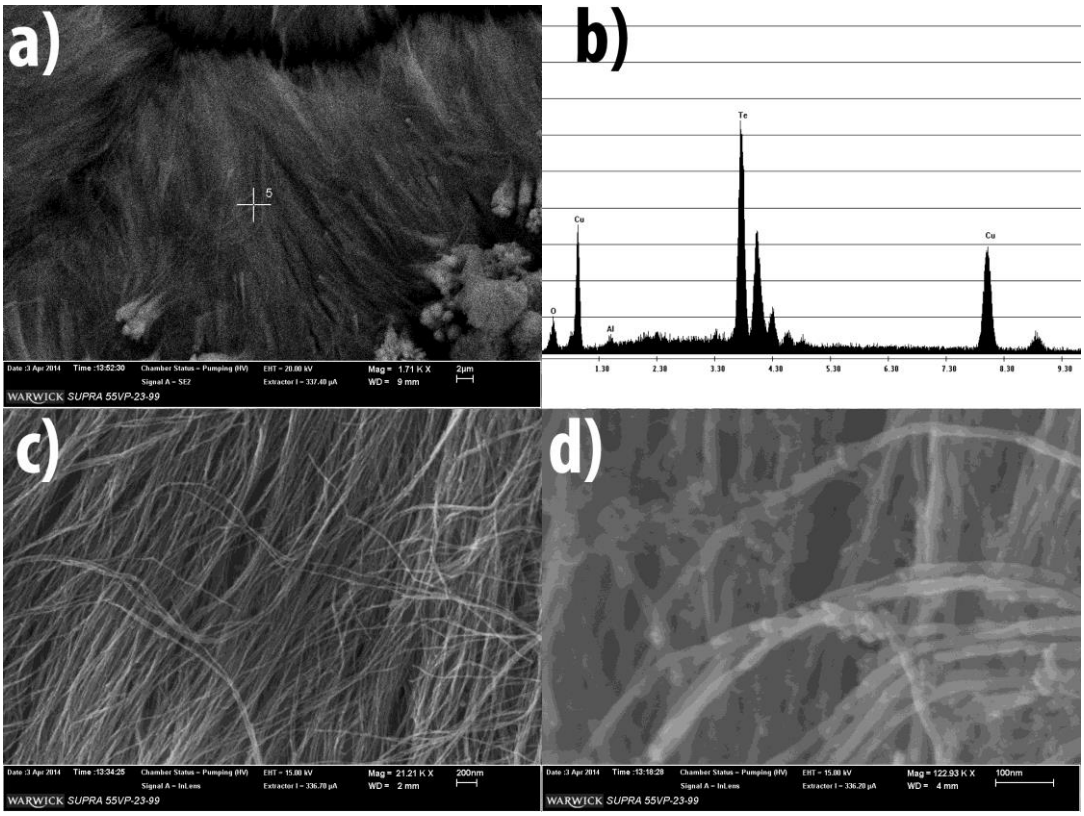

Figure 3.7: a) SEM image including beam marker for beam position during associated EDX acquisition in b. b) EDX spectrum from template released nanowires showing the nanowire composition as predominantly CuTe with some remnant alumina signal. c) Spaghetti web of continuous uniform released nanowires. d) High-magnification image of the branch like nanowires, a comparable uniform diameter can be observed throughout the image.

SADP of the nanowires once released onto a lacey carbon grid and imaged by TEM, Figure 3.8 a, indicates that the nanowires are polycrystalline. The polycrystalline SADP was analysed and plotted as a reduced density function plot (RDF). This is a circumferential integration of the SADP over 360 degrees, followed by the subtraction of the radially

decreasing background. This leaves a plot of reduced intensity with peaks that correspond to the inter-atomic orientation spacing which is directly comparable to XRD simulations. Comparisons between the RDF and simulated XRD intensities, shown in Figures 3.8, highlight a large degree of mismatch for most structures. However, the p4/nmm CuTe structure shows good correlation between the intensities and peak positions, Figure 3.9 e, confirming this space group.

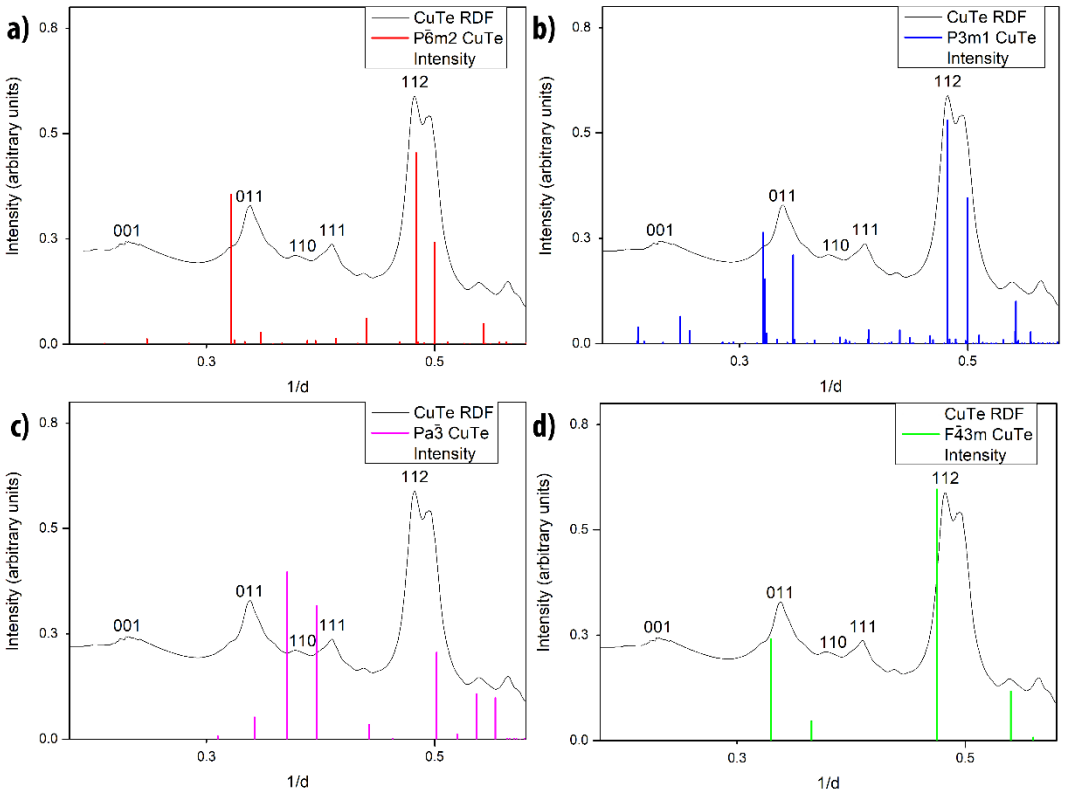

Figure 3.8: Comparisons between the experimental CuTe RDF and generated XRD profiles for known CuTe orientations. There is notable correlation between each individual structure, however, there is no complete correlation.

The structure identification as the P4/nmm tetragonal space group suggests a rickardite structure and therefore a $Cu_{3-x}Te_2$ or Cu_7Te_5 composition.[139-140] This can be seen in the STEM image as alternating Te and Cu columns, generated from atomic number contrast within HAADF. A line profile of the atomic column contrast, extracted from the nanowire in Figure 3.9 c, clearly show the repeating Te/Cu/Te structure. The crystallographic axis is [-0.56,0.57,0.87], shown in Figure 3.9 d, which is an off-axis orientation of the [-

1,1,2] plane. This first example of a binary nanowire grown through SCFED, highlighting the potential of the technique to produce more complex systems. As a result of this initial deposition more complex systems are currently being studied including: BiTe, SbTe, CuTe and SnTe.

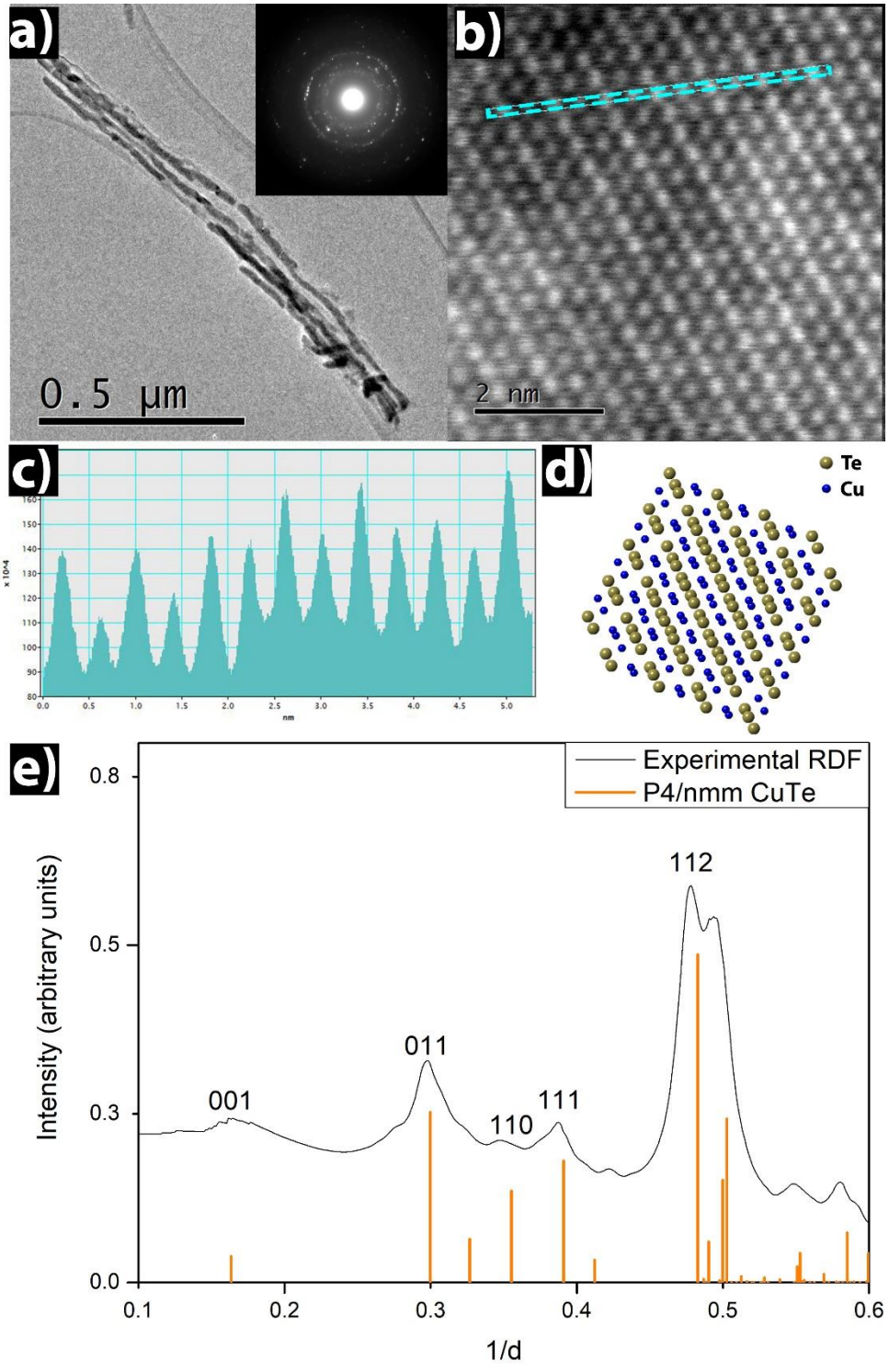

Figure 3.9: a) TEM image of naturally bundled CuTe nanowires post template removal, SADP for the bundle is inset suggesting polycrystalline nanowires. b) Annular dark field STEM image of the CuTe nanowires. c) Linescan of the atomic column contrast across the sample, area shown in c. d) Visualisation of the crystallographic orientation, the overlapping atoms generating smearing in the ADF image. e) RDF plot of the SADP is superimposed with kinematic intensities. A high degree of correlation is observed, with a mismatch between RDF and XRD arising from a zero offset error originating from the SADP.

3.3.2 Copper Tellurium Sulphide

A second unique phase was identified within the same sample, in regions with increased quantities of sulphur, a common Cu based contaminate, likely originating from within the original Cu source. A high-magnification STEM image is shown in Figure 3.9. The discovery of a Cu-Te-S phase was first reported by Makovickys, in 2000, as $Cu_{2.31}TeS_{0.32}$. Further work by Gillers suggested that the composition should actually be Cu_6Te_3S forming a $P2_13$ cubic α phase at room temperature and transforming into two different $P\bar{4}3n$ cubic β phases at elevated temperatures.[141-142]

All four phases are extremely similar with Giller's structures being an expansion of Mackovicky's work. When viewed along [001], all structures have a large octagonal structure defined by Te atoms, shared between adjacent octagons, and a central column of Te atoms, as observed in Figure 3.10. The spacing of Te atoms in the central column is twice that of those shared between octagons. Comparisons between the experimental image and the published theoretical models show clear agreement in position and intensity for these atom columns. The spaces between the Te atoms are filled by a network of Te and S atoms, and it is these which vary between the different models. Because of their similarities there is very little distinction between the four models making visual confirmation between the different models challenging. Nevertheless, it is clear from Figure 3.10 that the arrangement of Cu atoms in straight lines in the Mackovicky and Gillers 293 K alpha model are more consistent with the experimental image than the V-shaped arrangement of Cu atoms in the Gillers 473 and 673 K beta phases.

The HAADF images give Z number contrast matching the Cu and Te in the models to the images however as S is a light element it gives very low contrast in HAADF images. In order to investigate the structure more carefully, SADPs of the CuTeS were acquired and compared with simulations, as shown in Figure 3.11. Comparisons between the four

structures electron diffraction patterns undoubtedly establish the 293 K α Cu_6Te_3S phase as being most consistent with the diffraction pattern.

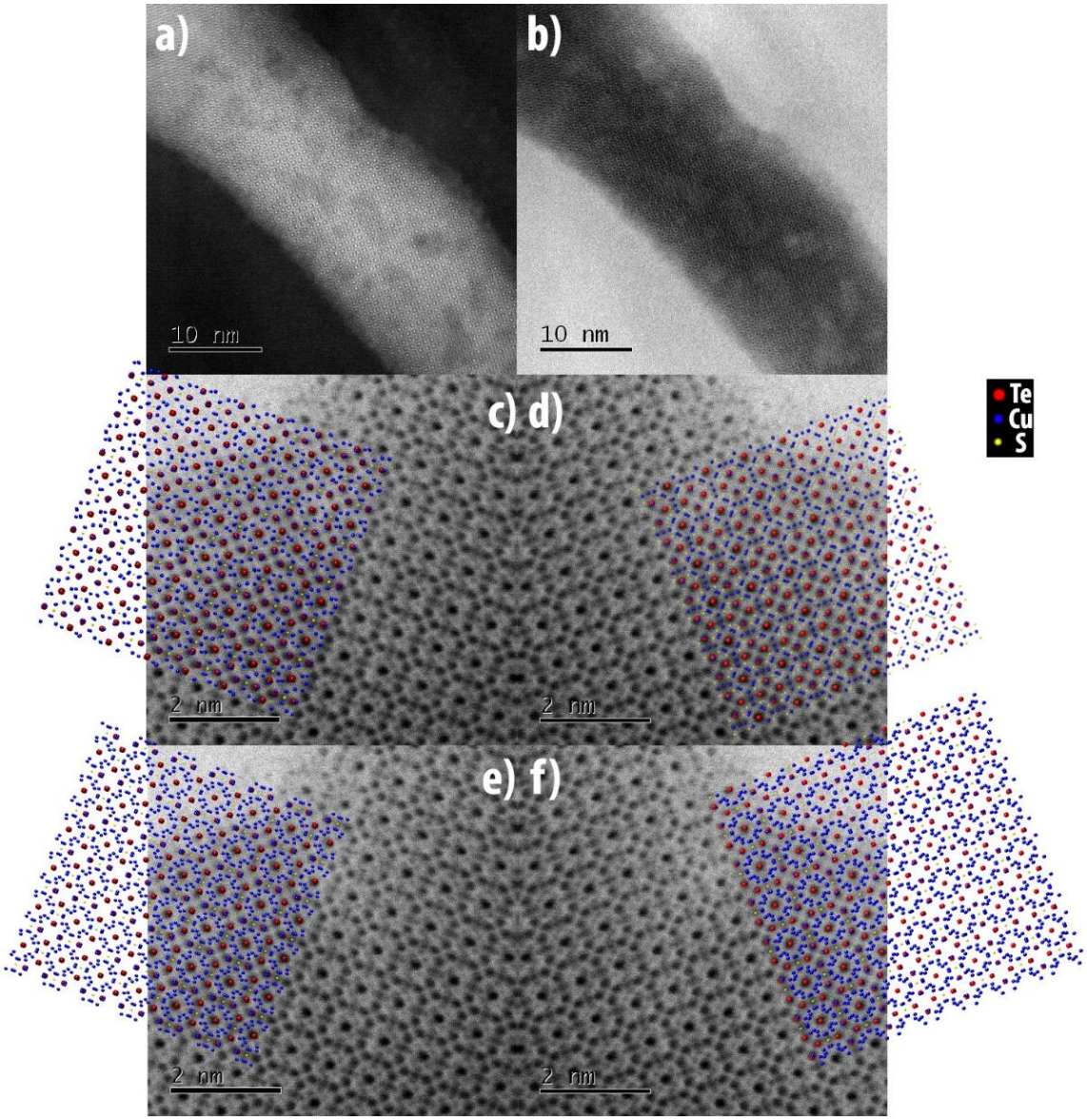

Figure 3.10: a-b) STEM HAADF and BF image respectively, showing the CuTeS superlattice structure formed in a 13 nm nanowire. c-f) The Cu_6Te_3S 293 K α phase (c), Mackovicky $Cu_{2.31}TeS_{0.32}$ structure(d), Cu_6Te_3S 473 K β phase and Cu_6Te_3S 673 K β phase all superimposition onto a BF image. The nanowire is mirrored in c and e to allow superimposition on the image.

This conclusion arises from the presence of additional superstructure diffraction spots that are only observed in both the experimental data and the α phase Cu_6Te_3S. The growth orientation of the nanowire could be any of the major axis as the [100], [010] and

[001] planes all produce the same reflections. With only two previously published articles on the CuTeS system, it is believed that this is the first recorded growth of a nanowire. It is also the first reported case of low temperature synthesis with the previous samples generated from high temperature quenching.

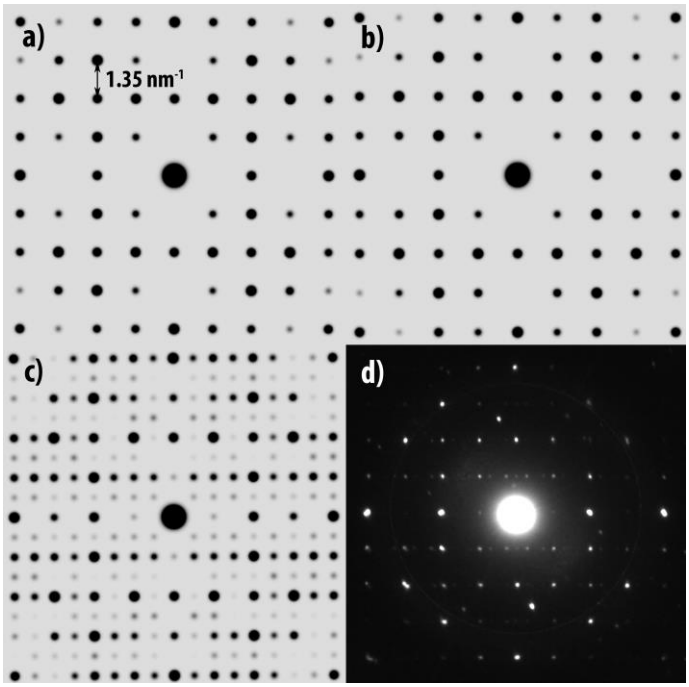

Figure 3.11: a) Simulated SADP of the $Cu_{2.31}TeS_{0.32}$ Mackovicky structure highlighting the 1.35 nm^{-1} spot spacing observed for all model phases and the experimental image. b) Simulated SADP of the 473 K β phase, which appears identical to both the 673 K β phase and the $Cu_{2.31}TeS_{0.32}$ structure. c) Simulated SADP of the 293 K α phase Cu_6Te_3S, with an additional array of weak superstructure spots. d) Experimental SADP from a CuTeS nanowire, the repeating 1.35 nm^{-1} spaced structure is observed as well as the superstructure spots, consistent with c).

3.4 SCFED of Tin into Hierarchical Alumina Templates

After successful deposition into 13 nm templates, the next step is to push towards smaller templates. This was achieved by driving the template pore diameter down using a hierarchical template that has a stepped pore diameter of < 10 nm leading to 18 – 35 nm and finishing with 100 - 170 nm, with a Cr/Au electrode deposited on the surface with the smallest pores. Sn was deposited into the templates using an electrolyte of $[N^nBu_4][SnCl]$ in

supercritical CH_2F_2 at ~180 bar and 86ºC (deposition by David Cook at the University of Southampton).

SEM imaging in Figure 3.12 shows Sn deposition throughout the template, with the higher diameter nanowires extending over 20 µm. The template appears to mimic the smaller nominal diameter templates forming in a branch like structure throughout. The diameter interfaces are clearly defined across the sample, with the smaller pores feeding into the larger pores. The planview images indicate a high filling fraction with over 60% of the pores filling deeply into the template > 10 µm.

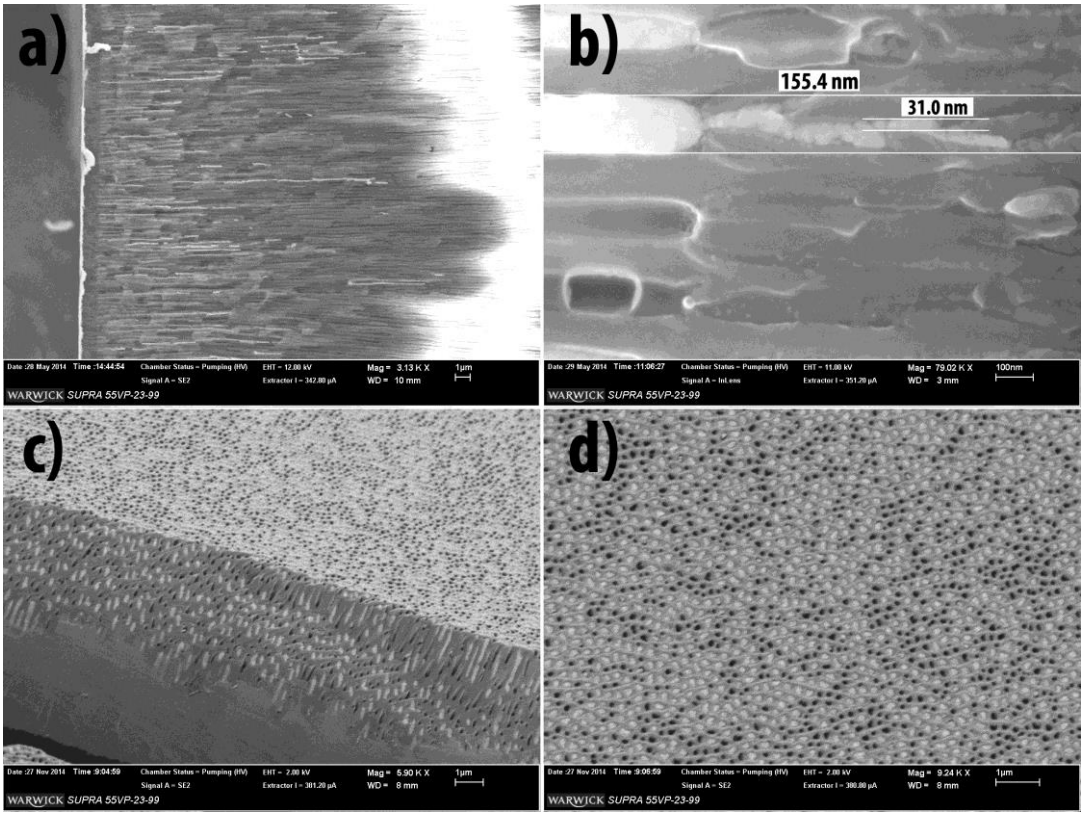

Figure 3.12: a) Low magnification cross sectional SEM image illustrating the defined 30 – 170 nm diameter transition and depth of deposition into the template. b) High-magnification image of the 30 -170 nm transition. c-d) Low magnification planview images indicating the uniform depth of filling and high filling fraction.

FIB cross-sections were prepared to allow clear imaging of the Sn/Au interface, as this region contains the smallest pores and is the initiation point for the electrodeposition.

The smallest diameter pores extend ≈ 200 nm from the Au deposition electrode before transitioning into the mid-range pores for ≈ 1 µm, with the large pore then continuing to the surface of the template. Investigation of the small diameter region, Figure 3.13 b, show a range of nanowire diameters and constrictions, fulfilling the < 10 nm criteria set out as the experimental goal. EDX maps of the interface showed a clear interface between the alumina template, Cr sticking layer and Au contact with no Au observed within the pores, Figure 3.13 c-i.

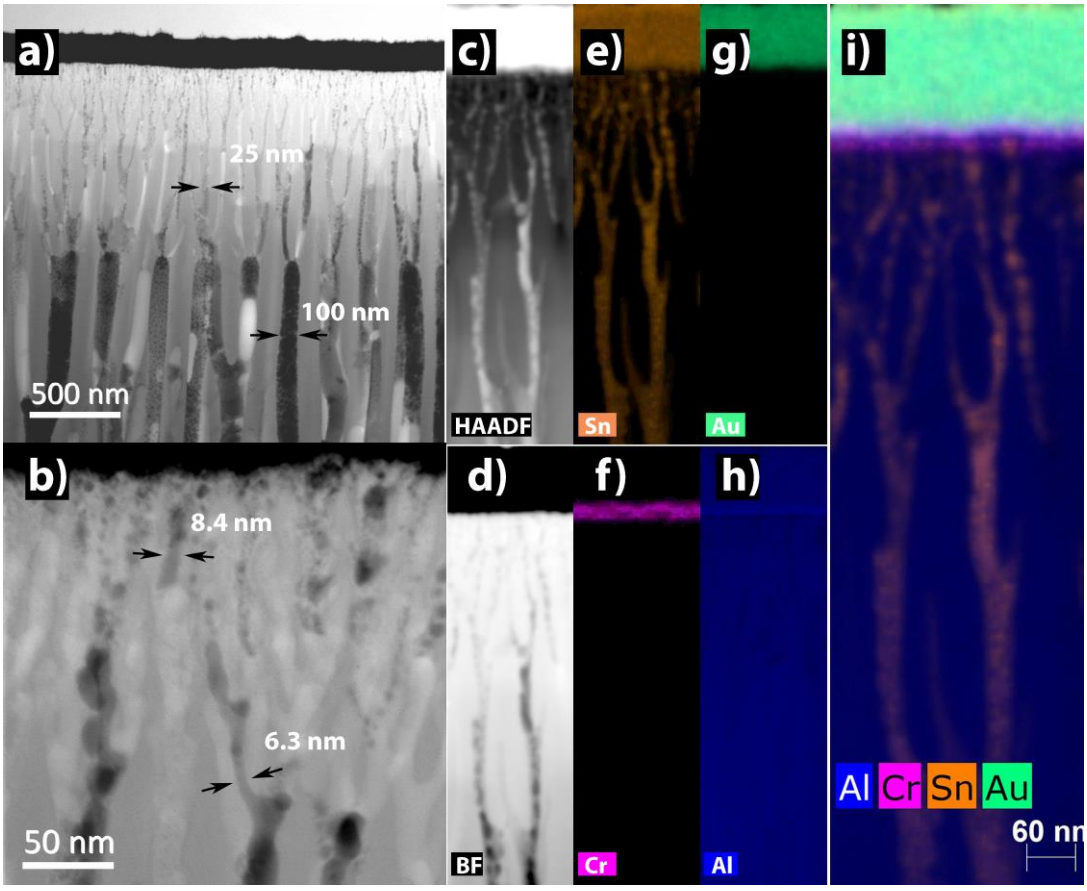

Figure 3.13: a) STEM BF image of the pore diameter transitions running throughout the asymmetric template. b) Example of the small pore region highlighting some < 10 nm pores. c-i) STEM edx maps of the small pore to Au interface including composite map.

3.5 Conclusion

SCFED is a novel electrodeposition technique that has proven to be versatile in its initial experimental phase, producing a range of different samples. This Chapter focused on the

effective use, and need, of electron microscopy when studying these systems. First, the case of planar deposition of Ge as a thin film; the resulting films' crystallinity was examined using XRD and Raman. The results suggested a large quantity of amorphous structure with some crystalline regions. SADP of the thin films indicated some form of polycrystallinity which when imaged using dark field TEM visualised the embedded crystallites within an amorphous template. This result was reinforced through analysis of the RDF of the SADPs confirming the protocrystallinity.

Application of the SCFED process to grow nanowires within porous media allows us to establish more challenging depositions. Ge deposition was successfully achieved for both 35 and 13 nm nominal diameter alumina templates. For both systems, the generated nanowires were amorphous and continuous indicating a good mass transport rate during deposition and no pore blocking arising from surface tension. The successful deposition of CuTe was the first binary system achieved using the SCFED process, an extremely challenging structure due to its formation in a range of different compositions. XRD of the sample indicated that the P4/nmm space group was dominant suggesting a Rickardite-like structure. This also led the way to further experiments with other binary systems, including BiTe, SbTe and SnTe.

High-resolution STEM (HRSTEM) imaging of the CuTe nanowires revealed regions that appeared to contain a different structure. EDX of these regions showed an increase in S, suggesting CuTeS. Within the literature there are two reported papers on CuTeS providing four very similar potential crystal structures.[141-142] SADP of the nanowire with comparisons to the simulated structures allowed the successful identification of the Cu_6Te_3S 293 K α phase structure. It is believed that these are the first ever images of this system in atomic resolution.

In attempts to drive down the nanopore diameter an experimental hierarchical template was developed to create sub 10 nm nanowires. The template structure was analysed

as small sub 10 nm pores penetrating ≈ 200 nm into the template, this then transitioned into the 18 – 35 nm region for ≈ 1 μm before transitioning into > 100 nm pores that extending throughout the rest of the template. Sn was successfully deposited into the pores with uniform deposition across a high fraction of pores to depths > 10 μm. It is key to note that for the deposition to occur the supercritical fluid must have been in contact with the Au electrical contact. Therefore, for nanowires to be observed in the > 100 nm pores it is assumed that deposition has occurred within the sub 10 nm pores. This is believed to be one of the smallest successful depositions into hierarchical templates with sub 10 nm constrictions. It is expected that a standard aqueous electrodeposition would not be able to penetrate the sub 10 nm pores because of surface tension.

The Effects of Heating on Bismuth and Tellurium Nanowires

4.1 Introduction

Advances in TEM sample holders have allowed access to in situ methods in electron microscopy experimentation. In situ experimentation allows the user to observe, in real time, the direct effect of an applied stimulus. These variables may be independent or in combination, e.g. sample heating or cooling, the application of an electric field using a nanoprobe, or the release of a gas into the vacuum environment, in proximity to the area under observation.[143-147] As TEM is a microscopy technique, it can be challenging to look past the obvious explanation for what you observe. An example being the observation of a SnO nanowire melting at elevated temperatures within the TEM by Hudak, here they potentially erroneously suggest a solid-liquid-vapor phase transition with a 35% reduction in melting temperature from 1080 to 700 °C.[148] This would be a correct assumption under standard atmosphere but this is not necessarily true for in situ high vacuum experiments. Therefore, it is essential to fully account for all of the experimental variables within a system to accurately categorise a phase transition as: melting, evaporating or sublimation, as shown throughout this Chapter.

This Chapter discusses the effects of in situ nanowire heating under high vacuum within the TEM. The first Section focuses on tellurium nanowires, encapsulated in a thin (≈ 2 – 3 nm) alumina sheath, proving that they undergo sublimation, the phase transition from solid to gas, with no intermediate liquid phase. Using in situ videos, the experimental rate of sublimation is calculated and compared to the Hertz-Knudsen model. Theoretical calculations of a pressure drop across a continuous pipe suggest that the remnant alumina is flawed with potential holes and discontinuities. The process of impurity concentration in the

remaining material is proposed to explain an observed reduction in sublimation rate, and its eventual halt. The final Section analyses bismuth nanowires under similar conditions. These nanowires do not sublime but undergo a phase transition from solid to liquid, see Section 1.2.4. In the liquid state the average atomic spacing is calculated from electron diffraction patterns using a radial distribution analysis.

4.2 Tellurium Sublimation

4.2.1 Tellurium Nanowires

A Tellurium complex of ($[N\mathit{n}Bu_4]_2[TeCl_6]$) was electrodeposited into approximately 100 µm thick porous anodic alumina templates (with nominal pore sizes of 13 and 55 nm and Cr/Au electrodes) from supercritical R32, in a process previously outlined (deposition by David Cook at the University of Southampton).[149] A focused ion beam lift-out was used to obtain a cross-section TEM specimen of the bottom of the nanowires and the electrode. An elemental analysis using EDX is shown in Fig. 4.1b, ignoring the aluminium and oxygen signals from the template. The Au electrode and thin Cr adhesion layer are clearly visible, as well as individual Te nanowires ~ 13 nm in diameter. The interface between the nanowires and electrode appears sharp, with no intermetallic compound present. The nanowires appear discontinuous, although electrodeposition requires that electrical conductivity is maintained for deposition to take place. This could be a loss of material during preparation of the thin TEM specimen; although high temperatures are not expected during FIB specimen preparation Te is the material most easily lost, with the lowest threshold for sublimation- as investigated further in this chapter. The alumina templates were dissolved by immersing the sample in a concentration of 4M NaOH and washing in IPA and deionised water, leaving the Te nanowires attached to the electrode. The clean nanowires were then dispersed by sonication in IPA and drop cast onto a 3.05 mm copper grid with lacey carbon support film.

The Te nanowires were also imaged using SEM after dissolution of the template but prior to sonication i.e. whilst still contacted to the deposition electrode, Figure 4.1 a. The unsupported nanowires bundle up and average tens of microns in length. EDX analysis of the nanowires, undertaken on a FIB cross section in Figure 4.2 b, indicates a defined growth interface with no contamination of visible reactions between the Au electrode, Pt sticking layer and Te nanowires.

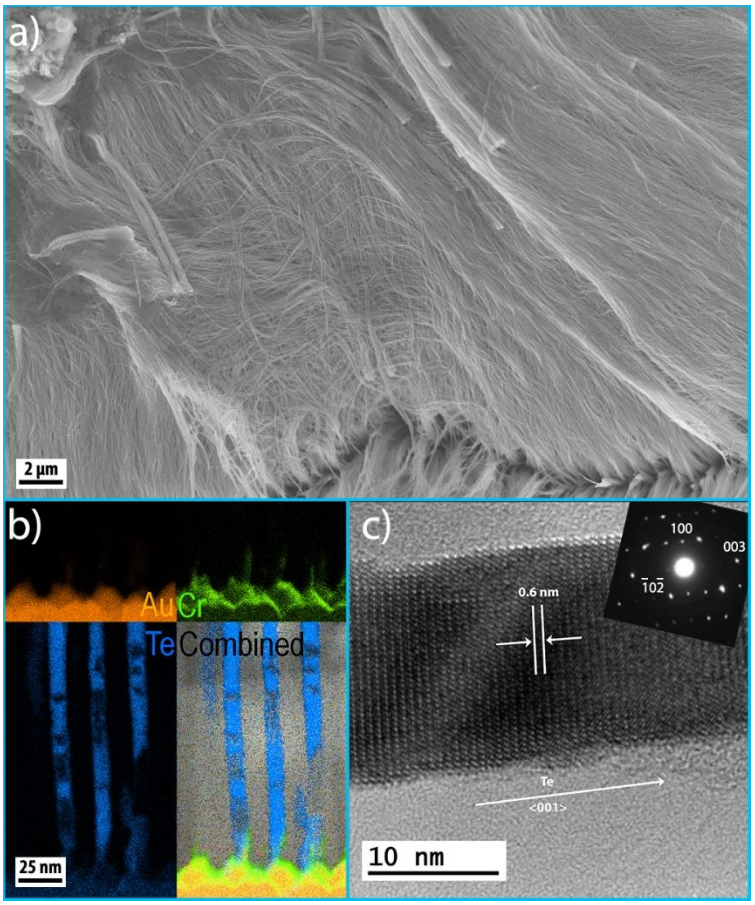

Figure 4.1: a) SEM image of tellurium nanowires after dissolution of the alumina template. The nanowires are connected to the electrode (bottom right), have a uniform diameter and are have lengths of at least tens of microns. b) EDX map from a FIB prepared cross section of the Te/Au growth interface. No impurities were observed with well-defined Te – Pt/Au interfaces. c) TEM image of a single released nanowire highlighting the 001 growth orientation confirmed by the inset SADP.

A typical released Te nanowire from the nominal 13 nm sample is shown in Figure 4.1 c. The nanowires have a variable diameter, ranging between 9 and 25 nm, as a result of

the rough inner surface of the pore in the template. The selected area diffraction patterns (SADP) of the nanowires show the nanowire to be a single crystal, forming in the bulk P3121 space group with its long axis (i.e. the growth direction) along [001]. Although not apparent in Fig. 4.1 b, the nanowire is sheathed in a layer of amorphous material, ~2-3 nm thick, this becomes visible after sublimation.

4.2.2 Tellurium Sublimation

The melting point T_{melt} of pure Te at atmospheric pressure is 449.5 °C.[150] It is known that when heated, materials with dimensions < 50 nm will undergo a size-dependent reduction in melting temperature.[151] Studies on Sn particles by Lai suggest a reduction in melting temperature by approximately 4, 10 and 30% for nanoparticles with 20, 10 and 5nm dimensions respectively.[152] Therefore, we predict a decrease in Te melting temperature by ≈ 7 – 8 %. There have been several cases of in situ nanowire melting with extremely high melting point reduction percentages. Sun reported 40 – 80 nm GeTe nanowires undergoing a 46% melting reduction of 335 °C whilst Shaygan reported a 30 nm ZnTe nanowire undergoing a 65 % melting reduction with both reports emphasising solid to liquid melting transisions.[153-154]

The material will sublime at temperatures below T_{melt} when its vapour pressure exceeds the ambient pressure. The ion pump pressure of the 2100 LaB_6 TEM, P_{TEM} used for this investigation is typically ~5 x 10^{-7} mmHg during standard operation. Although the ion pump is not immediately adjacent to the specimen, the vacuum at the specimen is augmented by a liquid nitrogen cooled cryo-shield (‘cold finger’), which also acts as an anti-contamination trap and therefore the specimen vacuum is considered to be the same as the ion pump vacuum. The vapor pressure of many materials is described very well by the extended Antoine equation

$$log_{10}(P_v) = A - B/(T + C) \qquad (4.1)$$

where P_v = vapor pressure (in mmHg), T = absolute temperature (in Kelvin) and A, B, C are constants.[155] For Te, A = 6.6385, B = 4084 and C =98.94,[156-157] giving the characteristic vapor pressure curve of Figure 4.2. This shows that heating of Te inside the TEM is well inside the sublimation regime, and that sublimation should commence at approx. 220°C.

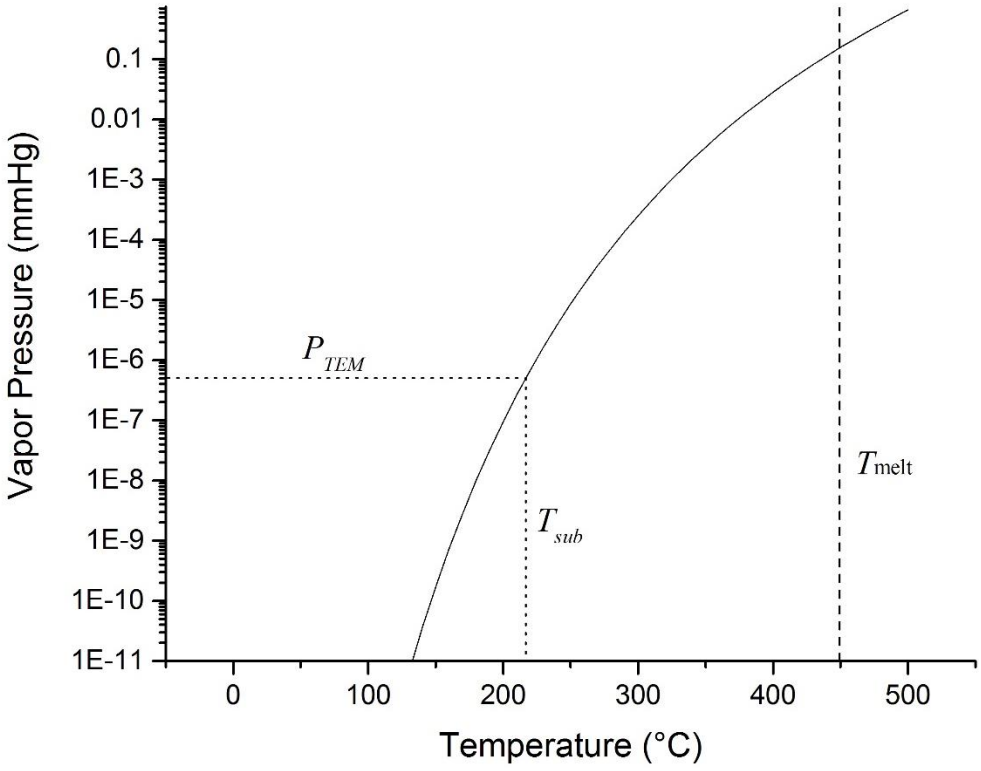

Figure 4.2: Vapour pressure of tellurium as a function of temperature from Eq. 4.1. Sublimation is expected when this exceeds the pressure in the TEM (horizontal line) and should occur well below the melting point of Te at 449.5 °C (vertical line).

Direct confirmation of the lack of any liquid intermediate phase between the solid Te and vacuum is presented in Figure 4.3. The nanowires were heated using a Gatan model 652 water-cooled specimen heating holder. Figures 4.3 a-c show three bright field images at intervals of 0.5s from a sequence taken at 10 frames/second and a thermocouple temperature of 255 ºC. An obvious loss of material from the nanowire is visible, with the thin alumina sheath remaining as a tube to the left of the image. Figures. 4.3 d-f are dark field images of the same nanowire some time later. These images are formed by a diffracted beam, which

can only be produced by Bragg scattering from crystalline material; the crystal appears bright on a dark background. This shows that the material remains solid and crystalline, i.e. loss of material is demonstrably due to sublimation rather than evaporation from the liquid phase.

Further evidence is given in Figures 4.3 g-I, which show lattice fringes in the Te at a thermocouple temperature of 250 °C indicating its crystalline nature while material sublimes from the surface. These prove the lack of an intermediate liquid phase that would be present if the nanowire was melting and evaporating at a temperature lower than the bulk material. This suggests that the reductions in melting temperature previously mentioned and reported by Hudak, Sun and Shaygan are more likely incorrectly identified vapor pressure related sublimations.[148, 153-154]

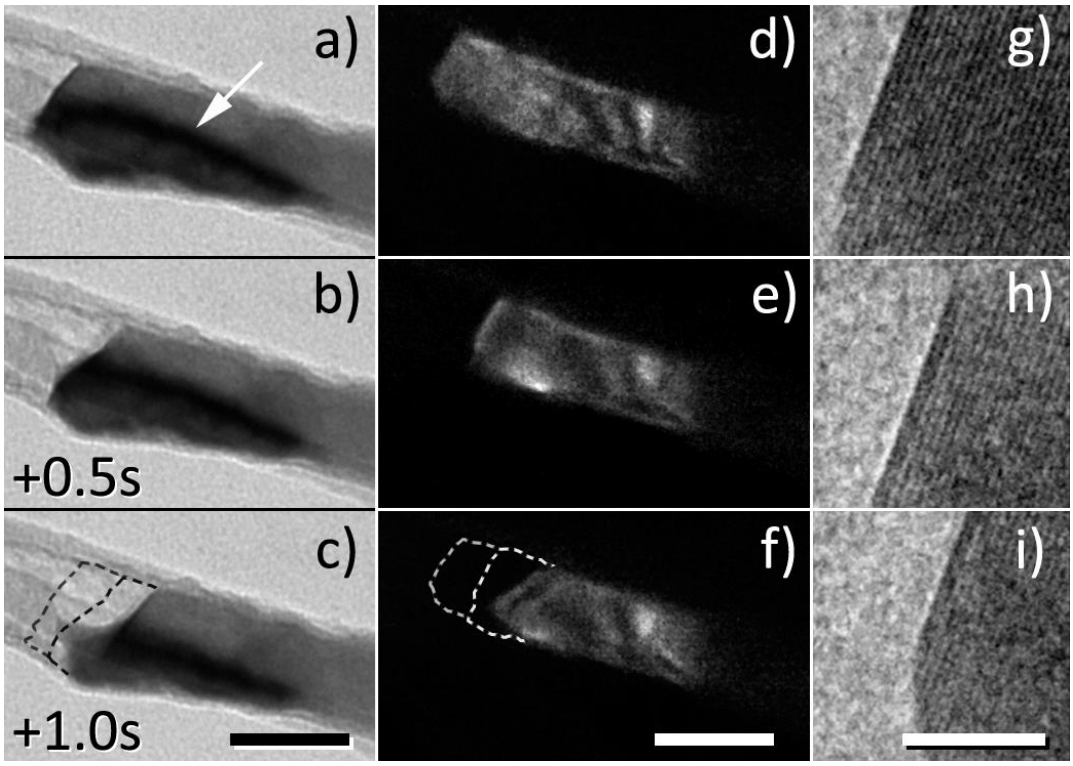

Figure 4.3: Sublimation of a Te nanowire with diameter ≈ 13 nm at a thermocouple temperature of 255 ºC. a-c) Bright field TEM images at time intervals of 0.5 seconds, the loss of Te by sublimation from the nanowire. (10 nm scale bar) d-f) A similar set of dark field TEM images showing that the material is crystalline, and therefore solid, as the sublimation front travels down the nanowire. (10 nm scale bar) g-i) A set of higher magnification images showing crystalline lattice fringes observed throughout sublimation. (5 nm scale bar)

The nanowires are heated via thermal radiation from a furnace that encapsulates the Cu grid and by electron beam irradiation. Therefore, it is expected that there may be some discrepancies between the temperature at the nanowire and the thermocouple. However, as the sample is at high vacuum the thermal radiation loss should be minimalised and the electron beam effects should be low due to the metal thermal conductance of Te and small dimensions of the nanowires.

The amount of material lost from the nanowire during sublimation can be extracted through the examination of individual frames within the recorded videos. This is undertaken by extracting the timestamp from each fifth frame and comparing the change in nanowire length, recorded as length sublimed. The rate of change of length, hereafter called the rate of sublimation, can then be calculated by finding the gradient after fitting the lines or dividing the length sublimed by the total time of sublimation. Examples of such are shown in Figure 4.4 a and there appears to be no correlation between rate of sublimation and nanowire diameter.

In Figure 4.4 a, nanowires of varying diameters were heated to 215, 248, 250 and 255 ºC allowing for the sublimation to be observed and recorded. The rate of sublimation is not smooth due to edge wetting effects, where the surface impingement increases at regions of alumina variation, an example can be seen in Figure 4.3 c. The sublimation can be seen to pause for ≈ 10 seconds for the 12 and 13 nm nanowires. Examination of the footage, Figure 4.4 b – c, indicates that this is due to impingement on large foreign contaminants, > 5 nm in diameter, within the nanowire. It is suspected that the mass of the contaminant is too high to be transported along the nanowire, see Section 4.2.5, and therefore blocks the quantity of vacuum exposed to the Te, generating the pause.

The experimental rate of sublimation was calculated for a range of different diameter nanowires at different temperatures between 215 and 250 ºC. The nanowire diameter was

ignored whilst averaging as it is expected to have no effect on the rate of sublimation, as shown below in Section 4.2.3. The experimental rates of sublimation were then averaged, as shown in Table 4.1. The average experimental results are compared to the theoretical rates in Figure 4.5.

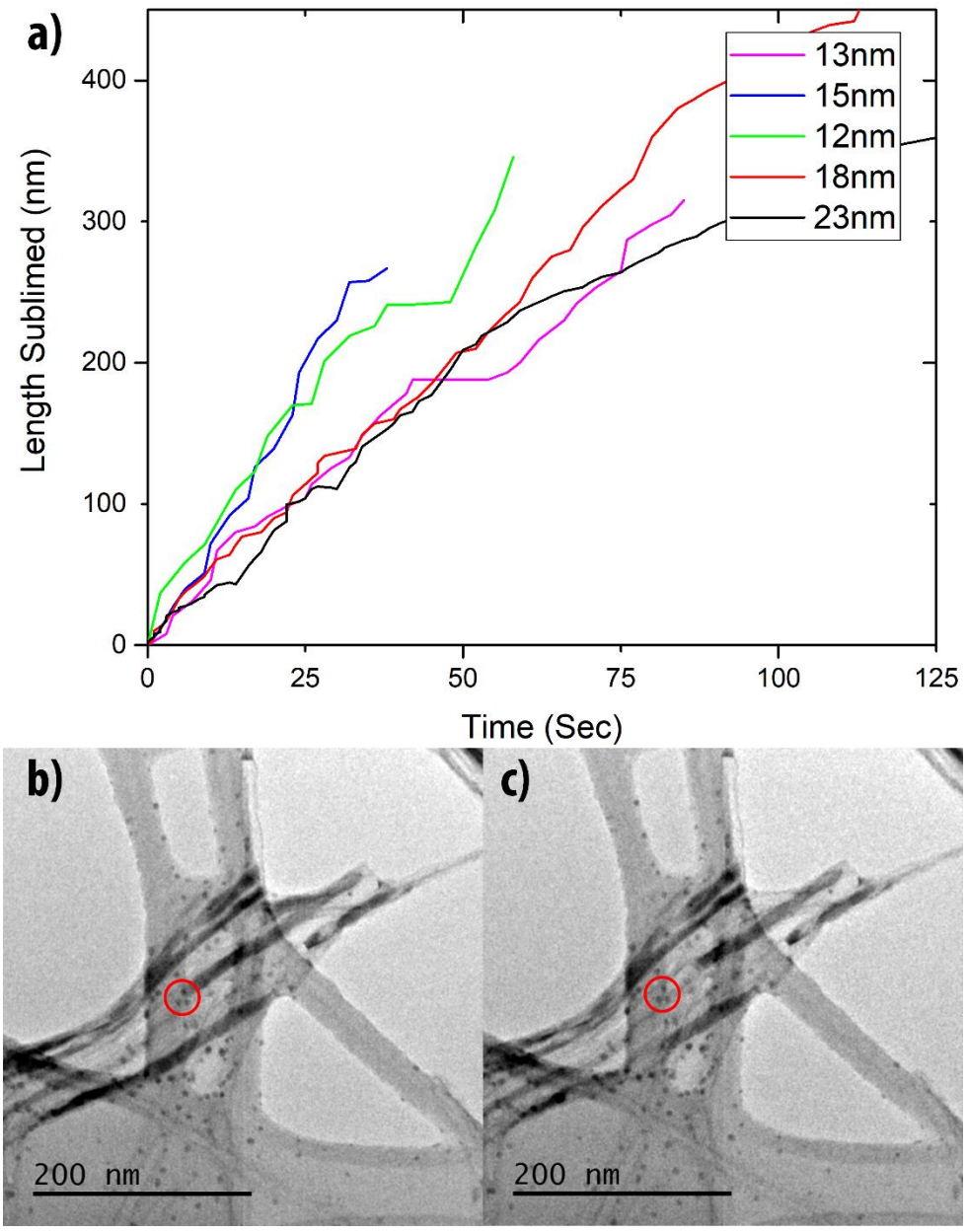

Figure 4.4: a) Representative plot of the quantity of nanowire sublimed over time. There are some fluctuations in the rate of sublimation varying between 3.5 nm s^{-1} and 5.1 nm s^{-1}. b) 12 nm nanowire during a contamination impingement sublimation pause. c) The same nanowire during the renewed sublimation, the contaminants have remained in place whilst the Te sublimes around it.

Temperature (°C)	Average rate of sublimation (m s^{-1})
215	3.9 x 10^{-9}
220	7.9 x 10^{-9}
230	1.0 x 10^{-8}
235	8.7 x 10^{-9}
240	2.1 x 10^{-8}
245	1.0 x 10^{-8}

Table 4.1: The average rate of sublimation as a function of thermocouple temperature between 215 and 245 °C.

4.2.3 Theoretical Rate of Sublimation

For the conditions used in these experiments we expect Langmuir-type sublimation i.e. sublimation under high vacuum. Mass transport occurs once the pressure and temperature are high enough that the vapor pressure of the nanowire is greater than or equal to the partial pressure of the system. The flux of molecules leaving the system, $\frac{dN}{dt}$, can be described by the Hertz-Knudson equation[158]

$$\frac{dN}{dt} = \frac{(P_v - P)A}{\sqrt{2\pi mkT}} \qquad (4.2)$$

where P_v = vapor pressure, P = system pressure, k = Boltzmann constant, m = mass, T = temperature and A = surface area of the sublimation front of the nanowire. A single unit cell of Te contains three Te atoms in a volume, V, of 1.01x10^{-28} m^3. Therefore, the flux of molecules per second, equation 4.3, can be calculated as

$$\frac{dN}{dt} = \frac{3A}{V}\frac{dr}{dt} \qquad (4.3)$$

where $\frac{dr}{dt}$ is the length of nanowire sublimed with respect to time. Equations 4.2 and 4.3 can be combined to show $\frac{dr}{dt}$ as a function of temperature and pressure, this is shown by equations

4.4. It is interesting to highlight that $\frac{dr}{dt}$ is independent of the nanowire diameter as the area of the nanowire is cancelled.

$$\frac{dr}{dt} = \frac{(P_v - P)V}{3\sqrt{2\pi mkT}} \qquad (4.4)$$

A plot of $\frac{dr}{dt}$ against T, Figure 4.4, is combined with the average experimental rate of sublimation extracted from multiple sublimation videos for temperatures between 215 and 245 °C.

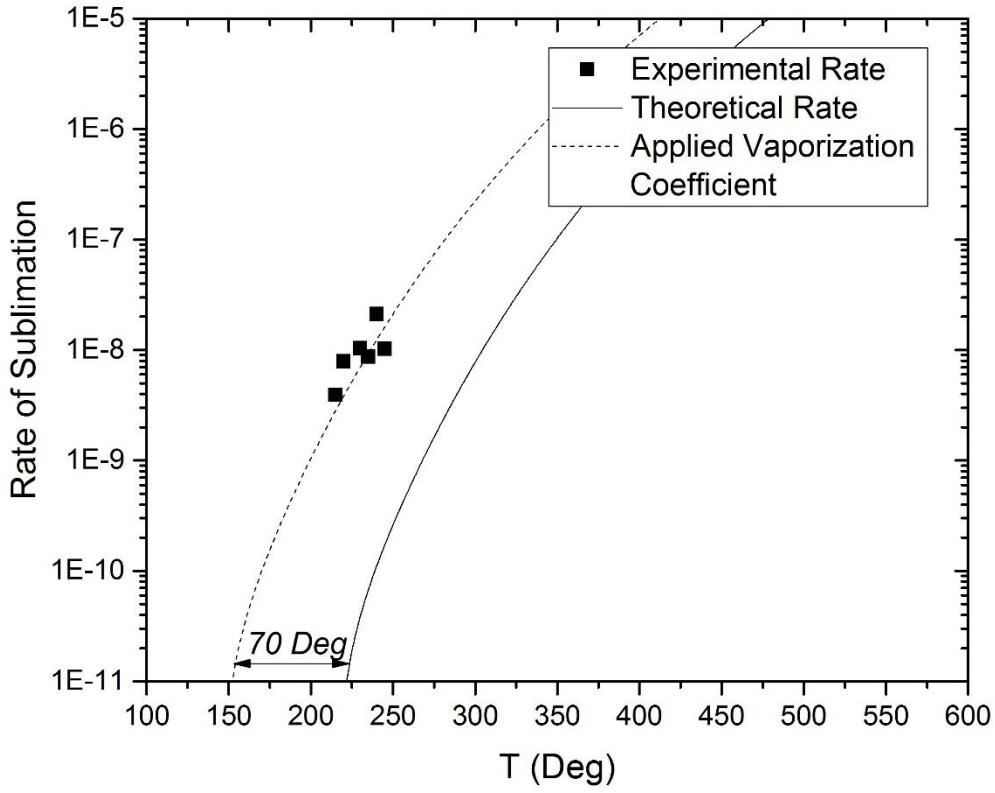

Figure 4.5: A plot of the theoretical and average experimental rates of sublimation against temperature. The dashed line represents the application of a vaporization coefficient 0.9, this translates the theoretical rate of sublimation by -70 ºC. The correlation between the applied vaporization coefficient suggesting a similar relationship between experiment and theory with some inaccuracies, most probably in temperature measurement.

The experimental rate of sublimation is significantly higher than the theoretical rate. This is probably due to inaccuracies in the temperature and pressure measurements and

partially described by the inclusion of a multiplying factor known as the coefficient of evaporation, α.[159]

$$\frac{dr}{dt} = \frac{\alpha(P_v - P)V}{3\sqrt{2\pi mkT}} \qquad (4.5)$$

An evaporation coefficient, α, of 2 x 10^{-3} translates the theoretical calculations by 70 ºC creating a high level of conformity with the experimental results, shown in Figure 4.5. This coefficient accommodates for the interaction between the Te gas molecules and the sublimation front, in which a small quantity of sublimed Te can be reflected back towards the sublimation front and impinge on the surface.[160-161] The evaporation coefficient should always be unity or below with values typically ranging between 0 and 1.[162] This experimental result is similar to the value calculated by Yim for GeTe of ≈ 10^{-3}, in which GeTe nanowires were sublimed by heating inside an electron microscope.[163]

4.2.4 Pressure Drop

No significant Te redeposition is observed and it is expected that the Te is instantly removed to the vacuum by the pressure difference between the sublimation interface and the vacuum. As the excess alumina remains in contact with the nanowire it acts to create a pipeline around the nanowire, visible in Figure 4.3a, therefore once sublimation has begun the nature of the gas flow must be explained by gas flow dynamics within pipes.[164] The kinetics are described by three regimes and governed by the Knudsen number. The three regimes are:

I) Continuum flow, $Kn < 0.01$, the mean free path is smaller than the diameter of the pipe and consequently the gases interactions are dominated by intermolecular collisions compared to wall collisions. The flow in this regime is often referred to as viscous with fluid like characteristics.[165]

II) Molecular flow, $Kn > 1$, the mean free path is of the same order, or greater than, the diameter of the pipe, resulting in the flow being dominated by molecule to

wall collisions. All resemblance to fluid like behaviour is lost as there are no intermolecular collisions.[166]

III) Transitional flow, $0.01 < Kn < 1$, an intermediate regime between continuum and molecular flow where both intermolecular collisions and molecule wall collisions are common. The combination of the two interactions or lack of a dominant interact complicate analysis of gases in this flow regime.[167]

The Knudsen number, *Kn*, is defined as the ratio of the mean free path, λ, to the diameter of the pipe, d. The λ of Te under the observed conditions is 72.8 m where

$$\lambda = \frac{kT}{\sqrt{2}\pi d^2 P} \qquad (4.6)$$

K is the Boltzmann constant, T the temperature (Kelvin), d is the nanowire diameter and *P* the pressure inside the TEM. The exact diameter of excess alumina pipe is irrelevant due to the orders of magnitude difference but for continuity assuming a 13 nm pipe then *Kn*, equation 4.7, suggests a Knudsen number of 7.3×10^9 and the sublimed gas would therefore follow the molecular flow regime.

$$Kn = \frac{\lambda}{d} \qquad (4.7)$$

As the system is being treated as a pipe, the throughput of the pipe, Q, can be calculate as the rate of volumetric flow with respect to time.[168]

$$Q = p\frac{dV}{dt} = kT\frac{dN}{dt} \qquad (4.8)$$

With the observed sublimation rate of 10 nm s^{-1} the number of molecules per second, $\frac{dN}{dt}$, equals 1.1×10^4 molecules s^{-1}, giving a throughput *Q* of 7.9×10^{-17}. The conductance, *C*, of a long cylindrical pipe under molecular flow is given by the Knudsen formula[169]

$$C = \frac{D^3}{6L}\sqrt{\frac{2\pi kT}{m}} \qquad (4.9)$$

where *D* is the pipe diameter, *L* is its length and m is molecular mass. For Te_2 molecules with a mass of 4.24×10^{-25} kg, at 500 K, in a pipe of 10 nm in diameter and 1 μm in length, the conductance C is 5.33x10-17 $m^3\ s^{-1}$.

The conductance and throughout are related by the pressure drop along the pipe governed by

$$C = Q\delta p \qquad (4.10)$$

where δp is the difference in pressure at the ends of the pipes. By applying the results from equation 4.8 and equation 4.9 a pressure drop of $\frac{C}{Q}$ = 1.5 Pa or 1.13×10^{-2} mmHg would be expected. At this pressure, the rate of sublimation should rapidly decrease and stop, however, this is not observed suggesting that the excess alumina "pipeline" contains multiple defects and escape points. This is interesting, as for multiple defects you would expect multiple sublimation fronts, however, a single sublimation front is observed during experimentation.

4.2.5 Contamination Transport

In some samples, the rate of sublimation was observed to decline once the sublimation front approached the encapsulated end. If a nanowire is contaminated with a small quantity of a foreign element that does not sublime, it will remain in the nanowire while the Te sublimes. The foreign element thus becomes more concentrated in the nanowire as sublimation proceeds. A build-up of contaminant on the sublimation surface may be responsible for the stop-start behaviour observed in some nanowires. Diffusion of the contaminant into the nanowire would allow sublimation to recommence. Nevertheless, the concentration of contaminant must increase as the volume of the nanowire shrinks, eventually bringing

sublimation to a halt by blocking the surface or the formation of a binary system of contaminate and Te that does not sublime.

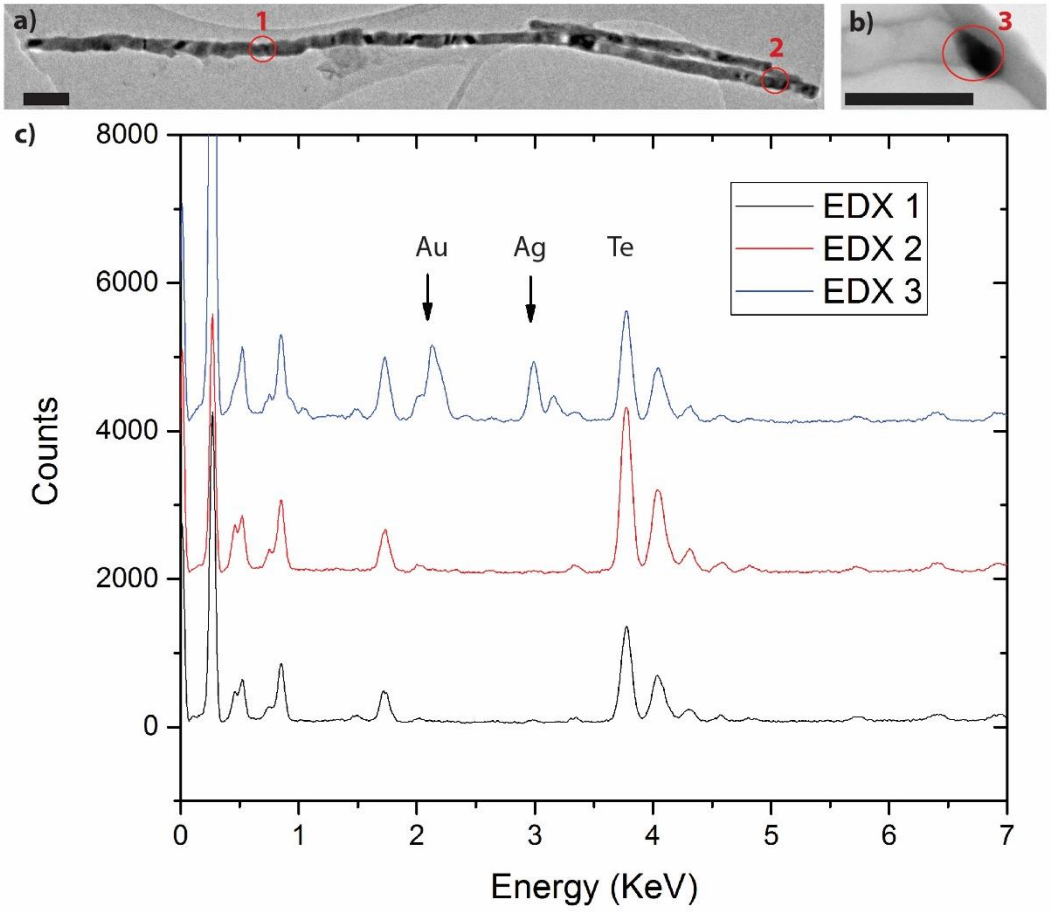

Figure 4.6: a) Low magnification TEM image of Te nanowire before heating and sublimation. b) Post sublimation remnant nanowire, approximately 50nm in length. c) Three EDX spectra from locations indicated in a) and b), all three spectra are practically identical apart from the huge increase in Ag and Au signal in the post sublimation nanowire. (Scale bar 100nm)

This was quite common throughout the samples with EDX analysis showing that the Nanowires were contaminated with Ag and Au, which were present in the supercritical electrochemical cell, although they were supposed to be isolated from the electrolyte by encapsulation in epoxy. Presumably this encapsulation failed, allowing them to be dissolved into the electrolyte and participate in the electrodeposition process. EDX measurements taken before sublimation, Figure 4.6a spectra 1 and 2, show no contamination, whilst EDX

of the final material after sublimation had halted, Figure 4.6c, shows approximate 2:1 ratios of Te to both Au and Ag, Table 4.2. The contamination was removed from the samples by changing the contact electrode from Au to Pt for the SCFED.

	Te (At %)	Ag (At %)	Au (At %)
Spectrum 1	8.9	0.2	0
Spectrum 2	13.6	0	0
Spectrum 3	7.0	2.8	4.1

Table 4.2: Approximate EDX quantification for a Te nanowire before and after sublimation. A sample density of 8.32 g cm^{-3}, representative of AgTe, is applied with a thickness estimated at 50 nm.

4.3 Liquid Bismuth Analysis

Bismuth was successfully deposited from a complex of tetrabutyl ammonium bismuth tetrachloride, [N*n*Bu_4][$BiCl_4$], into anodic alumina templates with Cr/Au electrodes from supercritical R32 (deposition by David Cook at the University of Southampton). Two different types of anodic alumina templates were used with a nominal pore diameter of 35 and 80 nm. The 80 nm templates contained a wider range of pore diameters with the 35 nm templates having a range of 20 – 40 nm and the 80 nm template ranging between 60 and 100 nm. Again the template was dissolved by immersing the sample in a concentration of 4M NaOH. The sample was washed in IPA and deionised water before the nanowires were released by sonication in IPA and drop cast onto a 3.05 mm copper grid with lacey carbon support film.

A typical released Bi nanowire from the nominal 35 nm templates is shown in Figure 4.7 a. The inset SADP shows the nanowire to be single crystal consistent with a bulk $R\bar{3}mH$ space group and a growth direction (long axis) along the $[110]$ direction, perpendicular to the $[\bar{1}1\bar{2}]$ plane.[170] Significant diameter variations can be observed with 20 nm constrictions and 50 nm expansions

4.3.1 Proof of Phase Change

The melting temperature of Bi is 271.4 °C, at this temperature solid Bi will undergo a phase change into a liquid.[171] The phase change from solid to liquid can be induced during imaging by heating the sample, an example of this phase change is shown in Figure 4.7. The nanowires appearance does not change much during this transition, as shown in Figure 4.7 a and d at 27 and 257 °C respectively. Like the Te discussed in the previous section, the Bi is confined within remnant alumina, this prevents it from flowing and losing its shape. Yet, by observing the nanowires diffraction pattern during heating, the transition from solid to liquid is easily identified as the ordered crystal structure breaks down and the atoms form into a liquid, with an isotropic spacing distribution. This is apparent from the transition of bright diffraction spots in Figure 4.7 b to diffuse diffraction rings in Figure 4.7 c.[172]

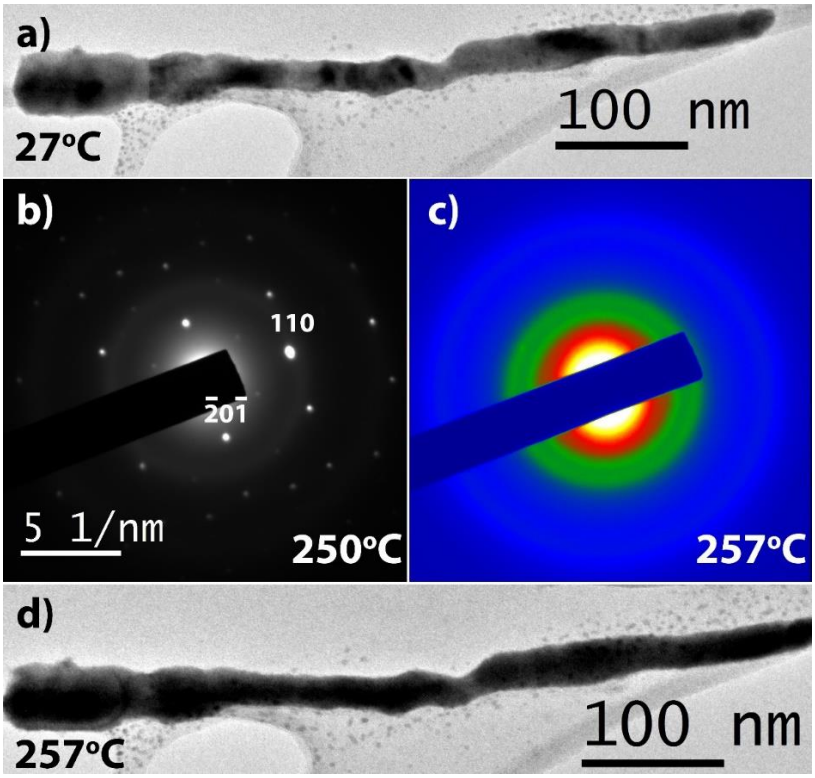

Figure 4.7: a) Typical 35 nm crystalline Bi nanowire imaged at room temperature. b) SADP of the nanowire in a) at 250 °C showing a crystalline diffraction pattern. c) SADP of the same nanowire at 257 °C, the diffraction pattern is no longer crystalline and is now amorphous. d) Image of the same nanowire in a) now at 257 °C, it is no longer crystalline but holding its structure as an enclosed liquid.

4.3.2 Radial Distribution Analysis

The encapsulation of the nanowires allows them to be examined for extended periods of time, e.g. up to ten minutes or longer, without fear of sample damage or movement. This was used to advantage in the acquisition of high dynamic range electron diffraction (HDR-ED) patterns. This technique uses multiple exposure times, from fractions of a second to several minutes, that are combined into a single dataset.[173] A key advantage of a HDR-ED pattern compared to a conventional SADP is the ability to acquire a diffraction pattern without a beam stop in the high intensity parts of the pattern and, due to the longer exposure, acquire sufficient counts to avoid low signal to noise ratios in the data, this allows for cleaner analysis and is easily observed in Figure 4.8.

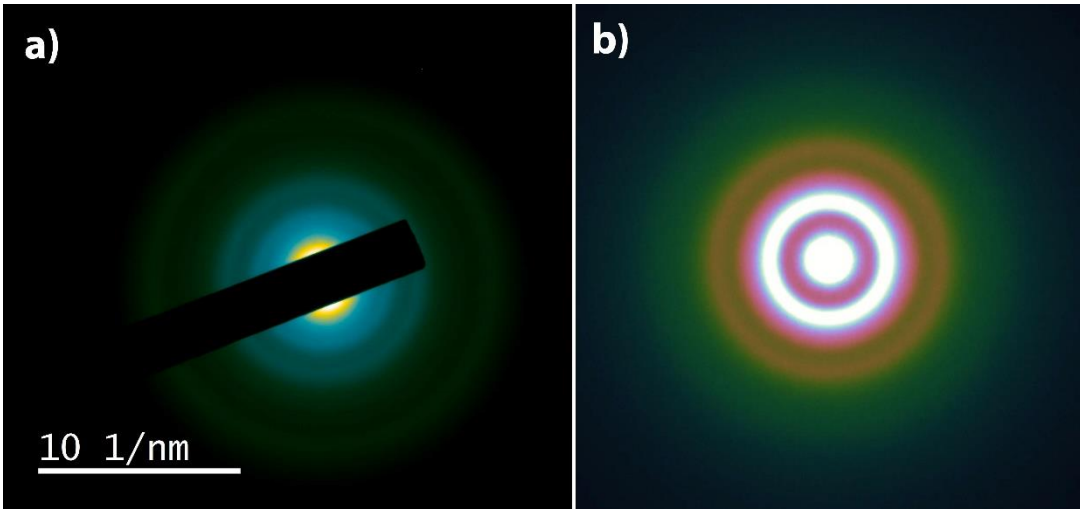

Figure 4.8: a) 25cm SADP of Bi nanowire at 257 °C using a beam stopper with a 5 second exposure. b) HDR-ED of a similar Bi nanowire at 300 °C with no beam stopper and an initial exposure of 60 seconds and a total acquisition time of approximately 5 minutes.

Once acquired, the HDR-ED data were analysed using the *RDFTools* plugin to generate the RDF plots, as described in Section 2.4.4.[123] The parameters for analysis with the *RDFTools* plugin were examined to find the optimum number of pixels to average over whilst maintaining the structural information and intensity of the image. Averaging is the sum of the signal of a pixel width from the centre of the diffractogram. It was used to increase the signal to noise ratio, allowing for the analysis of higher radii. Care must be taken when

averaging as at high numbers the curvature of the diffraction pattern will begin to cause interference and may mask results. Figure 4.9 a explores the effect of these parameters, suggesting a pixel average of 40 provides the optimum detail, whilst maintaining the natural intensity ratio of the peaks. Calculation parameters were set with a Bi density of 9.78 g cm^{-1}, a plot range of 20 Å, an initial beam cut of 0.8 Å and a plot resolution of 1200 pixels. RDF plots were also generated for a post sublimation remnant alumina nanotube and the lacey carbon support film, checking for signal interference. There is no evidence of interference, RDF plots are shown in Figure 4.9 b, justified by the lack of key low r peaks from the C and Alumina having no constructive interference on the acquired Bi RDF.

The data extracted from the RDF plot of a 13 nm nanowire of liquid Bi at 300 °C shows a high amount of correlation with the data obtained from the same experiments undertaken for bulk Bi using x-ray diffraction (XRD) and neutron diffraction. The average atomic spacing is described through a first peak at 3.47 Å, a hump at 4.92 Å and a peak at 6.5 Å, the plot agrees with the works published by Greenberg, Isherwood, Emuna, Waseda, Sharrah and Akola, highlighted below in Table 4.3.[174-179]

Author	1st Peak	2nd Peak	3rd Peak
Myself	3.47	4.92	6.5
Greenberg	3.28	4.65	**6.6**
Isherwood	3.4	**4.8**	**6.9**
Emuna	**3.5**	**5**	**6.6**
Waseda	**3.1**	N/A	**6.5**
Sharrah	3.35	**4.8**	6.8
Akola	3.08	**4.9**	**6.7**

Table 4.3: A summary of peak spacings observed in RDF measurements of liquid bismuth by various authors. All measurements are undertaken using Neutron diffraction or XRD apart from Akola who has produced simulations from DFT. Bold numbers are interpreted from graphs whilst normal numbers are stated by the author.

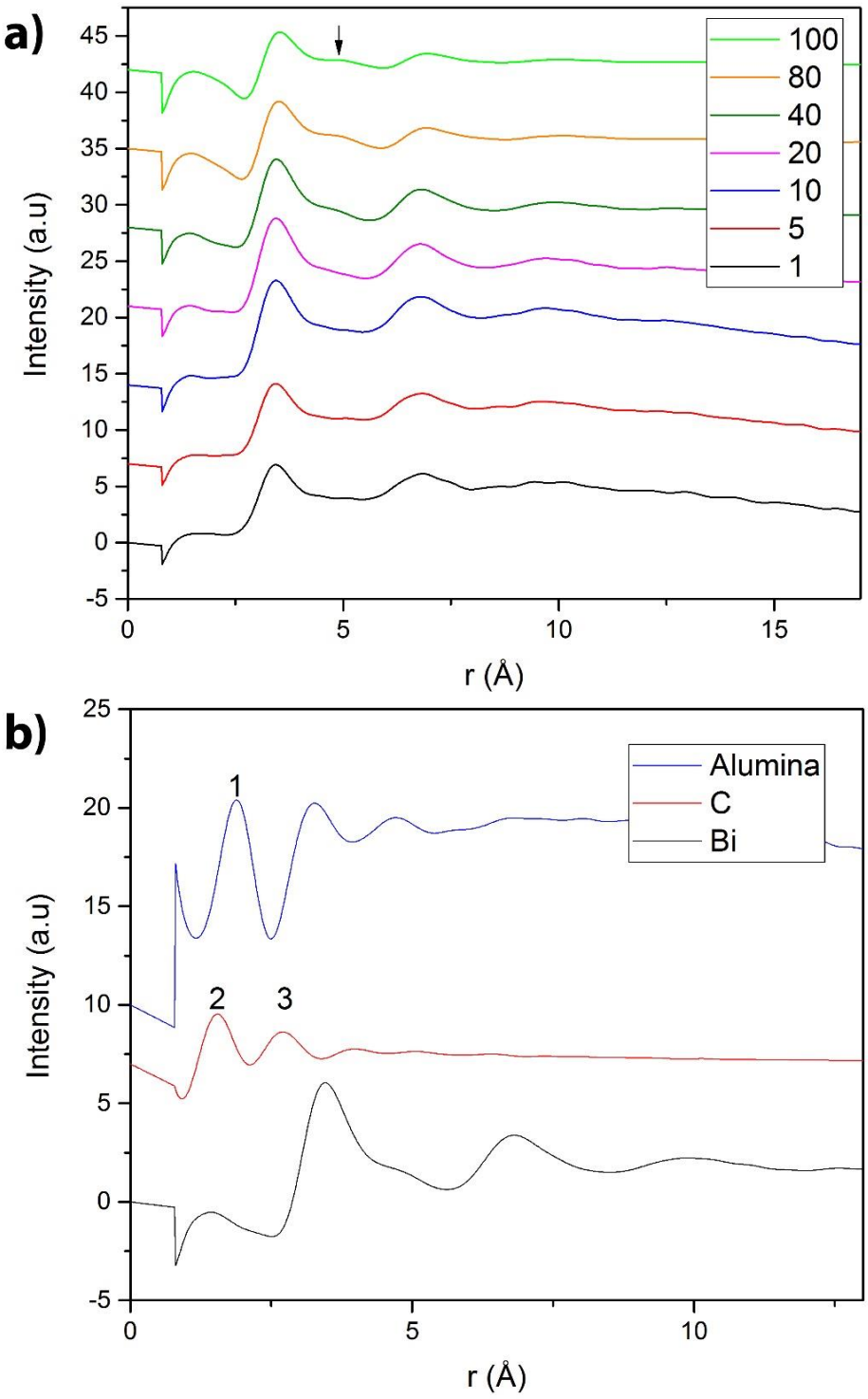

Figure 4.9: a) RDF analysis of a stable liquid Bi nanowire at 300 °C for a range of different averaging parameters. The second peak highlighted by an arrow is indistinguishable in plots < 40 and the ratio of peak intensities is decreased for plots > 40. b) RDF analysis of remnant empty alumina pore, lacey carbon support film and liquid Bi nanowire. The lack of interference from the labelled peaks 1, 2 and 3 in the Bi suggest that little to no background signals are interfering with the results.

The previously reported liquid Bi data has predominantly been acquired using Neutron diffraction and XRD from a sample volume of mm^3. Here we report the first results from electron diffraction analysing a sample volume of nm^3. Therefore, this data is acquired from a volume measurement $\approx 1 \times 10^{12}$ times smaller than any other reported measurements, highlighting the ability to provide nanoscale analysis where X-ray measurements are impossible.

The continual heating of the sample beyond the melting point leads to the Bi evaporating at 440 ºC, 1124 ºC below the 1564 ºC boiling point of Bi at atmospheric pressure.[180] Again this is directly observed in situ in Figure 4.10, with the reduction in evaporation temperature arising due to the vapor pressure of Bi.

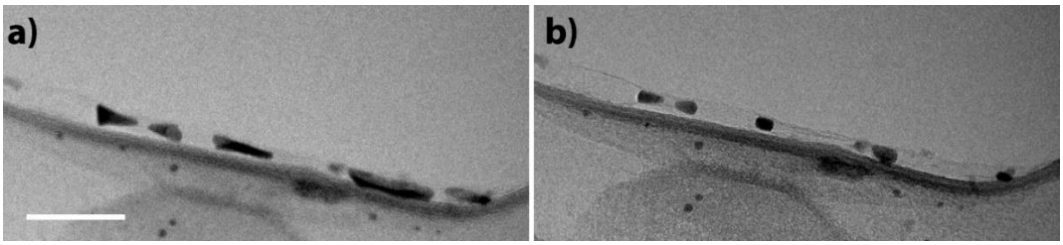

Figure 4.10: a) 35 nm liquid Bi nanowire, evaporating at 440 ºC. b) The same nanowire after 15 seconds. 250 nm scale bar.

4.4 Conclusion

The effects of heating a material under high vacuum have been explored to highlight how phase transitions may be misinterpreted, leading to incorrect reports of a reduction in melting temperature.[148, 153-154] This Chapter investigated the effects of heating SCFED grown single crystal Te nanowires under such a vacuum. Prediction of sublimation are acquired through analysis of the extended Antoine equation which predicts that for a vacuum of $\sim 5 \times 10^{-7}$ mmHg, such as present in the column of the 2100 TEM, Te should undergo sublimation at a temperature 200 °C below its melting point. Evidence that there is no liquid front creating a

liquid – gas interface was then provided in the form of confirmation of the Te crystallinity through a combination of dark field and high-resolution imaging.

The rate of sublimation is plotted, in Figure 4.4, as a function of length of nanowire sublimed against time, this highlighted a lack of correlation between the nanowire diameter and the rate of sublimation. This was expanded on by applying the observed parameters of temperature and pressure to the Hertz-Knudsen equation to generate a theoretical rate of sublimation against temperature plot. Comparisons between the theoretical and experimental rate of sublimation as a function of temperature were positive, Figure 4.5. The experimental results followed the trend of the theoretical results and matched a translation of the theoretical rate by 70 °C. This translation results in a vaporization coefficient of 2×10^{-3}. Examination of the gas flow down the remnant alumina pipeline indicated that a pressure drop of 1.5 Pa would arise over a length of 1μm. This would stop the sublimation and prevent the constant rate of sublimation that is observed, suggesting that the excess alumina pipeline contains multiple defects and escape points.

The second section of the chapter analysed SCFED grown single crystal Bi nanowires under similar conditions to the Te. The crystalline Bi nanowires were melted undergoing the solid to liquid phase transition. As the nanowire is encapsulated in a remnant alumina tube the liquid nanowire retains its appearance and there is no obvious phase change. Proof of the transition from solid to liquid arises from analysis of the SADP, in which the nanowire can be observed changing from a crystalline bright spot pattern to amorphous rings. The amorphous rings of the liquid Bi were analysed to find the average atomic spacing, this required HDR-ED SADPs that, when analysed using *RDFTools,* generated a RDF plots. With the help of the software, the average interatomic spacings were identified as 3.47, 4.92 and 6 Å and found to be the same as previously recorded data generated from XRD and Neutron diffraction. This is believed to be the first report of liquid Bi analysis, using this

technique in situ. It demonstrates the application of the process for volumes ≈1 x 10^{12} times smaller than the standard mm^3 samples for X-ray/Neutron Diffraction.

Filling of Carbon Nanotubes via the Capillary Melt or Sublimation Method

5.1 Introduction

Single-walled carbon nanotubes (SWNTs) are noted for their potential applications due to their strength and electrical properties. Examples include electrochemical devices, utilising the conductivity and natural mechanical strength of the nanotube, or hydrogen storage, exploiting the large active surface area and large internal volume of the SWNTs.[181-183] Formed through arc discharge, chemical vapor deposition and laser ablation, SWNTs form with a small range of diameters ≈ 0.5 – 6 nm.[184-188] We aim to exploit this as another form of encapsulation media for the formation of nanowires.[90]

It has been shown that some nanowires, formed within SWNTs, grow as single atomic chains.[189] This is the ultimate possible crystal structure that can be observed as a nanowire is confined within a decreasing diameter constriction. This ability to generate one-dimensional chains of atoms, including potentially binary and tertiary systems, produces profound changes to material properties with respect to the bulk crystal.[190]

This Chapter discusses the encapsulation of materials within carbon nanotubes to form nanowires with extremely small diameters. The first Section explores deposition within large diameter 1.2 – 1.75 nm SWNTs using the capillary melt filling technique. HRTEM image analysis is undertaken to understand the observed crystal matching it to a bulk-like structure. This experiment is initially undertaken using Ge as the filling material, then repeated using SbTe. Bulk Sb_2Te_3 was identified within the nanotubes and formed in both 4- and 5-atomic layer motifs, depending on SWNT diameter. The effect of electron beam

irradiation is briefly examined through analysis of an induced phase change within the encapsulated material.

The second Section examines nanowires encapsulated within smaller SWNTs with a diameter range of 0.7 – 1.2 nm. Both tellurium and tin telluride are encapsulated using the sublimation technique and observed using HRTEM and HRSTEM. Elemental characterisation was undertaken using atomic resolution EELS to analyse the purity of the samples and to identify potential contaminates. The stability of the encapsulated nanowires is examined to highlight some of the challenges faced whilst imaging the system. Theoretical structure simulations are undertaken using the AIRSS method to analyse the energy of the crystal structures with relation to the confining SWNT diameter. The density of states is calculated for the tellurium system indicating a transition from metallic to semiconducting, due to a phase transition controlled by the SWNT diameter.

5.2 Capillary Melt Filling

5.2.1 Germanium

The first case of encapsulation is the Ge system, which was encapsulated within SWNTs using the capillary melt filling technique as described in Section 2.2.2. After pre-treating the SWNTs, they were combined with 60 mg of Ge powder through a rough grinding process before being sealed under vacuum in a quartz silica ampoule. The sample was heated to 980 ^{o}C and held at this temperature for 36 hours using the heating cycle described in Table 2.1.

After heating, the ampoule showed visible results of a reaction between the inside ampoule wall and the Ge, believed to be the formation of SiGe from the Si rich ampoule. This is expected as literature reports the formation of SiGe easily in temperatures above 550 ^{o}C and as the ampoule is evacuated before heating so an oxide is less likely.[191] This reaction has not been seen in any other SWNT filling experiments under similar conditions. This is

believed to greatly affect the quantity of Ge available for filling and is reflected in the higher quantity of Ge required for filling when compared to other systems.

Bulk Ge forms in the face centred cubic (fcc) diamond structure with the $Fd\bar{3}m$ space group.[133] Image analysis with crystal simulations for the encapsulated Ge system suggest that this is also the crystal structure formed under encapsulation conditions. As Ge is tetravalent, you would expect the encapsulated and therefore most basic crystal structure to also be tetravalent as $Fd\bar{3}m$ is.

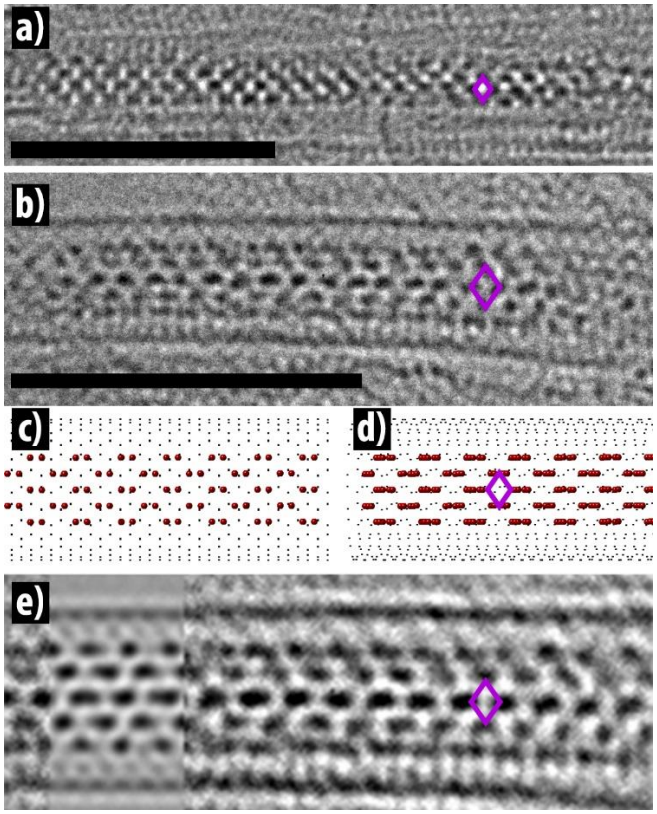

Figure 5.1: a) Encapsulated Ge within a 1.2 nm diameter SWNT. b) Encapsulated Ge nanolattice in a 1.7 nm diameter SWNT. c) Potential encapsulated bulk Ge structure manipulated to fill a SWNT with similar diameter to that in b. This is then tilted by 6º parallel to the SWNT in d). e) Simulated TEM image of the tilted encapsulated bulk structure superimposed onto the SWNT seen in b. Scale bar = 5 nm.

The Ge system appears to be stable over the SWNT diameter range, as encapsulation within both the 1.2 nm and 1.75 nm exhibits the same structure, as shown in Figure 5.1 a and b respectively. Lattice blurring is observed parallel to the SWNT orientation. This suggests that the SWNT is tilted, as the blurring arises when a lattice is off axis, with the contrast generated from overlapping atomic columns.

The Ge system was simulated by extracting a region from the diamond fcc Ge lattice equal to the volume inside the SWNT. A SWNT with a diameter equal to that of the experimental image is then generated and stuffed with said extracted volume, Figure 5.1 c. A virtual TEM was set up in SimulaTEM, with simulation parameters equal to those observed during experimentation in the microscope i.e. C_3=0.001 mm and an acceleration voltage of 80 Kv.[192] It is shown that the structure simulated, as seen in Figure 5.1 d, tilted by 6º, parallel to the direction of the nanotube, is enough to generate the central spot elongation and match up the structure with a high amount of accuracy. Examination of the diffraction pattern from the theoretical structure suggests the Ge is forming along the [100] axis, this is reinforced by the formation of a repeating diamond shaped motif highlighted throughout Figure 5.1.

We believe this to be the first experimental encapsulation of crystalline Ge within SWNTs at such an extreme diameter range. This is suggested from the previous work published by Zhang[193] being related to theoretical filling and the experimental filling observed by Cui[194] was both amorphous and on a much larger scale. The formation of crystalline Ge within these confinements suggest that the SCFED of Ge may become crystalline if deposition was successfully achieved within a sub 2 nm confinement.

5.2.2 Antimony Telluride

For comparisons to the Ge and of interest due to its known phase change properties, Antimony Telluride was encapsulated, again, within SWNTs using the capillary melt filling

technique. The ground and combined Sb_2Te_3/SWNT were sealed under vacuum in a silica quartz ampoule with a mass ratio of 30/9 mg respectively. It was heated using the cycle described in Table 2.1 at a maximum temperature of 620 ºC for a total of 45 hours. Unlike the Ge system, no reaction with the ampoule was observed.

Encapsulated Sb_2Te_3 forms as its bulk counterpart, with the crystals observed in Figure 5.2 being bulk Sb_2Te_3 forming in the R-3mh space group.[195] The SWNTs again had a diameter distribution which affects the amount of space available when the Sb_2Te_3 is formed. The result of this is the observation of both 4 layer and 5 layer thick motifs of encapsulated Sb_2Te_3 nanowires, Figure 5.2 a-d.

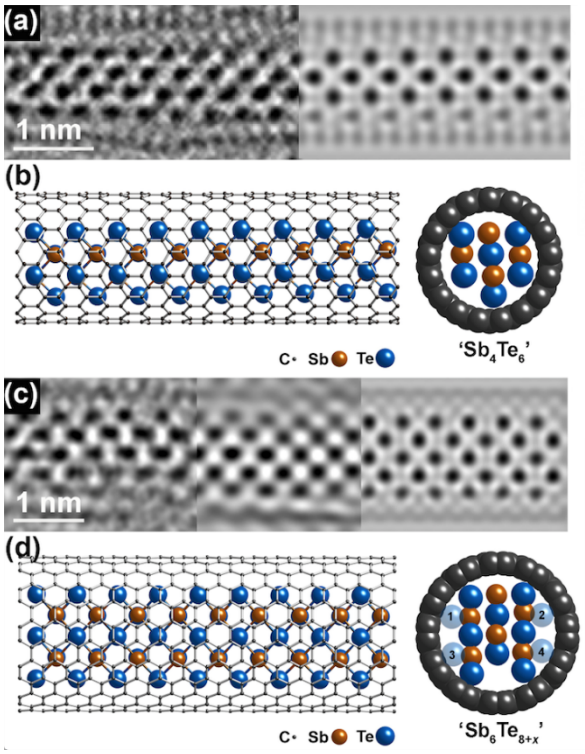

Figure 5.2: a) TEM image (left) and simulated image (right) for a 4 – atomic layer thick Sb_2Te_3 nanowire within a 1.35 nm SWNT. b) Simulated 4 – atomic layer thick structural model of the nanowire based on bulk Sb_2Te_3. c) TEM image followed by a Wien filtered image and then superimposed with (d) the 5 – atomic layer simulated structure for a Sb_2Te_2 Nanowire within a 1.62 nm SWNT. d) Simulated 5 – atomic layer thick structural model.

It was found that a crystalline to amorphous phase change could be induced in situ by irradiating the Sb_2Te_3 nanowires using the electron beam. This was characterised using

SADP taken before and after condensed electron beam irradiation. A beam current of 1.5 pA cm^{-2} was strong enough to initiate the transition with a complete phase change observed within 5 minutes. This is identified from the observed change in the SADP in which the crystalline Sb_2Te_3 spots become diffuse. A beam current of 0.8 pA cm^{-2} was used during the original image acquisition in Figure 5.3 a, suggesting the threshold transitional current lies between 0.8 and 1.5 pA cm^{-2}.

This reports the first encapsulation of crystalline Sb_2Te_3 within SWNTs. The crystal structure was investigated through high-resolution aberration corrected TEM imaging. The quality of the data obtained allowed for crystal determination and simulation with a high amount of accuracy. The direct phase transition from crystalline to amorphous was observed under electron beam irradiation, and shown to occur between the energy range of 0.8 and 1.5 pA cm^{-2} at an accelerating voltage of 80 kV.

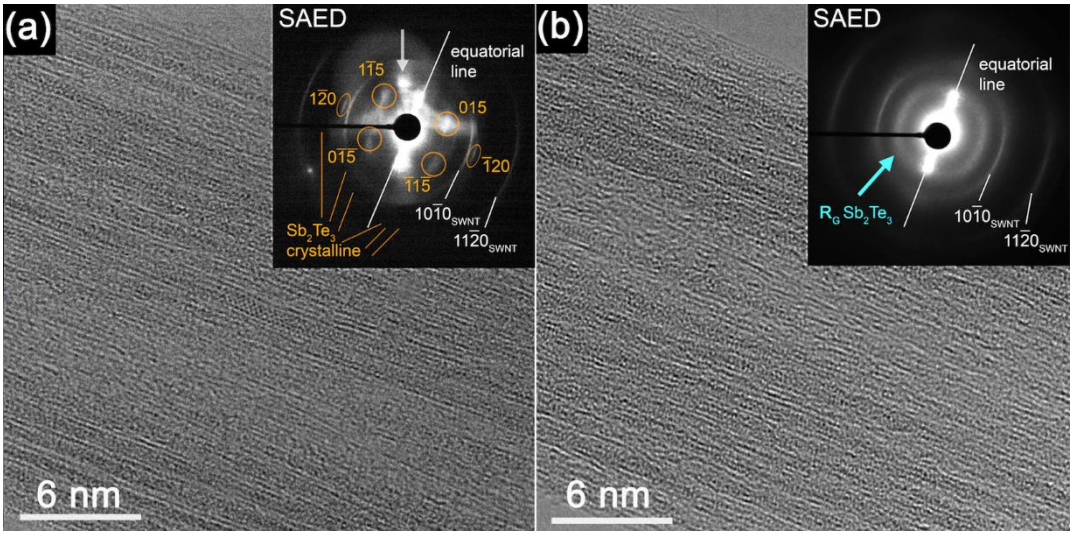

Figure 5.3: a) TEM image of bundled Sb_2Te_3 filled SWNT with inset SADP from the featured bundle. Bright spot reflections are observed within both the SADP and TEM image, evidence for crystalline filling. b) The same bundle after 5 minutes of 1.5 pA cm^{-2} electron beam irradiation. Evidence of the samples crystallinity has been removed from both the SADP and TEM image, with a diffuse ring labelled R_G indicating an amorphous structure.

5.3 Sublimation Filling

It was found that the capillary melt filling method produced a high amount of contamination in the form of remnant bulk material, especially catalysis particles, agglomerating on the outside of the SWNTs. It was also challenging to generate a high filling fraction using this technique, possibly arising from the filled material being drawn out of the SWNTs during cooling/annealing due to the connection with remnant bulk particles. Therefore, the sublimation technique was adopted to remove contamination and increase the filling percentage. This technique was applied to two new systems for investigation.

5.3.1 Tellurium

Tellurium was encapsulated within SWeNT SWNTs using the sublimation filling technique detailed in Section 2.2.3. The sublimation filling technique was used as it had shown promise in generating less contaminated samples with higher filling fractions due to the increase in gas mobility and penetration over liquid melts. The source of SWNTs was shifted to SWeNT as they could provide SWNTs with both smaller diameters and a smaller diameter distribution. 100 mg of powdered Te was loaded into a sublimation ampoule with 60 mg of SWNTs loaded into the opposite end, before being sealed under vacuum. The sample was heated at 425 ºC for 6 days. After heating, confirmation of Te mass transport was observed by new crystallites forming around the SWNTs and a complete reduction of the original Te powder.

The Te chains observed within the SWNTs were predominantly helical coils, Figure 5.4, formed from a 3-fold-symmetric screw axis. The experimental results suggest that the compression on each coil, and therefore the periodicity of the Te is non-monotonic with respect to the nanowire diameter, highlighted in Figure 5.4. Single Te atomic chains were observed in the smallest diameter SWNTs, indicating that the threshold for truly one-dimensional crystals lies with a nanotube diameter between 0.855 and 0.749 nm. The exact

encapsulated structure is hard to define from TEM images due to the rotation of each individual helix and the energy transfer from the electron beam.

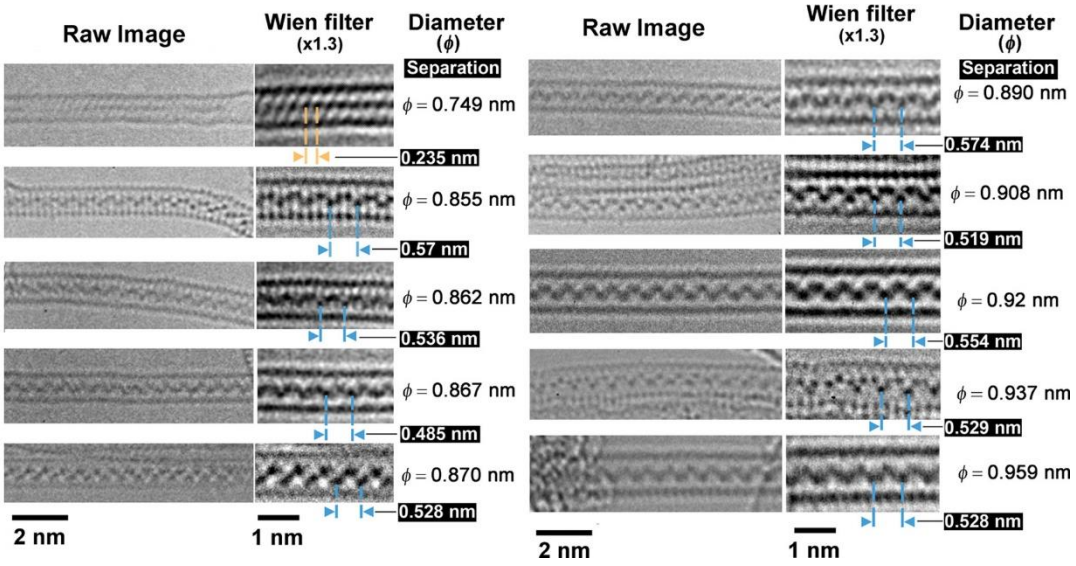

Figure 5.4: TEM images of encapsulated Te nanowires within SWNTs (sorted by diameter). A single linear Te chain is observed inside a 0.749 nm SWNT with helical coil like structure observed throughout the others. The periodicity of each chain is indicated and was acquired from the Wien filtered images for each system.

The SWNTs are imaged using an 80 kV accelerating voltage, as this has shown to be below the knock on damage threshold for graphitised carbon of 86 kV.[196] The SWNTs are not damaged by the electron beam but there is considerable energy transfer to the encapsulated nanowires. This is observed through the movement of Te atoms, somewhat freely, within the SWNTs.

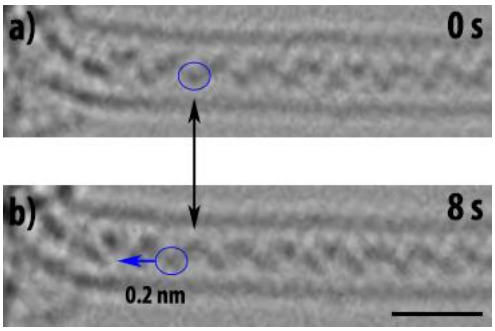

Figure 5.5: a) Initiation of a Te coil shift due to electron beam irradiation. b) The same coil 8 seconds later. The reference atom in a) has been displaced by 0.2 nm to form a minor compression at the SWNT corner (far left). Scale bar = 1 nm

An example of encapsulated Te movement is shown in Figure 5.5 highlighting the translation of a Te coil inside the SWNT to form a coil compression. It has been suggested that the amount of energy transferred may be decreased by using an in situ cooling holder. However, this would be challenging due to the resolution loss induced by the cooling holder generating high amounts of sample drift.

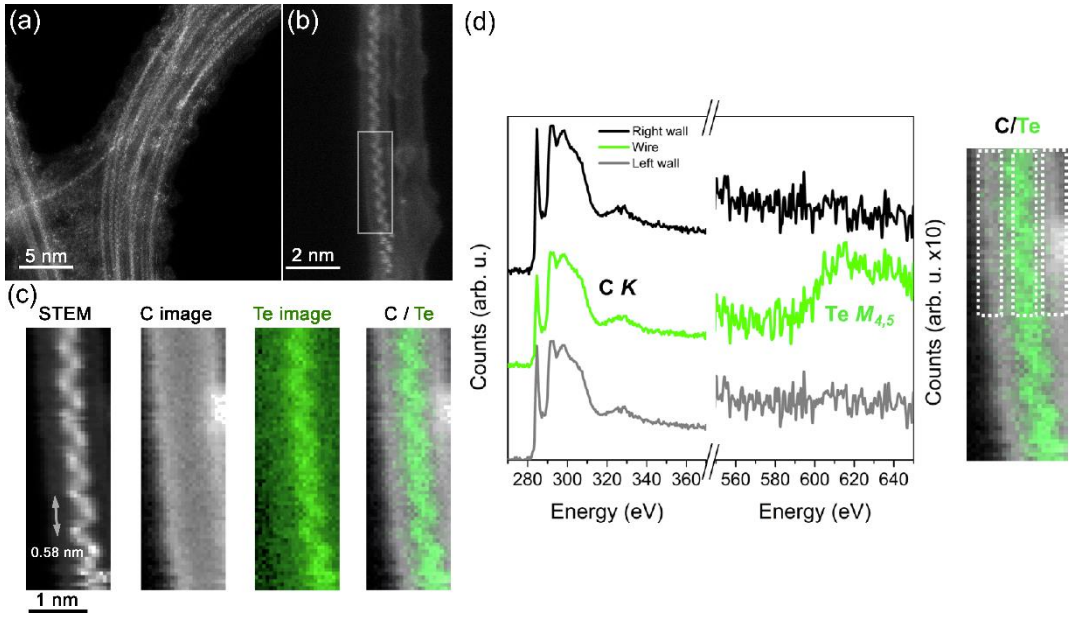

Figure 5.6: a) ADF STEM image showing a high filling percentage and large difference in Z contrast between the C and Te. b) Higher magnification image of a single helical coil Te nanowire. The box indicates the spectrum image region of c and the source of the EELS analysis in d. c) STEM ADF image, C, Te and a composite C/Te spectrum images. d) Extracted EELS spectra from the regions indicated by the dashed boxes in the composite C/Te image. The C K edge and Te M 4,5 edge EELS spectra indicated pure Te within the SWNT with no Te signal observed within the SWNT walls. (STEM imaging, EELS and EELS mapping by Q. Ramasse, STFC SuperSTEM)

A high filling fraction was seen throughout the sample observed from the Z contrast between the C and Te in STEM imaging, Figure 5.6 a. EELS analysis combined with STEM imaging confirmed the chemical identity as elemental Te with no O seen in the spectra. The resolution of the spectrum imaging allows for reconstruction of the C and Te images from the spectrum.

Analysis of the EELS spectra from the bounding C regions and internal Te nanowire region suggests elemental Te. Examination of the extracted C spectra show increased Pi bonding, the first peak in the C spectra, as expected when looking perpendicularly through the SWNT but no chemical shifts or changes in shape. This suggests that the C has no local interaction with the Te, reinforcing the observations of free Te movement under electron beam irradiation. EDX analysis was unobtainable from the individual Te coils as the X-ray count was too low. A strong Te peak was observed for bundles of filled SWNTs, however. this may include large crystallite contaminants, observed across the sample, and has therefore been omitted here.

In an attempt to determine the crystal structure from a more robust approach the AIRSS method was adapted to model the encapsulated Te.[98] This was undertaken by Paulo Medieros and Andrew Morris at the University of Cambridge using the methods detailed in section 2.4.5. The use of a confining potential, equivalent to the Van der Waals interaction seen by the encapsulated Te, as a parameter for the AIRSS search allowed for extensive structure searches. The most energetically favourable structures, predominantly helix based, are shown in Figure 5.7. Analysis of the resulting structures with relation to their energies and the SWNT diameter suggest several predictions, as follows.

Te encapsulation within a SWNT with a diameter < 0.77 nm will always form in a linear chain as the most energetically favourable orientation. Above 0.77 nm the lowest energy structure is a zigzag structure, superseded by the 3-atom helix (3H) orientation above 0.86 nm.[197] The 3H structure is 3-atom helix similar to a helix seen within bulk Te, but with a wider unit cell. The energy profiles suggest, for the nominal diameter distribution of SWeNT SWNTs, that the 3H structure should be the dominant structure, which it is.

It was also found that for SWNTS with a diameter ≈ 1.1 nm a defective 3H structure becomes energetically most favourable. This defective structure derives from a combination

of two helices from 3H but one with a left-hand screw and the other a right-hand screw. As a defective 3H structure can be energetically favourable this suggests that atomic displacements due to electron beam irradiation could lead to the formation of new stable orientations away from the natural forming structures.

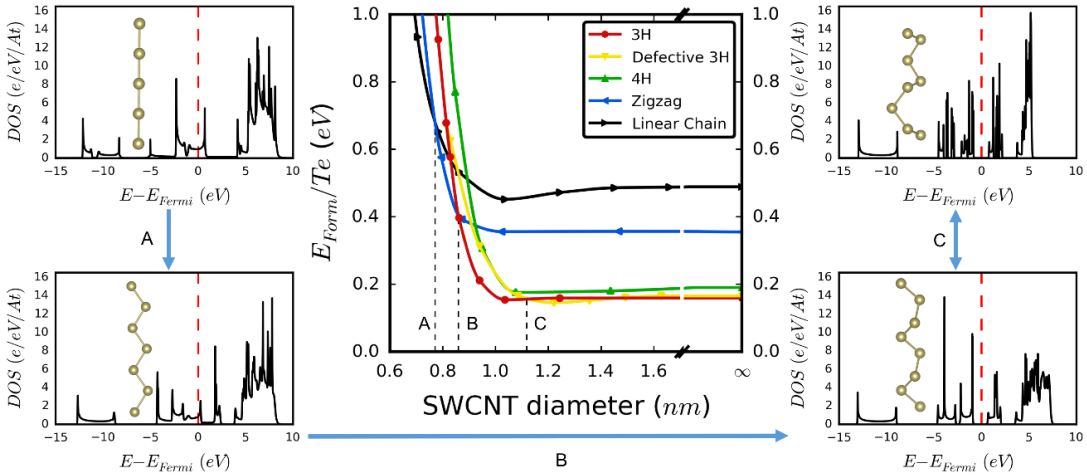

Figure 5.7: Examination of the competing encapsulated Te nanowires as predicted by AIRSS. Central panel: Formation energy per encapsulated atom as a function of SWNT diameter. The labels A – C indicate transitions in the energetically favourable structure. Surrounding panels: Visualisation of each structure including their calculated density of state (DOS). Labelled arrows indicate the structural transitions. (Encapsulation energies and DOS calculations by P. Medeiros)

The electronic densities of states were calculated for each Te structure, Figure 5.7. The interaction between the encapsulated Te and the SWNTs, particularly the SWNTs influence on the Te electronic structure, is believed to be small or negligible. Inspection of the density of state plots suggest that upon undergoing the structural transition from zigzag to 3H (transition B) the Te also transitions from metallic to semiconducting.

Thus, it is expected that encapsulated Te will form in its bulk like helical structure until confined within a sub 0.86 nm diameter SWNT. Below this it forms a new zigzag structure before transitioning to a truly one dimensional atomic chain structure below 0.77 nm. The densities of states also suggest that upon making the transition from bulk-like Te the system also transitions from semiconducting to metallic. The theoretical structures,

generated using the AIRSS method, show a high degree of correlation with the experimental structures. As predicted a linear chain is observed in a 0.749 nm SWNT and the 3H structure is observed in throughout the 0.855 - 0.959 nm SWNT diameter range. It is believed that the variation in periodicity arises from the atomic relaxations occurring as a function of diameter. This positive comparison suggests that the AIRSS method can be used effectively to model such systems in the future.

5.3.2 Tin Telluride

The final system studied here is SnTe sublimed into SWeNT SWNTs. This was undertaken in attempts to form a more complex encapsulated nanowire using the sublimation method. 70 mg of SnTe was loaded into a silica quartz sublimation ampoule opposite to 10 mg of SWeNT SWNTs. Once sealed under vacuum the region of the ampoule containing the SnTe was baked at 760 ºC for 7 days. Visual confirmation of mass transport was observed through the growth of crystallites in the colder SWNT end of the sublimation ampoule.

STEM images indicate a high degree of filling, clearly visible from the high Z contrast of the SnTe in comparison to the C in the ADF images, Figure 5.8. Some excess material was seen on the surface of the SWNTs as well as some filled SWNTs with a diameter greater than expected. Throughout the sample two dominant structures were observed, akin to the filled Te system, with a helix and a one-dimensional chain prevailing throughout. SnTe naturally forms in a face centred cubic $Fm\bar{3}m$ crystal structure with simple overlapping Sn and Te fcc structures.[198] As this structure is cubic most of the crystallographic orientations from the bulk would satisfy a linear chain condition. No combined SnTe or isolated Sn/Te column helix arrangements arise within the bulk crystal suggesting that this may be a new phase.

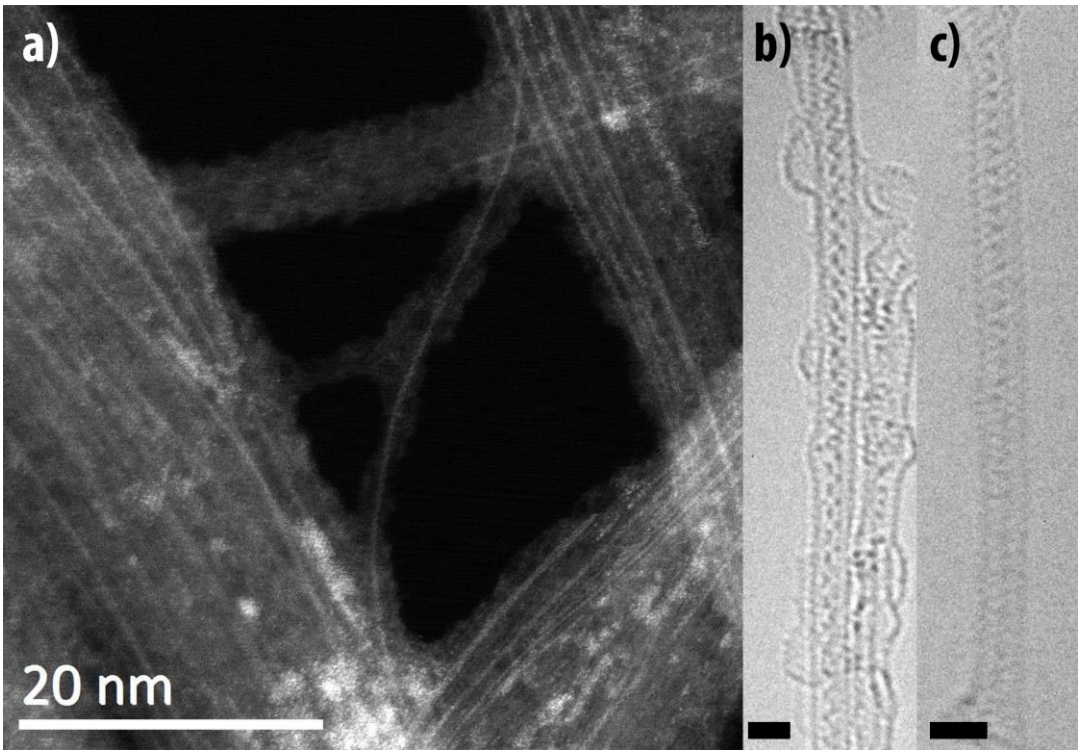

Figure 5.8 a) STEM ADF image of SnTe filled SWNTs, a high degree of filling is observed with some contaminant/bulk-like material also visible. b-c) Helical and one-dimensional chain SnTe structures seen throughout the sample as the two dominant orientations. Inset 1 nm scale bar

EELS was performed on the samples to understand the structures observed. Representative data was taken from the two prominent systems of both the helical and one-dimensional chain. The EELS data was acquired whilst capturing live video of the samples to correct for drift in real time. Analysis of the EELS spectra confirms the identity of the helical chain as SnTe, though it does not provide quantitative information on the elemental ratio. Analysis of the one-dimensional chain shows a clear Sn edge, onset at 485 eV, but instead of a Te peak onset at 572 eV, there is an edge onset at ≈ 620 eV. This suggest either a 50 eV chemical shift or that the element being identified is Iodine, which has a strong $M_{4,5}$ edge at 619 eV, making the one-dimensional chains SnI. No I should be present within the sample and it is believed that this is a contaminant from a previous experiment. The Sn M_3 edge onset can be seen as expected at ≈ 720 eV in both spectra indicating that the energy calibration is correct for both of them.

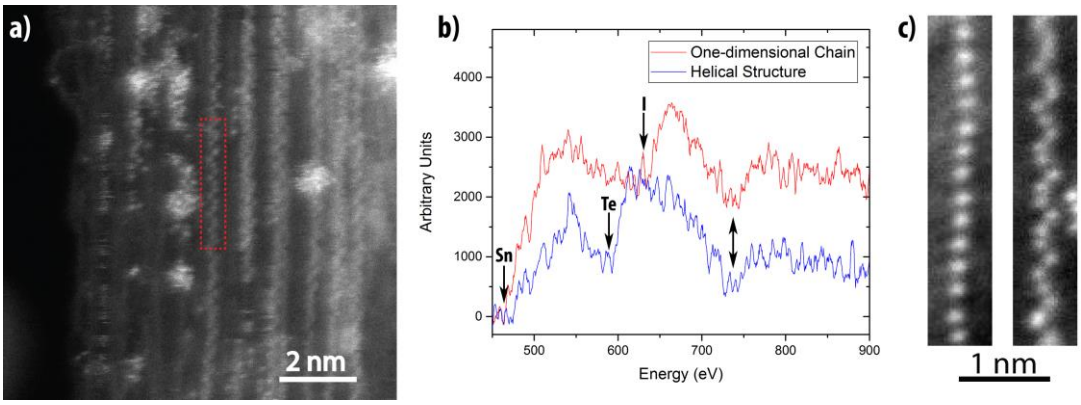

Figure 5.9 a) STEM ADF image of SnTe filled SWNTS, an overlay highlights a typical survey region used during EELS acquisition. b) Smoothed EELS spectra for the one-dimension and helical encapsulation structures. The approximate onset energies for Sn, Te and I are indicated to highlight the change in EELS spectra across the two structures. The Sn M_3 onset can be seen at ≈ 720 eV in both samples. c) Summed stack of STEM ADF images for both a one-dimensional and helical crystal. (STEM imaging, EELS and EELS mapping by Q. Ramasse, STFC SuperSTEM)

Simulations of the encapsulated structures were performed using the AIRSS method. The potential for formation of non-stoichiometric crystal structures with different ratios of Sn and Te is high due to incongruent sublimation. The possible difference in stoichiometry removes any ability to compare different structures purely through their potential energy. Therefore, potential structures are compared with respect to their per atom formulation energy, defined in Section 2.4.5. A plot of the formation energy against concentration of Te is shown in Figure 5.10 a. Here a comparison between the formation energy for bulk and gaseous Te within SWNTs with two diameters, 4.06 and 6.78 Å, is plotted against the percentage composition of Te. The difference in formation energy between gaseous and solid Te indicates that formation will only occur once sublimed into the gaseous medium as the formation energy must be negative. The energy minimum indicates that the optimum stoichiometry is 1:1 SnTe.

From this criteria the AIRSS method was implemented to search for potential encapsulated structures of stoichiometric SnTe (performed by Andrij Vasylenko at the University of Warwick). Once identified, the formation energy of the potential structures

were plotted as a function of SWNT diameter. This indicated several dominant crystal structures arising as a function of SWNT diameter, Figure 5.10 b, with the prevailing structure in the SWeNT diameter range being a double zigzag. This matches the experimental results reported above as the dominant structure appeared to be some form of helix structure. It is believed that the helixes observed are the double zigzag structure as highlighted in Figure 5.10 c, with the overlapping zigzags being the source of lattice blurring in the acquired experimental images.

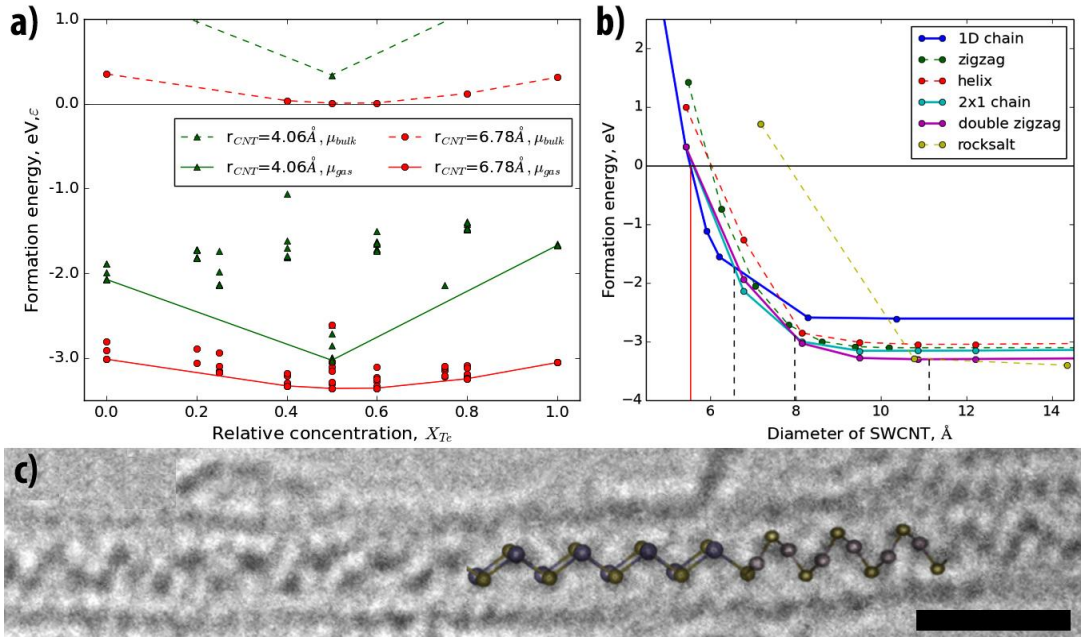

Figure 5.10 a) Plot of the formation energy of SnTe nanowires for different relative concentrations of Te embedded within two different diameter SWNTs. Included is the formation energy of solid Te. b) Formation energy as a function of SWNT diameter for encapsulated SnTe nanowires. The dashed black lines indicate the transitions in dominant crystal structures with the red line being the minimum SWNT diameter. c) HRTEM image of encapsulated SnTe nanowire overlaid with the predicted double zigzag (left) transitioning into a helical chain (right). Scale bar = 1 nm. (formation energy modelled by A. Vasylenko)

In summary, the successful filling of SnTe within SWNTs has been observed across a diameter range of 0.8 – 1.1 nm. A formation energy against relative concentration plot was used to confirm that the formation must arise for a gaseous medium and identified a natural affinity towards a stoichiometric 1:1 ratio of Sn and Te. This aided in refining an AIRSS method theoretical structure search to locate crystal structures and map them by their

formation energy. The suggested theoretical structures appear to map to experimental images with good agreement.

5.4 Conclusion

There can be no smaller nanowire than a one-dimensional chain of atoms. This can be experimentally created through the manipulation of material encapsulation within carbon nanotubes. This Chapter described four different systems of nanowires grown within two different diameter nanotubes exploring the relationships between: nanotube diameter, crystal structure, electron beam irradiation, theoretical modelling and the challenges of elemental characterisation.

The first case reports Ge encapsulation within NI SWNTs with a diameter range of 1.2 – 1.75 nm using the melt filling technique. Here the crystal structure was determined through visual comparison and measurements of the observed atomic spacings in the high-resolution images. It was found that the Ge forms within the bulk $Fd\bar{3}m$ crystal structure. This is believed to be the first experimental case of crystalline Ge encapsulation within SWNTs as previous published work resulted in amorphous nanowires.

Antimony Telluride was also encapsulated within NI SWNTs using the melt filling technique. It was found that the Sb_2Te_3 formed as its bulk counterpart and due to the SWNT diameter distribution both 4 layer and 5 layer Sb_2Te_3 nanowires were observed. The effects of electron beam irradiation were examined through the analysis of pre- and post-irradiation SADP. This indicated a phase change from solid to amorphous suggesting that the threshold beam current lies between 0.8 and 1.5 pA cm^{-2}.

The third encapsulation study involved Te confinement within narrower SWNTs, with a diameter 0.7 – 1.1 nm, using the sublimation technique. Imaging of the sample showed two prevalent structures: a one-dimensional chain and a helical coil, with the helical coil similar to bulk Te. An EELS study of the sample confirmed the filling composition to be

elemental Te with spectral imaging allowing for a reconstruction of the coil from the Te signal. The effects of electron beam irradiation were more apparent within the smaller diameter SWNTs and easily visualised through the mobility of the encapsulated atoms. It is believed that this mobility may be reduced through the application of a cooling holder however this would induce drift and possibly affect the image quality. The encapsulated structure was simulated from first principles using the AIRSS method. This relied on the encapsulation volume, generated from the Van der Waals surface of the carbon nanotube, and not the experimental results. This indicated three dominant structures, depending on nanotube diameter: a one-dimensional chain, a helix and a defective helix. The theoretical results showed a high degree of correlation to the experimental results including mapping the SWNT diameter where the structural transitions should occur.

The final system investigated was the SnTe system, again encapsulated within the 0.7 – 1.1 nm diameter SWNTs. Examination of the filled SWNTs highlighted two prominent structures across the sample, similar to the Te system, consisting of a one-dimensional chain and a helical structure. Of the two structures, the one-dimensional chain is more akin to bulk $Fm\bar{3}m$ SnTe with no helix orientations present. EELS analysis of the samples reinforced the two dominant structures and allowed for chemical analysis of them. This confirmed the helical structure as SnTe but suggested that the one-dimensional chain had a composition of SnI. The contaminating I is believed to have entered the system from a previous experiment.

Simulations of the encapsulated structures were undertaken using the AIRSS method after examining the potential stoichiometry of the sample. The confirmed stoichiometry of 1:1, Sn Te, helped refine the potential SnTe structures and allowed for mapping the lowest energy, most likely crystal structure as a function of SWNT diameter. The predicted structure, for the nominal SWNT diameter, was a double zigzag. A variation of the helical structure observed.

Conclusions and Future Work

This thesis aimed to identify electron microscopy as the primary characterisation technique for analysing samples formed by both SCFED and CNT encapsulation. The versatility of electron microscopy is explored through a combination of systems: general characterisation including EDX analysis and SADP, in situ heating with high-resolution video recording and RDF, and STEM imaging with EELS. The ability to undertake such a vast range of analysis underpins and confirms this hypothesis.

Chapter 3 demonstrated the need for electron microscopy with respect to the analysis of samples formed using the experimental SCFED method. Ge films were shown to be protocrystalline with SADP visualising XRD and Raman results. DF imaging allowed for visualisation of Ge crystallites embedded within an amorphous Ge film. This led to the successful SCFED of Ge, CuTe, CuTeS and Sn into AAO pores. SADP of the polycrystalline CuTe system combined with RDF allowed for the identification of the P4/nmm tetragonal space group from comparisons to the bulk kinematic diffraction intensities. SADP was then utilised to identify the Cu_6Te_3S as the deposited structure from 4 potential options. A new AAO hierarchical template was introduced for SCFED of Sn. With successful SCFED achieved within sub 10 nm pores with a 6.3 nm nanowire compression observed.

Though the advantages of using electron microscopy to characterise SCFED samples is indisputable, improvements can still be made progressing forward with the analysis. Annealing increased the crystallinity of the Ge films. Therefore, by replicating this in situ, using a heating stage, it is expected that real time annealing could be performed and dynamically observed. With respect to identifying the crystallographic CuTeS structure, the inclusion of atomic resolution EDX, though very challenging, would provide indisputable evidence for the elemental distribution across the lattice and would complement the current work.

In Chapter 4, the phase transition of encapsulation nanowires is examined in situ for Bi and Te. With respect to Te, the UHV conditions within the microscope altered the phase transition causing sublimation. This was caused by a combination of the Te vapor pressure compared to the UHV of the microscope and the temperature of the system. Calculations proved the sublimation to be Langmuir-type and the process was successfully described by the Hertz-Knudsen equation rendering an evaporation coefficient of 2×10^{-3}.

The continuous rate of sublimation shows that the excess alumina template must be non-continuous, as no pressure drop is observed. Additionally, combining the rate of sublimation with EDX indicates that small quantities of contaminants are transported along the nanowire during the sublimation process sitting on the sublimation front to be deposited at the end of the sublimation process. SADP of the Bi phase transition proves a phase transition from solid to liquid. Finally, RDF analysis, with optimisation of the RDFTools plugin, generated a first peak at 3.47 Å, this is comparable to results obtained through XRD and neutron diffraction. However, XRD and neutron scattering would have little signal at the nanometre scales involved here.

To expand on the heating and sublimation experiments, the primary deficiency involved was the accuracy of both the temperature and vacuum measurements at the sample. The upgrade to a MEMS based heating holder would increase the accuracy of the temperature measurements, as the thermocouple is incorporated onto the heating mechanism at the sample. This also bolsters the stability of the holder. The accuracy of the vacuum measurement must also be explored, this could be improved by the positioning of a vacuum gauge closer to the sample. Several variations of in situ heating sample holders are now available, allowing for a second variable to be measured, for example electrical biasing or a liquid atmosphere. The addition of sample biasing would be favourable, as this would allow for the measurement of electrical properties of the nanowire, before, during and after heating.

The final chapter presents attempts to make one-dimensional crystals through the encapsulations of materials within CNTs. As a way to establish procedure, traditional capillary melt filling was assessed with the encapsulation of Ge and SbTe. The procedure was successful, resulted in bulk crystals with 3 – 4 atom thick motifs. The instability of the encapsulated crystals was observed in situ through electron beam amorphisation of SbTe. The low-filling fraction and amount of surface contamination across the sample was identified as the limiting factors of the capillary method. To compensate for this, sublimation filling and smaller diameter SWNTS were investigated.

Smaller degrees of encapsulation were observed for both Te and SnTe, including one-dimensional crystals. This was a result of both the implementation of the sublimation procedure and a change in SWNT suppliers. Visual investigation from HRTEM and HRSTEM proved challenging, with more fundamental crystal structures arising. Therefore, the application of AIRSS as a structure determination technique was essential to effectively identify all of the observed structures. The transitions through these structures as a function of SWNT confining diameter is easily explained, using AIRSS, with respect to the formation energy of the structure.

Expanding on this research to form complex materials, comprised of multiple elements, is of great interest. As the underlying physics of atomic interactions at the truly one-dimensional scale are scarcely probed. This is also the natural next step for the AIRSS, as the introduction of multiple elements require more complex searches. In terms of application, the ability to form functional devices from the filled CNTS is highly desirable, due to the noted change in elemental properties at small size ranges (< 3nm). This could be achieved by distributing the filled CNTs from suspension onto bucky paper in a process similar to the redistribution process for Ni96 CNTs.

Encapsulated nanowires have shown promising potential as next generation devices.[199-201] Continued study of different encapsulated materials, including different forms of encapsulation, with respect to the profound changes in physical properties at the nanoscale will be essential. As the interest in smaller devices and materials increases, it is electron microscopy that will provide the most accurate visualization technique. The combination of this with in situ experimentation, will be key as this trend continues, making electron microscopy an invaluable tool.

Bibliography

(1.) Schaller, R. R. "Moore's Law: Past, Present and Future." *IEEE Spectrum* **1997,** *34*, 52-59.

(2.) Moore, G. E. "Cramming More Components onto Integrated Circuits." *Proceedings of the IEEE* **1998,** *86*, 82-85.

(3.) Shin, J. L.; Huang, D.; Petrick, B.; Hwang, C.; Tam, K. W.; Smith, A.; Pham, H.; Li, H.; Johnson, T.; Schumacher, F.; Leon, A. S.; Strong, A. "A 40 Nm 16-Core 128-Thread Sparc Soc Processor." *IEEE Journal of Solid-State Circuits* **2011,** *46*, 131-144.

(4.) Kaneko, A.; Yagishita, A.; Yahashi, K.; Kubota, T.; Omura, M.; Matsuo, K.; Mizushima, I.; Okano, K.; Kawasaki, H.; Inaba, S.; Izumida, T.; Kanemura, T.; Aoki, N.; Ishimaru, K.; Ishiuchi, H.; Suguro, K.; Eguchi, K.; Tsunashima, Y. "In Sidewall Transfer Process and Selective Gate Sidewall Spacer Formation Technology for Sub-15nm Finfet with Elevated Source/Drain Extension, "*IEEE InternationalElectron Devices Meeting*, 2005. IEDM Technical Digest., 5-5 Dec. 2005; 2005; pp 844-847.

(5.) Markov, I. L. "Limits on Fundamental Limits to Computation." *Nature* **2014,** *512*, 147-154.

(6.) O'Dwyer, C.; Szachowicz, M.; Visimberga, G.; Lavayen, V.; Newcomb, S. B.; Torres, C. M. "Bottom-up Growth of Fully Transparent Contact Layers of Indium Tin Oxide Nanowires for Light-Emitting Devices." *Nat Nanotechnol* **2009,** *4*, 239-44.

(7.) Britnell, L.; Ribeiro, R. M.; Eckmann, A.; Jalil, R.; Belle, B. D.; Mishchenko, A.; Kim, Y.-J.; Gorbachev, R. V.; Georgiou, T.; Morozov, S. V.; Grigorenko, A. N.; Geim, A. K.; Casiraghi, C.; Neto, A. H. C.; Novoselov, K. S. "Strong Light-Matter Interactions in Heterostructures of Atomically Thin Films." *Science* **2013,** *340*, 1311-1314.

(8.) Novoselov, K. S.; Geim, A. K.; Morozov, S. V.; Jiang, D.; Katsnelson, M. I.; Grigorieva, I. V.; Dubonos, S. V.; Firsov, A. A. "Two-Dimensional Gas of Massless Dirac Fermions in Graphene." *Nature* **2005,** *438*, 197-200.

(9.) Wagner, R. S.; Ellis, W. C. "Vapor-Liquid-Solid Mechanism of Single Crystal Growth." *App. Phys. Lett.* **1964,** *4*, 89-90.

(10.) Schönenberger, C.; van der Zande, B. M. I.; Fokkink, L. G. J.; Henny, M.; Schmid, C.; Krüger, M.; Bachtold, A.; Huber, R.; Birk, H.; Staufer, U. "Template Synthesis of Nanowires in Porous Polycarbonate Membranes: Electrochemistry and Morphology." *The Journal of Physical Chemistry B* **1997,** *101*, 5497-5505.

(11.) Kodambaka, S.; Tersoff, J.; Reuter, M. C.; Ross, F. M. "Diameter-Independent Kinetics in the Vapor-Liquid-Solid Growth of Si Nanowires." *Physical Review Letters* **2006,** *96*, 096105.

(12.) Li, S. Y.; Lee, C. Y.; Tseng, T. Y. "Copper-Catalyzed Zno Nanowires on Silicon (1 0 0) Grown by Vapor–Liquid–Solid Process." *J. Cry. Gro.* **2003,** *247*, 357-362.

(13.) Sung-Jin, W.; Sungjoo, L.; Dong-Zhi, C.; Wei-Feng, Y.; Byung-Jin, C.; Yun-Fook, L.; Dim-Lee, K. "B-Doping of Vapour–Liquid–Solid Grown Au-Catalysed and Al-Catalysed Si Nanowires: Effects of B 2 H 6 Gas During Si Nanowire Growth and B-Doping by a Post-Synthesis in Situ Plasma Process." *Nanotechnology* **2007,** *18*, 275302.

(14.) Martelli, F.; Rubini, S.; Piccin, M.; Bais, G.; Jabeen, F.; De Franceschi, S.; Grillo, V.; Carlino, E.; D'Acapito, F.; Boscherini, F.; Cabrini, S.; Lazzarino, M.; Businaro, L.;

Romanato, F.; Franciosi, A. "Manganese-Induced Growth of Gaas Nanowires." *Nano Letters* **2006,** *6*, 2130-2134.
(15.) Perea, D. E.; Li, N.; Dickerson, R. M.; Misra, A.; Picraux, S. T. "Controlling Heterojunction Abruptness in Vls-Grown Semiconductor Nanowires Via in Situ Catalyst Alloying." *Nano Letters* **2011,** *11*, 3117-3122.
(16.) Adachi, M. M.; Anantram, M. P.; Karim, K. S. "Core-Shell Silicon Nanowire Solar Cells." *Scientific Reports* **2013,** *3*, 1546.
(17.) Keilbach, A.; Moses, J.; Köhn, R.; Döblinger, M.; Bein, T. "Electrodeposition of Copper and Silver Nanowires in Hierarchical Mesoporous Silica/Anodic Alumina Nanostructures." *Chemistry of Materials* **2010,** *22*, 5430-5436.
(18.) Jeske, M.; Schultze, J. W.; Thönissen, M.; Münder, H. "Electrodeposition of Metals into Porous Silicon." *Thin Solid Films* **1995,** *255*, 63-66.
(19.) Yin, A. J.; Li, J.; Jian, W.; Bennett, A. J.; Xu, J. M. "Fabrication of Highly Ordered Metallic Nanowire Arrays by Electrodeposition." *App. Phys. Lett.* **2001,** *79*, 1039-1041.
(20.) Arefpour, M.; Kashi, M. A.; Ramazani, A.; Montazer, A. H. "Electrochemical Pore Filling Strategy for Controlled Growth of Magnetic and Metallic Nanowire Arrays with Large Area Uniformity." *Nanotechnology* **2016,** *27*, 275605.
(21.) Tuan, H.-Y.; Lee, D. C.; Hanrath, T.; Korgel, B. A. "Catalytic Solid-Phase Seeding of Silicon Nanowires by Nickel Nanocrystals in Organic Solvents." *Nano Letters* **2005,** *5*, 681-684.
(22.) Ye, H.; Lu, P.; Yu, Z.; Song, Y.; Wang, D.; Wang, S. "Critical Thickness and Radius for Axial Heterostructure Nanowires Using Finite-Element Method." *Nano Letters* **2009,** *9*, 1921-1925.
(23.) Lauhon, L. J.; Gudiksen, M. S.; Wang, D.; Lieber, C. M. "Epitaxial Core-Shell and Core-Multishell Nanowire Heterostructures." *Nature* **2002,** *420*, 57-61.
(24.) Duan, X.; Lieber, C. M. "Laser-Assisted Catalytic Growth of Single Crystal Gan Nanowires." *J. Am. Chem. Soc.* **2000,** *122*, 188-189.
(25.) Yu, D. P.; Hang, Q. L.; Ding, Y.; Zhang, H. Z.; Bai, Z. G.; Wang, J. J.; Zou, Y. H.; Qian, W.; Xiong, G. C.; Feng, S. Q. "Amorphous Silica Nanowires: Intensive Blue Light Emitters." *App. Phys. Lett.* **1998,** *73*, 3076-3078.
(26.) Kim, Y.; Joyce, H. J.; Gao, Q.; Tan, H. H.; Jagadish, C.; Paladugu, M.; Zou, J.; Suvorova, A. A. "Influence of Nanowire Density on the Shape and Optical Properties of Ternary Ingaas Nanowires." *Nano Letters* **2006,** *6*, 599-604.
(27.) Riel, H.; Moselund, K. E.; Bessire, C.; Björk, M. T.; Schenk, A.; Ghoneim, H.; Schmid, H. "In *Inas-Si Heterojunction Nanowire Tunnel Diodes and Tunnel Fets*, "2012 International Electron Devices Meeting, 10-13 Dec. 2012; 2012; pp 16.6.1-16.6.4.
(28.) Xia, X.; Tu, J.; Zhang, Y.; Wang, X.; Gu, C.; Zhao, X.-b.; Fan, H. J. "High-Quality Metal Oxide Core/Shell Nanowire Arrays on Conductive Substrates for Electrochemical Energy Storage." *ACS Nano* **2012,** *6*, 5531-5538.
(29.) Schubert, E. F. "Introduction." In *Doping in Iii-V Semiconductors*, Schubert, E. F., Ed. Cambridge University Press: Cambridge, 1993; pp 1-5.
(30.) Young, H. D.; Freedman, R. A. "*University Physics : With Modern Physics*." Addison-Wesley: San Francisco, Calif.; Harlow, 2000.
(31.) Wen, B.; Sader, J. E.; Boland, J. J. "Mechanical Properties of Zno Nanowires." *Physical Review Letters* **2008,** *101*, 175502.
(32.) Cui, Y.; Zhong, Z.; Wang, D.; Wang, W. U.; Lieber, C. M. "High Performance Silicon Nanowire Field Effect Transistors." *Nano Letters* **2003,** *3*, 149-152.

(33.) Sung Dae, S.; Sung-Young, L.; Sung-Min, K.; Eun-Jung, Y.; Min-Sang, K.; Ming, L.; Chang Woo, O.; Kyoung Hwan, Y.; Sung Hwan, K.; Dong-Suk, S.; Kwan-Heum, L.; Heung Sik, P.; Jeong Nam, H.; Park, C. J.; Jong-Bong, P.; Dong-Won, K.; Donggun, P.; Byung-Il, R. "In *High Performance 5nm Radius Twin Silicon Nanowire Mosfet (Tsnwfet) : Fabrication on Bulk Si Wafer, Characteristics, and Reliability*, "IEEE InternationalElectron Devices Meeting, 2005. IEDM Technical Digest., 5-5 Dec. 2005; 2005; pp 717-720.

(34.) Thelander, C.; Agarwal, P.; Brongersma, S.; Eymery, J.; Feiner, L. F.; Forchel, A.; Scheffler, M.; Riess, W.; Ohlsson, B. J.; Gösele, U.; Samuelson, L. "Nanowire-Based One-Dimensional Electronics." *Materials Today* **2006,** *9*, 28-35.

(35.) Tian, B.; Kempa, T. J.; Lieber, C. M. "Single Nanowire Photovoltaics." *Chemical Society Reviews* **2009,** *38*, 16-24.

(36.) Brenner, A. "*Electrodeposition of Alloys: Principles and Practice*." Elsevier: 2013.

(37.) Endres, F.; Abbott, A.; MacFarlane, D. "*Electrodeposition from Ionic Liquids*." John Wiley & Sons: 2017.

(38.) Huo, S.; Schwarzacher, W. "Anomalous Scaling of the Surface Width During Cu Electrodeposition." *Physical Review Letters* **2001,** *86*, 256-259.

(39.) Shankar, K. S.; Raychaudhuri, A. K. "Fabrication of Nanowires of Multicomponent Oxides: Review of Recent Advances." *Materials Science and Engineering: C* **2005,** *25*, 738-751.

(40.) Kawai, S.; Ueda, R. "Magnetic Properties of Anodic Oxide Coatings on Aluminum Containing Electrodeposited Co and Co-Ni." *Journal of the Electrochemical Society* **1975,** *122*, 32-36.

(41.) AlMawlawi, D.; Coombs, N.; Moskovits, M. "Magnetic Properties of Fe Deposited into Anodic Aluminum Oxide Pores as a Function of Particle Size." *Journal of applied physics* **1991,** *70*, 4421-4425.

(42.) Blawert, C.; Dietzel, W.; Ghali, E.; Song, G. "Anodizing Treatments for Magnesium Alloys and Their Effect on Corrosion Resistance in Various Environments." *Advanced Engineering Materials* **2006,** *8*, 511-533.

(43.) Thompson, G. E. "Porous Anodic Alumina: Fabrication, Characterization and Applications." *Thin Solid Films* **1997,** *297*, 192-201.

(44.) Masuda, H.; Fukuda, K. "Ordered Metal Nanohole Arrays Made by a Two-Step Replication of Honeycomb Structures of Anodic Alumina." *science* **1995,** *268*, 1466.

(45.) Jessensky, O.; Müller, F.; Gösele, U. "Self-Organized Formation of Hexagonal Pore Arrays in Anodic Alumina." *App. Phys. Lett.* **1998,** *72*, 1173-1175.

(46.) Li, A. P.; Müller, F.; Birner, A.; Nielsch, K.; Gösele, U. "Hexagonal Pore Arrays with a 50–420 Nm Interpore Distance Formed by Self-Organization in Anodic Alumina." *Journal of Applied Physics* **1998,** *84*, 6023-6026.

(47.) Sander, M. S.; Prieto, A. L.; Gronsky, R.; Sands, T.; Stacy, A. M. "Fabrication of High-Density, High Aspect Ratio, Large-Area Bismuth Telluride Nanowire Arrays by Electrodeposition into Porous Anodic Alumina Templates." *Adv. Mater.* **2002,** *14*, 665-667.

(48.) Routkevitch, D.; Bigioni, T.; Moskovits, M.; Xu, J. M. "Electrochemical Fabrication of Cds Nanowire Arrays in Porous Anodic Aluminum Oxide Templates." *The Journal of Physical Chemistry* **1996,** *100*, 14037-14047.

(49.) Nielsch, K.; Müller, F.; Li, A. P.; Gösele, U. "Uniform Nickel Deposition into Ordered Alumina Pores by Pulsed Electrodeposition." *Adv. Mater.* **2000,** *12*, 582-586.

(50.) Darja Pečko; Rožman, K. Ž.; Kostevšek, N.; Shahid Arshad, M.; Markoli, B.; Samardžija, Z.; Kobe, S. "Electrodeposited Hard-Magnetic $Fe_{50}pd_{50}$ Nanowires from an Ammonium-Citrate-Based Bath." *J. All. Comp.* **2014,** *605*, 71-79.
(51.) Liang, Y.; Zhai, L.; Zhao, X.; Xu, D. "Band-Gap Engineering of Semiconductor Nanowires through Composition Modulation." *The Journal of Physical Chemistry B* **2005,** *109*, 7120-7123.
(52.) Rabin, O.; Herz, P. R.; Lin, Y. M.; Akinwande, A. I.; Cronin, S. B.; Dresselhaus, M. S. "Formation of Thick Porous Anodic Alumina Films and Nanowire Arrays on Silicon Wafers and Glass." *Advanced Functional Materials* **2003,** *13*, 631-638.
(53.) Walcarius, A. "Mesoporous Materials and Electrochemistry." *Chemical Society Reviews* **2013,** *42*, 4098-4140.
(54.) Ke, J.; Su, W.; Howdle, S. M.; George, M. W.; Cook, D.; Perdjon-Abel, M.; Bartlett, P. N.; Zhang, W.; Cheng, F.; Levason, W.; Reid, G.; Hyde, J.; Wilson, J.; Smith, D. C.; Mallik, K.; Sazio, P. "Electrodeposition of Metals from Supercritical Fluids." *Proc. Natl. Acad. Sci. U. S. A.* **2009,** *106*, 14768-72.
(55.) Bartlett, P. N.; Cook, D. C.; George, M. W.; Ke, J.; Levason, W.; Reid, G.; Su, W.; Zhang, W. "Phase Behaviour and Conductivity Study on Multi-Component Mixtures for Electrodeposition in Supercritical Fluids." *Phys. Chem. Chem. Phys.* **2010,** *12*, 492-501.
(56.) Cook, D.; Bartlett, P. N.; Zhang, W.; Levason, W.; Reid, G.; Ke, J.; Su, W.; George, M. W.; Wilson, J.; Smith, D.; Mallik, K.; Barrett, E.; Sazio, P. "The Electrodeposition of Copper from Supercritical Co(2)/Acetonitrile Mixtures and from Supercritical Trifluoromethane." *Phys. Chem. Chem. Phys.* **2010,** *12*, 11744-52.
(57.) Branch, J.; Alibouri, M.; Cook, D. A.; Richardson, P.; Bartlett, P. N.; Mátéfi-Tempfli, M.; Mátéfi-Tempfli, S.; Bampton, M.; Cookson, T.; Connell, P. "Plastic Reactor Suitable for High Pressure and Supercritical Fluid Electrochemistry." *Journal of The Electrochemical Society* **2017,** *164*, H375-H381.
(58.) Jaeger, G. "The Ehrenfest Classification of Phase Transitions: Introduction and Evolution." *Archive for history of exact sciences* **1998,** *53*, 51-81.
(59.) Ma, T.; Wang, S. "*Phase Transition Dynamics*." Springer: 2014.
(60.) von Helmolt, R.; Wecker, J.; Holzapfel, B.; Schultz, L.; Samwer, K. "Giant Negative Magnetoresistance in Perovskitelike La 2/3 Ba 1/3 Mno X Ferromagnetic Films." *Physical Review Letters* **1993,** *71*, 2331.
(61.) De Oliveira, M. J. "*Equilibrium Thermodynamics*." Springer: 2013.
(62.) Tabor, D. "*Gases, Liquids and Solids: And Other States of Matter*." Cambridge University Press: 1991.
(63.) De Podesta, M. "*Understanding the Properties of Matter*." CRC Press: 2002.
(64.) Antoine, C. "Tensions Des Vapeurs: Nouvelle Relation Entre Les Tensions Et Les Temperatures." *Comptes Rendus des Séances de l'Académie des Sciences* **1888,** *107*, 681-684.
(65.) Jenkins, H. D. B. "*Chemical Thermodynamics at a Glance*." John Wiley & Sons: 2008.
(66.) Hertz, H. "Ueber Das Verhalten Des Benzins Als Isolator Und Als Rückstandsbildner." *Annalen der Physik* **1883,** *256*, 279-284.
(67.) Knudsen, M. "Die Maximale Verdampfungsgeschwindigkeit Des Quecksilbers." *Annalen der Physik* **1915,** *352*, 697-708.
(68.) Maxwell, J. C. "V. Illustrations of the Dynamical Theory of Gases.—Part I. On the Motions and Collisions of Perfectly Elastic Spheres." *The London, Edinburgh, and Dublin Philosophical Magazine and Journal of Science* **1860,** *19*, 19-32.

(69.) Hoenig, C. L.; Searcy, A. W. "Knudsen and Langmuir Evaporation Studies of Stannic Oxide." *Journal of the American Ceramic Society* **1966,** *49*, 128-134.
(70.) Langmuir, I. "The Vapor Pressure of Metallic Tungsten." *Physical Review* **1913,** *2*, 329-342.
(71.) Langmuir, I. "The Evaporation, Condensation and Reflection of Molecules and the Mechanism of Adsorption." *Physical Review* **1916,** *8*, 149.
(72.) Munir, Z.; Hirth, J. "Surface Morphology of Sublimated Crystals of Cadmium and Zinc Sulfides." *Journal of Applied Physics* **1970,** *41*, 2697-2704.
(73.) Cassel, H. M. "Condensation Coefficient and Adsorption." *The Journal of Chemical Physics* **1949,** *17*, 1000-1001.
(74.) Wagner, W.; Saul, A.; Pruss, A. "International Equations for the Pressure Along the Melting and Along the Sublimation Curve of Ordinary Water Substance." *Journal of Physical and Chemical Reference Data* **1994,** *23*, 515-527.
(75.) Iijima, S. "Helical Microtubules of Graphitic Carbon." *Nature* **1991,** *354*, 56-58.
(76.) Mintmire, J. W.; Dunlap, B. I.; White, C. T. "Are Fullerene Tubules Metallic?" *Physical Review Letters* **1992,** *68*, 631-634.
(77.) Hamada, N.; Sawada, S.-i.; Oshiyama, A. "New One-Dimensional Conductors: Graphitic Microtubules." *Physical Review Letters* **1992,** *68*, 1579-1581.
(78.) Ebbesen, T. W. "Carbon Nanotubes." *Annual Review of Materials Science* **1994,** *24*, 235-264.
(79.) Yakobson, B. I.; Brabec, C. J.; Bernholc, J. "Nanomechanics of Carbon Tubes: Instabilities Beyond Linear Response." *Physical Review Letters* **1996,** *76*, 2511-2514.
(80.) Treacy, M. M. J.; Ebbesen, T. W.; Gibson, J. M. "Exceptionally High Young's Modulus Observed for Individual Carbon Nanotubes." *Nature* **1996,** *381*, 678-680.
(81.) Ebbesen, T. W.; Lezec, H. J.; Hiura, H.; Bennett, J. W.; Ghaemi, H. F.; Thio, T. "Electrical Conductivity of Individual Carbon Nanotubes." *Nature* **1996,** *382*, 54-56.
(82.) Odom, T. W.; Huang, J.-L.; Kim, P.; Lieber, C. M. "Atomic Structure and Electronic Properties of Single-Walled Carbon Nanotubes." *Nature* **1998,** *391*, 62-64.
(83.) Dresselhaus, M. S.; Dresselhaus, G.; Eklund, P.; Rao, A. "Carbon Nanotubes." In *The Physics of Fullerene-Based and Fullerene-Related Materials*, Springer: 2000; pp 331-379.
(84.) Dresselhaus, M.; Dresselhaus, G.; Saito, R. "Physics of Carbon Nanotubes." *Carbon* **1995,** *33*, 883-891.
(85.) Yoshinori, A.; Sumio, I. "Preparation of Carbon Nanotubes by Arc-Discharge Evaporation." *Japanese Journal of Applied Physics* **1993,** *32*, L107.
(86.) Bethune, D. S.; Klang, C. H.; de Vries, M. S.; Gorman, G.; Savoy, R.; Vazquez, J.; Beyers, R. "Cobalt-Catalysed Growth of Carbon Nanotubes with Single-Atomic-Layer Walls." *Nature* **1993,** *363*, 605-607.
(87.) Bronikowski, M. J. "Cvd Growth of Carbon Nanotube Bundle Arrays." *Carbon* **2006,** *44*, 2822-2832.
(88.) Pederson, M. R.; Broughton, J. Q. "Nanocapillarity in Fullerene Tubules." *Physical Review Letters* **1992,** *69*, 2689-2692.
(89.) Ajayan, P. M.; Iijima, S. "Capillarity-Induced Filling of Carbon Nanotubes." *Nature* **1993,** *361*, 333-334.
(90.) Ugarte, D.; Stöckli, T.; Bonard, J. M.; Châtelain, A.; de Heer, W. A. "Filling Carbon Nanotubes." *Applied Physics A* **1998,** *67*, 101-105.

(91.) Lago, R. M.; Tsang, S. C.; Lu, K. L.; Chen, Y. K.; Green, M. L. H. "Filling Carbon Nanotubes with Small Palladium Metal Crystallites: The Effect of Surface Acid Groups." *Journal of the Chemical Society, Chemical Communications* **1995**, 1355-1356.
(92.) K. Pradhan, B.; Kyotani, T.; Tomita, A. "Nickel Nanowires of 4 Nm Diameter in the Cavity of Carbon Nanotubes." *Chemical Communications* **1999**, 1317-1318.
(93.) Meyer, R. R.; Sloan, J.; Dunin-Borkowski, R. E.; Kirkland, A. I.; Novotny, M. C.; Bailey, S. R.; Hutchison, J. L.; Green, M. L. H. "Discrete Atom Imaging of One-Dimensional Crystals Formed within Single-Walled Carbon Nanotubes." *Science* **2000,** *289*, 1324-1326.
(94.) Su, Q.; Li, J.; Zhong, G.; Du, G.; Xu, B. "In Situ Synthesis of Iron/Nickel Sulfide Nanostructures-Filled Carbon Nanotubes and Their Electromagnetic and Microwave-Absorbing Properties." *J. Phys. Chem. C* **2011,** *115*, 1838-1842.
(95.) Geng, F.; Cong, H. "Fe-Filled Carbon Nanotube Array with High Coercivity." *Physica B: Condensed Matter* **2006,** *382*, 300-304.
(96.) Sloan, J.; Novotny, M.; Bailey, S.; Brown, G.; Xu, C.; Williams, V.; Friedrichs, S.; Flahaut, E.; Callender, R.; York, A. "Two Layer 4: 4 Co-Ordinated Ki Crystals Grown within Single Walled Carbon Nanotubes." *Chemical Physics Letters* **2000,** *329*, 61-65.
(97.) Spencer, J. H.; Nesbitt, J. M.; Trewhitt, H.; Kashtiban, R. J.; Bell, G.; Ivanov, V. G.; Faulques, E.; Sloan, J.; Smith, D. C. "Raman Spectroscopy of Optical Transitions and Vibrational Energies of ∼1 Nm Hgte Extreme Nanowires within Single Walled Carbon Nanotubes." *ACS Nano* **2014,** *8*, 9044-9052.
(98.) Chris, J. P.; Needs, R. J. "Ab Initio Random Structure Searching." *Journal of Physics: Condensed Matter* **2011,** *23*, 053201.
(99.) Pickard, C. J.; Needs, R. J. "High-Pressure Phases of Silane." *Phys Rev Lett* **2006,** *97*, 045504.
(100.) Ebbesen, T. W.; Ajayan, P. M.; Hiura, H.; Tanigaki, K. "Purification of Nanotubes." *Nature* **1994,** *367*, 519-519.
(101.) Ajayan, P. M.; Ebbesen, T. W.; Ichihashi, T.; Iijima, S.; Tanigaki, K.; Hiura, H. "Opening Carbon Nanotubes with Oxygen and Implications for Filling." *Nature* **1993,** *362*, 522-525.
(102.) Monthioux, M. "Filling Single-Wall Carbon Nanotubes." *Carbon* **2002,** *40*, 1809-1823.
(103.) Ram, S.; Ward, E. S.; Ober, R. J. "Beyond Rayleigh's Criterion: A Resolution Measure with Application to Single-Molecule Microscopy." *Proc. Natl. Acad. Sci. U. S. A.* **2006,** *103*, 4457-62.
(104.) Wells, O.; Boyde, A.; Lifshin, E.; Rezanowich, A. "Scanning Electron Microscopy**1974**.
(105.) Zhou, W.; Lin Wang, Z. "Scanning Microscopy for Nanotechnology." *Springer science & business media* **2007**.
(106.) Volkert, C. A.; Minor, A. M. "Focused Ion Beam Microscopy and Micromachining." *MRS Bulletin* **2007,** *32*, 389-399.
(107.) Wang, Z. M. "*Fib Nanostructures*." Springer: 2013.
(108.) Giannuzzi, L. A.; Stevie, F. A. "A Review of Focused Ion Beam Milling Techniques for Tem Specimen Preparation." *Micron* **1999,** *30*, 197-204.
(109.) Erni, R. "Aberration-Corrected Imaging in Transmission Electron Microscopy: An Introduction**2010**.

(110.) Scherzer, O. "Über Einige Fehler Von Elektronenlinsen." *Zeitschrift für Physik* **1936,** *101*, 593-603.
(111.) Krivanek, O.; Dellby, N.; Spence, A.; Camps, R.; Brown, L. "In *Aberration Correction in the Stem*, "Institute of Physics Conference Series, Bristol [England]; Boston: Adam Hilger, Ltd., c1985-: 1997; pp 35-40.
(112.) Jia, C. L.; Lentzen, M.; Urban, K. "Atomic-Resolution Imaging of Oxygen in Perovskite Ceramics." *Science* **2003,** *299*, 870-873.
(113.) Zemlin, F.; Weiss, K.; Schiske, P.; Kunath, W.; Herrmann, K. H. "Coma-Free Alignment of High Resolution Electron Microscopes with the Aid of Optical Diffractograms." *Ultramicroscopy* **1978,** *3*, 49-60.
(114.) Keyse, R. J. "Introduction to Scanning Transmission Electron Microscopy**1998**.
(115.) Pennycook, S. J.; Nellist, P. D. "*Scanning Transmission Electron Microscopy: Imaging and Analysis*." Springer New York: 2011.
(116.) Gubbens, A.; Barfels, M.; Trevor, C.; Twesten, R.; Mooney, P.; Thomas, P.; Menon, N.; Kraus, B.; Mao, C.; McGinn, B. "The Gif Quantum, a Next Generation Post-Column Imaging Energy Filter." *Ultramicroscopy* **2010,** *110*, 962-970.
(117.) Keast, V. J. "Ab Initio Calculations of Plasmons and Interband Transitions in the Low-Loss Electron Energy-Loss Spectrum." *Journal of Electron Spectroscopy and Related Phenomena* **2005,** *143*, 97-104.
(118.) Schattschneider, P.; Jouffrey, B. "Plasmons and Related Excitations." In *Energy-Filtering Transmission Electron Microscopy*, Reimer, L., Ed. Springer Berlin Heidelberg: Berlin, Heidelberg, 1995; pp 151-224.
(119.) Bragg, W. H.; Bragg, W. L. "The Reflection of X-Rays by Crystals." *Proceedings of the Royal Society of London. Series A, Containing Papers of a Mathematical and Physical Character* **1913,** *88*, 428-438.
(120.) Humphreys, C. J. "The Scattering of Fast Electrons by Crystals." *Reports on Progress in Physics* **1979,** *42*, 1825.
(121.) Cockayne, D. J. H. "The Study of Nanovolumes of Amorphous Materials Using Electron Scattering." *Annual Review of Materials Research* **2007,** *37*, 159-187.
(122.) Gotoh, K. "4 - Radial Distribution Function." In *Particulate Morphology*, Elsevier: Oxford, 2012; pp 37-59.
(123.) Mitchell, D. R.; Petersen, T. C. "Rdftools: A Software Tool for Quantifying Short-Range Ordering in Amorphous Materials." *Microsc Res Tech* **2012,** *75*, 153-63.
(124.) Britz, D. A.; Khlobystov, A. N. "Noncovalent Interactions of Molecules with Single Walled Carbon Nanotubes." *Chemical Society Reviews* **2006,** *35*, 637-659.
(125.) Segall, M.; Lindan, P. J.; Probert, M. a.; Pickard, C.; Hasnip, P.; Clark, S.; Payne, M. "First-Principles Simulation: Ideas, Illustrations and the Castep Code." *Journal of Physics: Condensed Matter* **2002,** *14*, 2717.
(126.) Morris, A. J.; Nicholls, R. J.; Pickard, C. J.; Yates, J. R. "Optados: A Tool for Obtaining Density of States, Core-Level and Optical Spectra from Electronic Structure Codes." *Computer Physics Communications* **2014,** *185*, 1477-1485.
(127.) Abbe, E. "Beiträge Zur Theorie Des Mikroskops Und Der Mikroskopischen Wahrnehmung." *Archiv für mikroskopische Anatomie* **1873,** *9*, 413-418.
(128.) Dunlap, W. C. "Electrical Properties of Gold-Germanium Alloys." *Physical Review* **1953,** *91*, 1282-1282.
(129.) Dodson, B. W.; McMillan, W. L.; Mochel, J. M.; Dynes, R. C. "Metal-Insulator Transition in Disordered Germanium-Gold Alloys." *Physical Review Letters* **1981,** *46*, 46-49.

(130.) Wu, M.; Brooks, N. R.; Schaltin, S.; Binnemans, K.; Fransaer, J. "Electrodeposition of Germanium from the Ionic Liquid 1-Butyl-1-Methylpyrrolidinium Dicyanamide." *Physical Chemistry Chemical Physics* **2013,** *15*, 4955-4964.
(131.) Wu, M.; Vanhoutte, G.; Brooks, N. R.; Binnemans, K.; Fransaer, J. "Electrodeposition of Germanium at Elevated Temperatures and Pressures from Ionic Liquids." *Physical Chemistry Chemical Physics* **2015,** *17*, 12080-12089.
(132.) Klavetter, K. C.; Pedro de Souza, J.; Heller, A.; Mullins, C. B. "High Tap Density Microparticles of Selenium-Doped Germanium as a High Efficiency, Stable Cycling Lithium-Ion Battery Anode Material." *Journal of Materials Chemistry A* **2015,** *3*, 5829-5834.
(133.) Cooper, A. "Precise Lattice Constants of Germanium, Aluminum, Gallium Arsenide, Uranium, Sulphur, Quartz and Sapphire." *Acta Crystallographica* **1962,** *15*, 578-582.
(134.) Stratton, W. G.; Hamann, J.; Perepezko, J. H.; Voyles, P. M. "Electron Beam Induced Crystallization of Amorphous Al-Based Alloys in the Tem." *Intermetallics* **2006,** *14*, 1061-1065.
(135.) Zhang, Y.; Ni, Y.; Wang, X.; Xia, J.; Hong, J. "Polycrystalline Cu7te4 Dendritic Microstructures Constructed by Spherical Nanoparticles: Fast Electrodeposition, Influencing Factors, and the Shape Evolution." *Crystal Growth & Design* **2011,** *11*, 4368-4377.
(136.) Li, B.; Xie, Y.; Huang, J.; Liu, Y.; Qian, Y. "Sonochemical Synthesis of Nanocrystalline Copper Tellurides Cu7te4 and Cu4te3 at Room Temperature." *Chemistry of Materials* **2000,** *12*, 2614-2616.
(137.) Zhang, L.; Ai, Z.; Jia, F.; Liu, L.; Hu, X.; Yu, J. C. "Controlled Hydrothermal Synthesis and Growth Mechanism of Various Nanostructured Films of Copper and Silver Tellurides." *Chemistry* **2006,** *12*, 4185-90.
(138.) Palchik, O.; Kerner, R.; Zhu, Z.; Gedanken, A. "Preparation of Cu2−Xte and Hgte by Using Microwave Heating." *Journal of Solid State Chemistry* **2000,** *154*, 530-534.
(139.) Mizota, T.; Koto, K.; Morimoto, N. "Crystallography and Composition of Synthetic Rickardite." *Mineralogical Journal* **1973,** *7*, 252-261.
(140.) Stevels, A. L. N.; Wiegers, G. A. "Phase Transitions in Copper Chalcogenides Ii. The Tellurides Cu3-X Te2 and Cute." *Recueil des Travaux Chimiques des Pays-Bas* **1971,** *90*, 352-359.
(141.) Malte Giller; Grotz, C.; Rudyk, B. W.; Mar, A.; Nilges, T. "Cu_6te_3s – a Cu-Filled Cr_3si-Structure Variant." *Zeitschrift für Kristallographie - Crystalline Materials* **2014,** *229*.
(142.) Makovicky, E.; Søtofte, I.; Karup-Møller, S. "The Crystal Structure of Cu2.31tes0.32. - a Condensed Cluster Compound." *Zeitschrift fuer Kristallographie* **2000,** *215*, 475-480.
(143.) Meister, S.; Schoen, D. T.; Topinka, M. A.; Minor, A. M.; Cui, Y. "Void Formation Induced Electrical Switching in Phase-Change Nanowires." *Nano Letters* **2008,** *8*, 4562-4567.
(144.) Nielsen, M. H.; Aloni, S.; De Yoreo, J. J. "In Situ Tem Imaging of Caco₃ Nucleation Reveals Coexistence of Direct and Indirect Pathways." *Science* **2014,** *345*, 1158-1162.
(145.) Xin, H. L.; Niu, K.; Alsem, D. H.; Zheng, H. "In Situ Tem Study of Catalytic Nanoparticle Reactions in Atmospheric Pressure Gas Environment." *Microscopy and Microanalysis* **2013,** *19*, 1558-1568.

(146.) Marín, L.; Warot-Fonrose, B.; Estève, A.; Chabal, Y. J.; Alfredo Rodriguez, L.; Rossi, C. "Self-Organized Al2cu Nanocrystals at the Interface of Aluminum-Based Reactive Nanolaminates to Lower Reaction Onset Temperature." *ACS Applied Materials & Interfaces* **2016,** *8*, 13104-13113.
(147.) Gulec, A.; Klie, R. F. "Direct Measurement of the Low Temperature Spin State Transitions in La1−Xsrxcoo3 (0.05 < X < 0.3)." *Journal of Applied Physics* **2014,** *116*, 233701.
(148.) Hudak, B. M.; Chang, Y.-J.; Yu, L.; Li, G.; Edwards, D. N.; Guiton, B. S. "Real-Time Observation of the Solid–Liquid–Vapor Dissolution of Individual Tin(Iv) Oxide Nanowires." *ACS Nano* **2014,** *8*, 5441-5448.
(149.) Bartlett, P. N.; Burt, J.; Cook, D. A.; Cummings, C. Y.; George, M. W.; Hector, A. L.; Hasan, M. M.; Ke, J.; Levason, W.; Pugh, D.; Reid, G.; Richardson, P. W.; Smith, D. C.; Spencer, J.; Suleiman, N.; Zhang, W. "A Versatile Precursor System for Supercritical Fluid Electrodeposition of Main-Group Materials." *Chemistry – A European Journal* **2016,** *22*, 302-309.
(150.) Epstein, A. S.; Fritzsche, H.; Lark-Horovitz, K. "Electrical Properties of Tellurium at the Melting Point and in the Liquid State." *Physical Review* **1957,** *107*, 412-419.
(151.) Qadri, S. B.; Skelton, E. F.; Hsu, D.; Dinsmore, A. D.; Yang, J.; Gray, H. F.; Ratna, B. R. "Size-Induced Transition-Temperature Reduction in Nanoparticles of Zns." *Physical Review B* **1999,** *60*, 9191-9193.
(152.) Lai, S.; Guo, J.; Petrova, V.; Ramanath, G.; Allen, L. "Size-Dependent Melting Properties of Small Tin Particles: Nanocalorimetric Measurements." *Physical review letters* **1996,** *77*, 99.
(153.) Shaygan, M.; Gemming, T.; Bezugly, V.; Cuniberti, G.; Lee, J.-S.; Meyyappan, M. "In Situ Observation of Melting Behavior of Znte Nanowires." *J. Phys. Chem. C* **2014,** *118*, 15061-15067.
(154.) Sun, X.; Yu, B.; Ng, G.; Meyyappan, M. "One-Dimensional Phase-Change Nanostructure: Germanium Telluride Nanowire." *J. Phys. Chem. C* **2007,** *111*, 2421-2425.
(155.) Honig, R. E. "Vapor Pressure Data for the More Common Elements." *RCA Review* **1957,** *XVIII*, 195 - 205.
(156.) Thomson, G. W. "The Antoine Equation for Vapor-Pressure Data." *Chemical Reviews* **1946,** *38*, 1-39.
(157.) Yaws, C. L. "*The Yaws Handbook of Vapor Pressure: Antoine Coefficients*." Gulf Professional Publishing: 2015.
(158.) Safarian, J.; Engh, T. A. "Vacuum Evaporation of Pure Metals." *Meta. Mater. Trans. A* **2012,** *44*, 747-753.
(159.) L'vov, B. V. "Thermal Decomposition of Solids and Melts**2007**.
(160.) Brewer, L.; Gilles, P. W.; Jenkins, F. A. "The Vapor Pressure and Heat of Sublimation of Graphite." *The Journal of Chemical Physics* **1948,** *16*, 797-807.
(161.) Marek, R.; Straub, J. "Analysis of the Evaporation Coefficient and the Condensation Coefficient of Water." *International Journal of Heat and Mass Transfer* **2001,** *44*, 39-53.
(162.) Fujikawa, S.; Yano, T.; Watanabe, M. "*Vapor-Liquid Interfaces, Bubbles and Droplets: Fundamentals and Applications*." Springer Science & Business Media: 2011.
(163.) Yim, J. W. L.; Xiang, B.; Wu, J. "Sublimation of Gete Nanowires and Evidence of Its Size." *J. Am. Chem. Soc.* **2009,** *131*, 14526-14530.
(164.) Livesey, R. G. "Flow of Gases through Tubes and Orifices." Wiley: 1998; pp 81-140.

(165.) Marquardt, N. "Introduction to the Principles of Vacuum Physics." *CERN EUROPEAN ORGANIZATION FOR NUCLEAR RESEARCH-REPORTS-CERN* **1999**, 1-24.
(166.) Chambers, A. "*Modern Vacuum Physics*." CRC Press: 2004.
(167.) Steckelmacher, W. "Knudsen Flow 75 Years On: The Current State of the Art for Flow of Rarefied Gases in Tubes and Systems." *Reports on Progress in Physics* **1986,** *49*, 1083.
(168.) O'Hanlon, J. F. "*A User's Guide to Vacuum Technology*." John Wiley & Sons: 2005.
(169.) Roth, A. "*Vacuum Technology*." Elsevier: 2012.
(170.) Cucka, P.; Barrett, C. S. "The Crystal Structure of Bi and of Solid Solutions of Pb, Sn, Sb and Te in Bi." *Acta Crystallographica* **1962,** *15*, 865-872.
(171.) Kaye, G. W. C.; Laby, T. H. "*Tables of Physical and Chemical Constants*." Longman: 1995.
(172.) Voigt-Martin, I.; Garbella, R.; Schumacher, M. "Structure and Defects in Discotic Crystals and Liquid Crystals as Revealed by Electron Diffraction and High-Resolution Electron Microscopy." *Macromolecules* **1992,** *25*, 961-971.
(173.) Evans, K.; Beanland, R. "High Dynamic Range Electron Imaging: The New Standard." *Microscopy and Microanalysis* **2014,** *20*, 1601-1604.
(174.) Greenberg, Y.; Yahel, E.; Caspi, E. N.; Benmore, C.; Beuneu, B.; Dariel, M. P.; Makov, G. "Evidence for a Temperature-Driven Structural Transformation in Liquid Bismuth." *EPL (Europhysics Letters)* **2009,** *86*, 36004.
(175.) Isherwood, S. P.; Orton, B. R. "An X-Ray Diffraction Investigation of Liquid Bismuth." *Philosophical Magazine* **1968,** *17*, 561-574.
(176.) Emuna, M.; Mayo, M.; Greenberg, Y.; Caspi, E. N.; Beuneu, B.; Yahel, E.; Makov, G. "Liquid Structure and Temperature Invariance of Sound Velocity in Supercooled Bi Melt." *J Chem Phys* **2014,** *140*, 094502.
(177.) Waseda, Y.; Suzuki, K. "Structure Factor and Atomic Distribution in Liquid Metals by X-Ray Diffraction." *physica status solidi (b)* **1972,** *49*, 339-347.
(178.) Sharrah, P. C.; Smith, G. P. "Neutron Diffraction and Atomic Distribution in Liquid Lead and Liquid Bismuth at Two Temperatures." *The Journal of Chemical Physics* **1953,** *21*, 228.
(179.) Akola, J.; Atodiresei, N.; Kalikka, J.; Larrucea, J.; Jones, R. O. "Structure and Dynamics in Liquid Bismuth and Bi(N) Clusters: A Density Functional Study." *J Chem Phys* **2014,** *141*, 194503.
(180.) Cahill, J. A.; Kirshenbaum, A. D. "The Density of Liquid Bismuth from Its Melting Point to Its Normal Boiling Point and an Estimate of Its Critical Constants." *Journal of Inorganic and Nuclear Chemistry* **1963,** *25*, 501-506.
(181.) Baughman, R. H.; Zakhidov, A. A.; de Heer, W. A. "Carbon Nanotubes--the Route toward Applications." *Science* **2002,** *297*, 787-792.
(182.) Smalley, R. E.; Dresselhaus, M. S.; Dresselhaus, G.; Avouris, P. "*Carbon Nanotubes: Synthesis, Structure, Properties, and Applications*." Springer Science & Business Media: 2003; Vol. 80.
(183.) Liu, C.; Fan, Y. Y.; Liu, M.; Cong, H. T.; Cheng, H. M.; Dresselhaus, M. S. "Hydrogen Storage in Single-Walled Carbon Nanotubes at Room Temperature." *Science* **1999,** *286*, 1127-1129.
(184.) Journet, C.; Maser, W. K.; Bernier, P.; Loiseau, A.; de la Chapelle, M. L.; Lefrant, S.; Deniard, P.; Lee, R.; Fischer, J. E. "Large-Scale Production of Single-Walled Carbon Nanotubes by the Electric-Arc Technique." *Nature* **1997,** *388*, 756-758.

(185.) Fan, S.; Chapline, M. G.; Franklin, N. R.; Tombler, T. W.; Cassell, A. M.; Dai, H. "Self-Oriented Regular Arrays of Carbon Nanotubes and Their Field Emission Properties." *Science* **1999,** *283*, 512-514.
(186.) Scott, C. D.; Arepalli, S.; Nikolaev, P.; Smalley, R. E. "Growth Mechanisms for Single-Wall Carbon Nanotubes in a Laser-Ablation Process." *Applied Physics A: Materials Science & Processing* **2001,** *72*, 573-580.
(187.) Sun, L. F.; Xie, S. S.; Liu, W.; Zhou, W. Y.; Liu, Z. Q.; Tang, D. S.; Wang, G.; Qian, L. X. "Materials: Creating the Narrowest Carbon Nanotubes." *Nature* **2000,** *403*, 384-384.
(188.) Kasperski, A.; Weibel, A.; Datas, L.; De Grave, E.; Peigney, A.; Laurent, C. "Large-Diameter Single-Wall Carbon Nanotubes Formed Alongside Small-Diameter Double-Walled Carbon Nanotubes." *J. Phys. Chem. C* **2015,** *119*, 1524-1535.
(189.) Ivanov, A. S.; Kar, T.; Boldyrev, A. I. "Nanoscale Stabilization of Zintl Compounds: 1d Ionic Li-P Double Helix Confined inside a Carbon Nanotube." *Nanoscale* **2016,** *8*, 3454-60.
(190.) Buffat, P.; Borel, J. P. "Size Effect on the Melting Temperature of Gold Particles." *Physical review A* **1976,** *13*, 2287.
(191.) Meyerson, B. S.; Uram, K. J.; LeGoues, F. K. "Cooperative Growth Phenomena in Silicon/Germanium Low-Temperature Epitaxy." *App. Phys. Lett.* **1988,** *53*, 2555-2557.
(192.) Gómez-Rodríguez, A.; Beltrán-del-Río, L.; Herrera-Becerra, R. "Simulatem: Multislice Simulations for General Objects." *Ultramicroscopy* **2010,** *110*, 95-104.
(193.) Zhang, X. Q.; Li, H.; Liew, K. M. "The Structures and Electrical Transport Properties of Germanium Nanowires Encapsulated in Carbon Nanotubes." *Journal of Applied Physics* **2007,** *102*, 073709.
(194.) Cui, G.; Gu, L.; Kaskhedikar, N.; van Aken, P. A.; Maier, J. "A Novel Germanium/Carbon Nanotubes Nanocomposite for Lithium Storage Material." *Electrochimica Acta* **2010,** *55*, 985-988.
(195.) Mansour, A. N.; Wong-Ng, W.; Huang, Q.; Tang, W.; Thompson, A.; Sharp, J. "Structural Characterization of Bi2te3 and Sb2te3 as a Function of Temperature Using Neutron Powder Diffraction and Extended X-Ray Absorption Fine Structure Techniques." *Journal of Applied Physics* **2014,** *116*, 083513.
(196.) Smith, B. W.; Luzzi, D. E. "Electron Irradiation Effects in Single Wall Carbon Nanotubes." *Journal of Applied Physics* **2001,** *90*, 3509-3515.
(197.) Ghosh, P.; Kahaly, M. U.; Waghmare, U. V. "Atomic and Electronic Structures, Elastic Properties, and Optical Conductivity of Bulk Te and Te Nanowires: A First-Principles Study." *Physical Review B* **2007,** *75*, 245437.
(198.) Bauer Pereira, P.; Sergueev, I.; Gorsse, S.; Dadda, J.; Müller, E.; Hermann, R. P. "Lattice Dynamics and Structure of Gete, Snte and Pbte." *physica status solidi (b)* **2013,** *250*, 1300-1307.
(199.) Schmidt, V.; Riel, H.; Senz, S.; Karg, S.; Riess, W.; Gösele, U. "Realization of a Silicon Nanowire Vertical Surround-Gate Field-Effect Transistor." *small* **2006,** *2*, 85-88.
(200.) Singh, A. K.; Kumar, V.; Briere, T. M.; Kawazoe, Y. "Cluster Assembled Metal Encapsulated Thin Nanotubes of Silicon." *Nano Letters* **2002,** *2*, 1243-1248.
(201.) Hu, M.-S.; Chen, H.-L.; Shen, C.-H.; Hong, L.-S.; Huang, B.-R.; Chen, K.-H.; Chen, L.-C. "Photosensitive Gold-Nanoparticle-Embedded Dielectric Nanowires." *Nature materials* **2006,** *5*, 102-106.